

UNIVERSITY OF CRETE
DEPARTMENT OF MATERIALS SCIENCE AND TECHNOLOGY

DEVELOPMENT AND STUDY OF PLASMONIC ORGANIC PHOTOVOLTAIC CELLS

GEORGE SPYROPOYLOS



University of Crete

August 2012

Supervisors: Dr. Stratakis Emmanuel, Prof. Kymakis Emmanuel

Abstract

The effect of incorporation of surfactant-free metallic nanoparticles (NPs) into the photoactive layer (P3HT:PCBM) and at the PEDOT:PSS/P3HT:PCBM interface of organic bulk heterojunction (BHJ) photovoltaic (PV) devices was systematically studied. It is evidenced that the NPs doping give rise to a dual improvement effect. On the one hand it leads to a better PV efficiency and on the other hand it results in enhanced photovoltaic stability and thus to slower device degradation rate during prolonged illumination. Spectroscopic analysis combined with photon-to-electron conversion efficiency measurements indicate that the efficiency improvement can be attributed to enhanced light harvesting and subsequent exciton generation rate into the photoactive layer due to localized surface plasmon resonant absorption and scattering effects. Besides this, the improved degradation stability is found to be caused by the enhanced structural and morphological properties of the NPs doped blend, as evidenced by an original approach based on joint in-situ time-resolved X-ray and atomic force microscopy monitoring. The role of the NPs surface termination is investigated by monitoring the performance of PV devices doped with various types of coated NPs.

Acknowledgments

I would like to express my deep gratitude to Dr. Emmanuel Stratakis and Prof. Emmanuel Kymakis for their educational and emotional support, for I could not reach without them this experience level so soon in my career. My special thanks also to my friend and contributor Minas Stylianakis for his moral support. Finally, I would like to mention that our group exceeded the framework of a usual academic group and passed into the boundaries of friendship.

Dedicated to my parents, Dimitris Spyropoulos and Vassiliki Spyropoulou and to my grandmothers, Anastasia Spyropoulou and Efrosini Georgara.

List of Publications

1. “Plasmonic organic photovoltaics doped with metal nanoparticles”,
George. D. Spyropoulos, Minas M. Stylianakis, E. Stratakis, E. Kymakis.
Photonics and Nanostructures - Fundamentals and Applications, 9 (2) pp. 184-189
2. “Enhanced structural stability and performance durability of bulk heterojunction photovoltaic devices incorporating metallic nanoparticles”,
Barbara Paci, **George D. Spyropoulos**, Amanda Generosi, Daniele Bailo, Valerio Rossi Albertini, Emmanuel Stratakis, and Emmanuel Kymakis.
Advanced Funtional Materials, 21 (18), pp. 3573–3582
3. “Spin coated carbon nanotubes as the hole transport layer in organic photovoltaics”,
Kymakis E., **Spyropoulos G.D.**, Stylianakis M., Stratakis, Koudoumas E., Fotakis C.
Solar Energy Materials and Solar Cells, in press, 10.1016/j.solmat.2011.09.046
4. “Organic bulk heterojunction photovoltaic devices with surfactant-free Au nanoparticles embedded in the active layer”, **George. D. Spyropoulos**, Minas M. Stylianakis, E. Stratakis, E. Kymakis. *Applied Physics Letters*, 100, 213904.
5. “Solution Processable Graphine linked to 3,5-DNitrobenzoyl as an electron acceptor in Organic Bulk Heterojunction Photovoltaic Devices”, Minas M. Stylianakis, **George. D. Spyropoulos**, E. Stratakis, E. Kymakis. *Carbon*, in press

Abbreviations and Symbols

AFM	Atomic force microscope
BHJ	Bulk heterojunction
DSC	Differential scanning calorimetry
EDXD	Energy dispersive X-ray diffraction
EDXR	Energy dispersive X-ray reflectivity
HOMO	Highest occupied molecular orbital
ITO	Indium tin oxide
J_{sc}	short circuit current density
LEDs	Light emitting diodes
LSPR	Localize plasmon resonance
LSPs	Localize surface plasmons
LUMO	Lowest unoccupied molecular orbital
OPVs	Organic Photovoltaics
P3HT	Poly(3-hexylthiophene-2,5-diyl)
PCBM	Phenyl-C61-butyric acid methyl ester
PEDOT:PSS	Poly(3,4-ethylenedioxythiophene) poly(styrenesulfonate)
SPPs	Surface plasmon polaritons
TEM	Transmission electron microscopy
TOAB	Tetraoctylammonium bromide
V_{oc}	Open circuit voltage

Table of Contents

1 Introduction	8
1.1 Motivation	9
2 Organic Electronic Materials	13
2.1 Conjugated Polymers	13
2.1.1 Introduction	13
2.1.2 Electronic Properties of Conjugated Polymers	15
2.1.3 Polythiophenes	20
2.2 Fullerene acceptors.....	25
2.3 Buffer Layer	26
3 Photovoltaic technology	29
3.1 P-N junction Solar Cells.....	29
3.2 Polymer Solar Cells.....	31
3.2.1 Types of OPVs	31
3.2.2 Bulk heterojunction concept and operating principles	33
3.3 Characteristics of a photovoltaic device.....	40
3.3.1 Current-Voltage Characteristics	40
3.3.2 Solar cell efficiency	43
4 Plasmonic Theory	46
4.1 Surface Plasmons	46
4.1.1 Basic Introduction to Plasmons	47
4.1.2 Bulk and Surface Plasmons	48
4.1.3 Extinction by metallic nanoparticles	53
4.1.4 Tuning the Plasmon Resonance	56
4.1.5 Utilizing Surface Plasmons in solar cells	61
5 Experimental procedures	68
5.1 Materials preparation.....	68
5.2 Device Fabrication	70
6 Results and discussion	81
6.1 Overview of research in Plasmonic OPVs	81
6.2 Surfactant free Nanoparticles	86
6.3 Incorporation of Surfactant free NPs in active layer/PEDOT:PSS interface	87
6.4 Incorporation of Surfactant free NPs in active layer	90
6.5 The Effect of Surfactant free NPs incorporation on Cell Aging	96
6.6 The role of NPs surfactant.....	107
6.7 Conclusion and Future Directions.....	112

Chapter 1

Introduction

In 1839 the French physicist Alexandre-Edmond Becquerel discovered the photovoltaic phenomenon. It took 42 years for the first photovoltaic device to appear, an event that triggered the inception of research in a field that now days can provide energy and ecological solutions. Since that first device, the evolution road of the photovoltaic technology is parted in three generations. The 1st generation was constituted by thick silicon films, while the 2nd by thin inorganic films. The 3rd generation is divided in two sections, the one that aims cost independently at high efficiencies and the other that aims at low-cost adequate efficiencies. The second part is mainly represented by Organic Photovoltaics (OPVs).

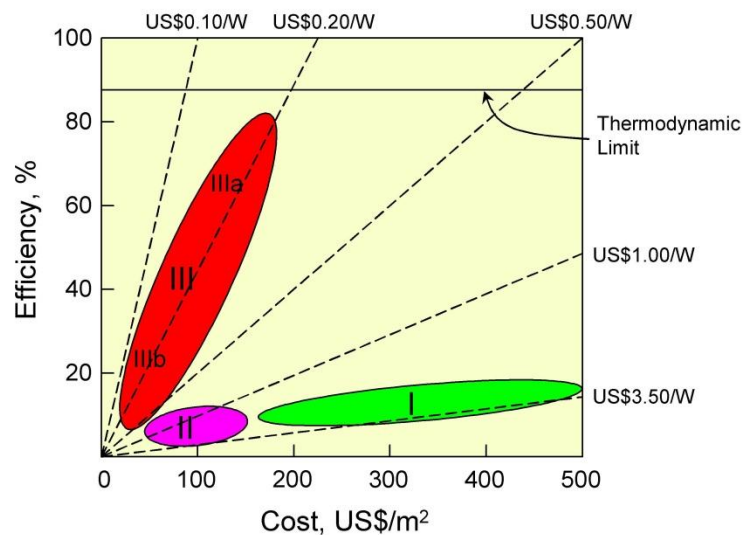


Figure 1.1 Efficiency dependence on cost for the three photovoltaic technology generations. OPVs are enlisted in the category IIIb.

1.1 Motivation

The experimental aim of this thesis is the manufacturing, analysis and optimization of OPV and plasmonic OPV devices, by incorporating metallic nanostructures. Furthermore, the theoretical part includes the interpretation of the functional mechanisms of these devices.

So, someone would wonder why photovoltaic technology, and why organic photovoltaic technology. These questions can be answered by observing the main ways of energy productions in “conservative” countries, which depend mainly on station or machines that spent consumable energy resources like petroleum and gas (fossil fuels). On the other hand, “modern” countries started to turn their eyesight in more exciting energy resources like uranium and other radioactive materials (nuclear energy). However, these resources are limited (something that also means increase of the cost) and their use has a serious environmental impact, which extends probably over several future generations¹. This situation poses an enormous pressure to the global community to address in a more sustainable energy production and in “green” development which will cover the needs of today without jeopardizing the future.

Several renewable energy sources are under development or even already introduced on market. Still, they make up only a limited part of the total energy production². Electric power can be produced indirectly from the conversion of water and wind energy to mechanical and afterwards to electrical. However, this procedure includes complex, expensive and massive parts (e.g. turbines).

Another renewable energy source that can serve as baseload resource in electrical networks is geothermal energy. The Earth’s heat becomes available to us by e.g. natural hot springs and can be used as such or converted into electricity. Though, limited in access, geothermal energy is a huge resource that is already exploited to a growing extend.

The fourth, and the strongest, “competitor” that claims a share in the production of sustainable energy, is bioenergy. Bioenergy, is carbon neutral and therefore does not contribute to the greenhouse effect.

Last but not least, the solar energy. The total amount of solar irradiation per year on the Earth's surface equals 1000 times the world's yearly energy need. Additionally, the direct conversion of solar energy to electricity through solar cells gives applicability and potentiality that is absolutely justified³.

Nowadays, the majority of solar cells are made of inorganic semiconductors, such as Si and GaAs. State-of-the-art monocrystalline silicon solar cells can reach power efficiencies up to 27.6% (Fig.1.2). However manufacturing these cells requires many energy intensive processing steps at very high temperatures leading to relatively high production costs and high energy pay back times (the time required for a solar cell to convert an amount of energy equivalent to that consumed in its production). Hence these solar cells are still too expensive to replace non-renewable energy sources.

On the other hand, organic solar cells that use conjugated polymers offer the possibility of low cost, less toxic manufacturing methods and the possibility of large area, light weight, flexible panels. Conjugated polymers are organic molecules with alternating single and double carbon-carbon bonded atoms and their electrical conductivity ranges from that of insulators to that of metals. They combine both the optoelectronic properties of semiconductors and the excellent mechanical and processing properties of polymeric materials and can be fabricated easily and cheaply by many solution processing techniques like printing, doctor-blading, slot die and roll-to-roll onto any desired substrate. These characteristics give a great benefit to organic solar cells for commercialization.

In conclusion, despite these benefits, organic photovoltaics, like its classical counterpart, have to fulfill the basic requirements for renewable energy production. In the energy market the competitive position of every solar technology is mainly determined by the factors efficiency, lifetime and costs (per Wp). The potential of organic photovoltaic has to be judged by these key figures as well, and two of them are drawbacks at the present. Fig.1.2 summarizes the restrictions within which organic photovoltaics can be commercialized. The important message of this figure is that successful commercialization can be realized only if all three technology driving aspects are fulfilled at the same time. A product development succeeding in only two aspects like, e.g. competitive costs and reasonable efficiency, will only be able to address niche markets unless the third parameter, in that case, life time, is also optimized.

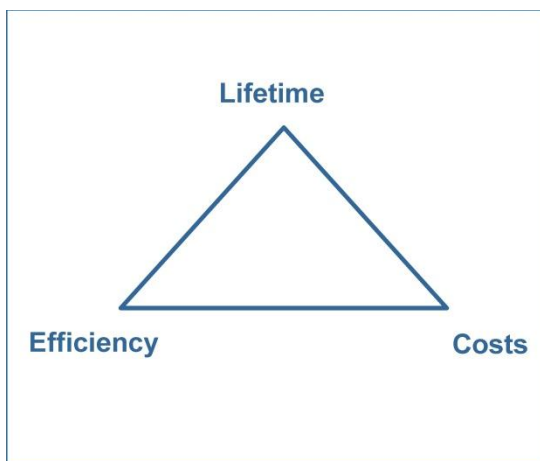


Figure 1.2 The critical triangle for photovoltaics with the three key factors.

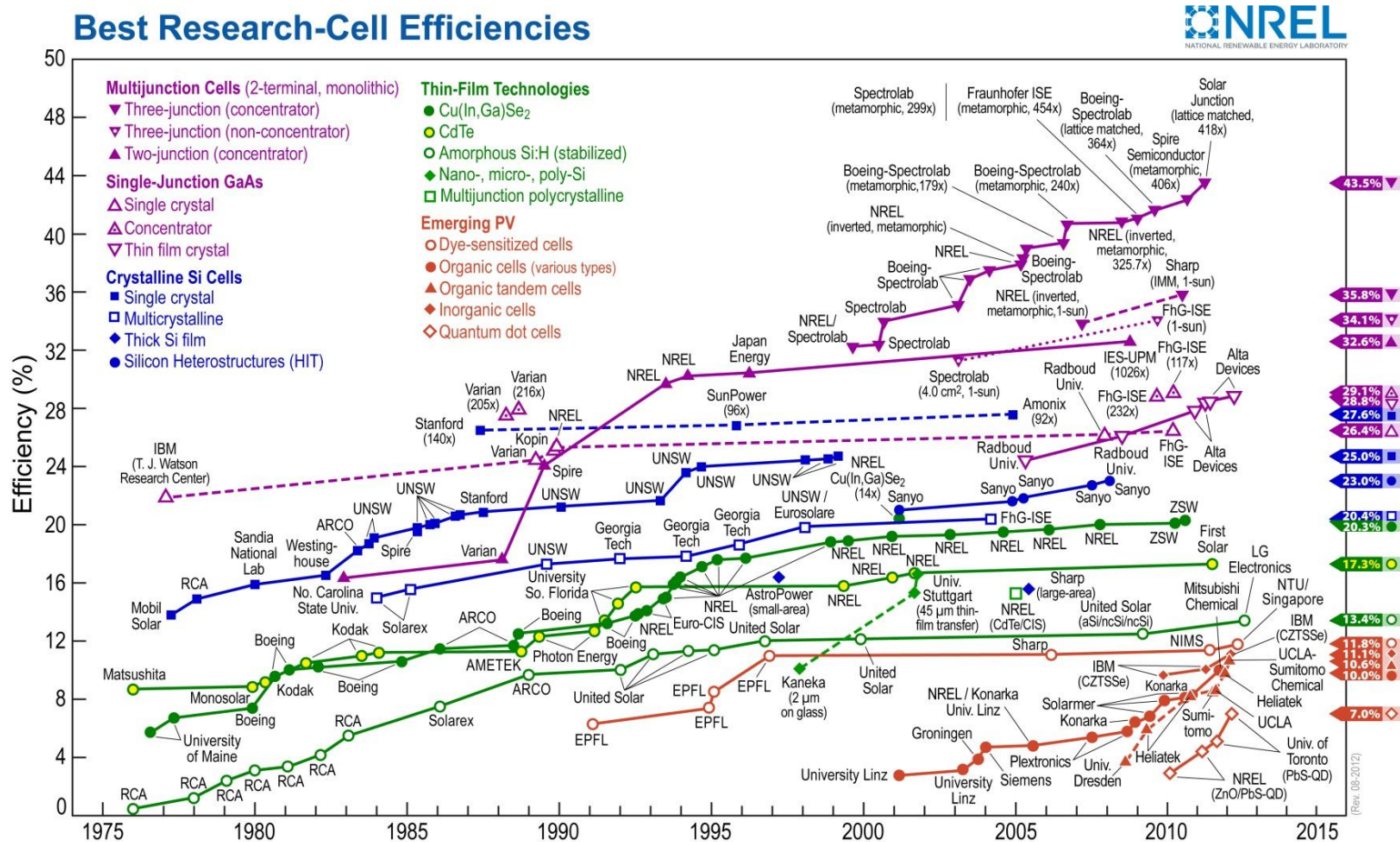


Figure 1.3 Best research-cell efficiencies for several technologies presented by the National Renewable Energy Laboratory

¹ World Energy Assesment: Overview,2004 Update, United Nation Development Programme(2004)

² Renewables in Global Energy Supply,InternationalEnergyAgency(2002)

³ A Vision for Photovoltaic Technology ReportbythePhotovoltaicTechnology ResearchAdvisoryCouncilPV-TRAC, DirectorateGeneralforResearch,EuropeanCommission(2005)

Chapter 2

Organic Electronic Materials

Currently, many promising low cost photovoltaic technologies are available and grouped under the name OPVs. All of them have a common, that at least one of the key functions for the solar energy conversion is accomplished by an organic semiconductor. Therefore, in order to understand the functional mechanism of OPVs, the knowledge of physics behind the organic materials that act as semiconductors, is essential.

2.1 *Conjugated Polymers*

2.1.1 Introduction

Conjugated polymers are a new class of organic materials with promising electronic properties. In their pristine form they behave as an insulator or a semiconductor, while in their doped form they become conducting. Together with these electrical properties come the intrinsic advantages of polymers, such as low cost, low toxicity and ease of manufacture over large area on low weight and flexible substrates. In this section, a short background on conjugated polymers is presented.

The basic element of an organic molecule is carbon, and a polymer contains a long sequence of consecutive carbon atoms. The carbon atoms are in turn linked together by covalent bonds. A polymer chain can be seen as being built up of small units repeating themselves throughout the chain. These units are called monomers and are the building blocks of the polymer. The unique property of conjugated polymers is the presence of conjugated double bonds along the backbone of the polymer. In conjugation, the bonds between the carbon atoms are alternately single and double. Every bond contains a localized σ bond which forms a strong chemical bond. In addition, every double bond also contains a less strongly localized π bond which is weaker.

Firstly, it is essential to understand how the carbon atoms behave when taking part in a chemical bond. The electronic structure of carbon is $1s^2 2s^2 2p^2$, having six

electrons of which only four can be used in bonds. The two 1s electrons are referred as core electrons, while the other four electrons are called valence electrons. The valence electrons in the carbon atom exhibit hybridization, a consequence of the electronic excitation of one or more 2s electrons to an empty 2p orbital. Depending on how the four valence electrons in carbon hybridize, one has sp^3 , sp^2 or sp hybridization. In conjugated polymers, three of these electrons, two with 2p ($2p_x$ and $2p_y$) character and one with 2s character, form three sp^2 hybridized orbitals. These three sp^2 -hybridized orbitals consist of three lobes, symmetrically directed in the xy-plane. Two of them will form the backbone of σ -bond type, whereas the third will bind to an hydrogen atom. The remaining fourth valence electron will form the p_z orbital pointing normal to the plane of the σ -bonds, as shown in Figure 2.1; it is delocalized over the whole molecule. The p_z electrons will form π -bonds with the neighbouring carbon atoms. This system of interacting p_z -orbitals is called a conjugated π system. The π -electrons can move quite freely a certain distance, which defines the conjugation length. The combination consisting of one of the σ -bonds and one π -bond between two given carbon atoms is referred as a double bond. The geometrical structures of several common conjugated polymers are shown in Figure 2.2, where the condition for conjugation, the alternation of the single and double bonds along the polymer backbone, can be seen.

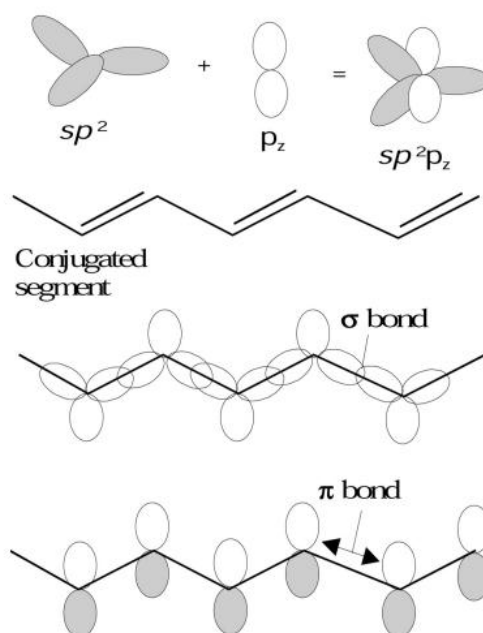


Figure 2.1 A simple molecular orbital representation of σ and π bonds in trans -polyacetylene, showing the p_z orbitals which overlap to provide the π bonds.

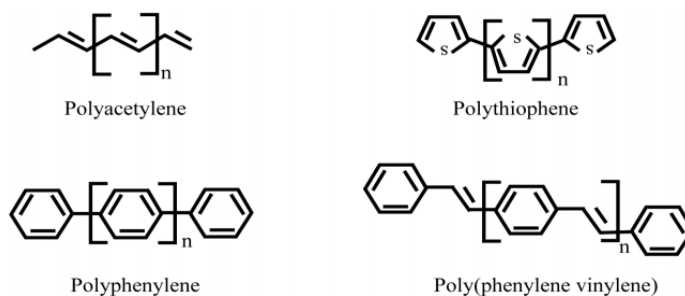


Figure 2.2 Some examples of conjugated polymers, in each one a sequence of alternating single and double bonds can be identified.

2.1.2 Electronic Properties of Conjugated Polymers

The conjugated polymers are found to be electrically insulating or semiconducting, and their band structure appears to be analogous to those of inorganic materials. The source of the semiconducting properties of conjugated polymers is related to the characteristics of the π bonds. First, the π -bonds are delocalized over the entire molecule and then, the quantum mechanical overlap of p_z orbitals on two carbon atoms splits their degeneracy and produces two orbitals, a bonding (π) orbital and an antibonding (π^*) (See Figure 2.3). The lower energy π -orbital produces the valence band, and the higher energy π^* -orbital forms the conduction band. In a polymer chain, several electrons contribute to the π system and the bonding and antibonding orbitals are made further degenerate, and become broad quasi-continuous energy bands⁴.

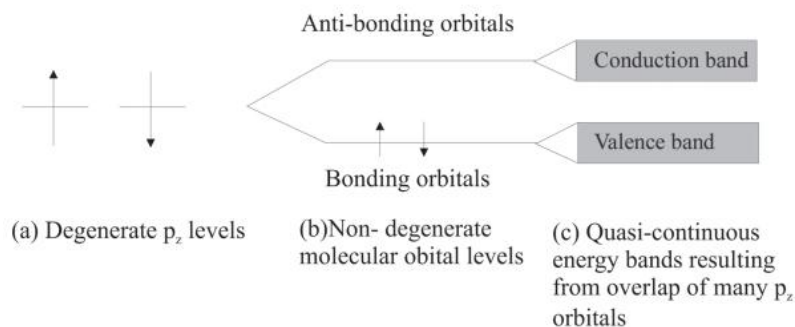


Figure 2.3 Schematic diagram showing the energy levels of electrons in p_z hybridised atomic levels and subsequently in the π bonding and anti-bonding molecular orbitals when a) two atoms are brought together to form a dimer and b) when a large number of atoms in a chain contribute to the delocalized π system.

Analogous to the valence and conduction band in inorganic semiconductors, the occupied π band forms the highest occupied molecular orbital (HOMO) and the unoccupied π^* band forms the lowest unoccupied molecular orbital (LUMO) of the polymer. As the overlap between the adjacent p_z orbitals and the number of electrons participating in the π system increases, the widths of the bands become broader, and the energy-gap between them decreases.

The difference in energy between the HOMO and the LUMO is defined as the bandgap. The bandgap controls the optoelectronic properties of the conjugated polymers and its value varies between conjugated polymers depending on the geometry and the type of the monomer units building the polymer. Band gaps are in the range of 1.5 to 3.5 eV, indicating that most of the polymers are active in the visible region. Exciting an electron from the valence to the conduction band is equivalent to transferring an electron from a bonding orbital to an anti-bonding orbital, by supplying it with energy greater than the bandgap. In a real polymer chain, the conjugation is unlikely to extend along its full length, as imperfections and defects interrupt the orbital overlap. Instead, there will be a series of chain segments, each of which is characterized by a different number of repeating units and has a different energy gap. The short chain segments will have a wide energy gap, while the long segments will have a narrow gap.

In solid crystals there is a 3 dimensional electronic band structure corresponding to the 3 dimensional nature of the crystal. Polymers are essentially 1 dimensional systems. That is because of the very long backbone of atoms, strongly bound to each other and the small interaction with neighbouring polymer chains. In particular there is strong coupling between the electronic excitations and the local configuration of the polymer chain. This leads to a family of excited states such as solitons, polarons, bipolarons and excitons, which represent the electronic excitations of the polymer combined with their associated lattice distortions.

2.1.2.1 Solitons

A conjugated polymer chain is not perfect and bond alternation defects are very common. Defects can be introduced during chemical synthesis, through photo excitation, chemical doping or by charge injection. Therefore, interruptions in the conjugation along

the chain are likely to be found. This structural defect is believed to be directly linked with the localized electronic state with energy in the middle of the bandgap, the ground state. In conjugated polymers, this ground state has two configurations with either the same (it has a degenerate ground state) or different energy (non-degenerate ground state), depending upon their geometrical configuration. Polyacetylene belongs to the degenerate class of conjugated polymers, meaning that the interchange of single and double bonds results in a geometrical equivalent state, with equal ground state energies. The equivalency of energy for the two different geometries on two adjacent portions of a polymer chain results in apparent bond alternation defects. The region between the two different, but energetically equal, regions defines a transition region where the bond lengths are almost equal, this region is called a soliton because it may travel as a solitary wave, without distortion or dissipation of energy^{5,6}. This is illustrated in Fig 2.4.

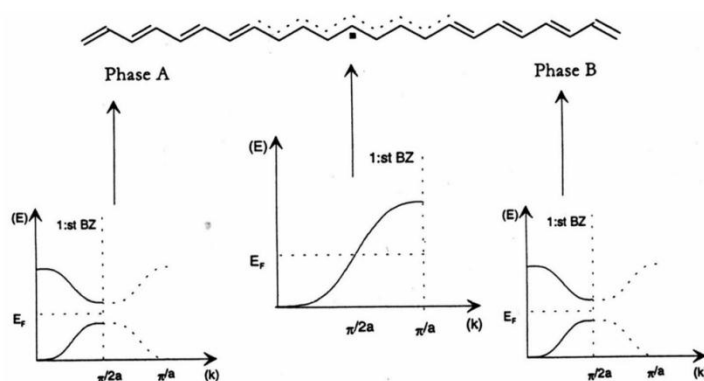


Figure 2.4 A transition region created by two different bond alternating phases A and B as well as the schematic sketch of the band structure for the different regions. Note that in the transition region, where the bond lengths are equal, the band is half filled with density of states at the Fermi level.

Hence, the soliton is represented as a transition region between two regions with alternating double and single bonds. Within the transition region the bond length between the carbon atoms are almost the same in contrast to the dimerised double and single bond regions around the transition region. This new energy state can accommodate either 1 or 2 electrons. If one unpaired electron alone occupies this level, then the soliton is neutral and carries a $1/2$ spin. The other two possible states are charged states with zero and two electrons respectively, but without any net spin. The three cases are shown in Fig 2.5.

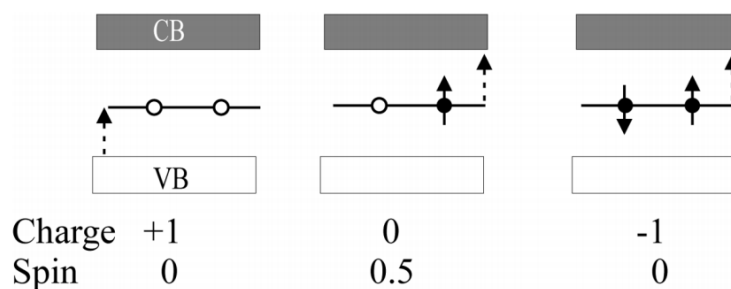


Figure 2.5 The three states of a soliton: positively charged, neutral and negatively charged.

Only the neutral soliton carries a spin. Also displayed are the possible transitions to and from the mid-gap states.

2.1.2.2 Polarons and Bipolarons

In non-degenerate ground state polymers, such as Poly(phenylene vinylene) (PPV), a simple exchange of the single and double bonds does not reproduce the same geometrical state. Instead, the energy of the state generated by the interchange always exhibits higher ground state energy, as shown in Fig 2.6. Since the higher energy ground state of the bond alternation reversal is unstable, the resultant change in bond lengths must be such that the phase of the polymer chain remains identical on either side of the defect.

This increase in ground state energy leads to a strong interaction between the two otherwise mobile solitons, resulting in a bonding and an anti-bonding interaction of the two states. Two new states, a symmetric and anti-symmetric combinations of the starting states are formed with energies which lie within the otherwise forbidden energy band gap. Depending on the amount of charge involved, there will be a single or double charged state. The single-charged state is called a polaron and carries a spin, whereas the double-charged state is called a bipolaron and carries no spin⁷.

A qualitative understanding of the polaronic charge carriers can be achieved by using the PPV, containing aromatic benzene rings, as the model system. For simplicity, the p-type doping, will be only considered. If an electron is removed from the neutral chain, a free radical (an unpaired electron with spin 1/2) and a spin-less positive charge are created, coupled to each other via a localized bond rearrangement, which takes the

form of a sequence of quinoid rings. This combination of a charged site coupled to a free radical via a local lattice distortion, creates a new localised electronic state within the bandgap (polaron P+), with the lower energy state being occupied by a single unpaired electron of spin 1/2. Upon further oxidation, the free radical of the polaron is removed and a dication (double positively charged ion) is created comprised of two positive charges coupled through the lattice distortion. This new spin-less defect is called a positive bipolaron (BP++).

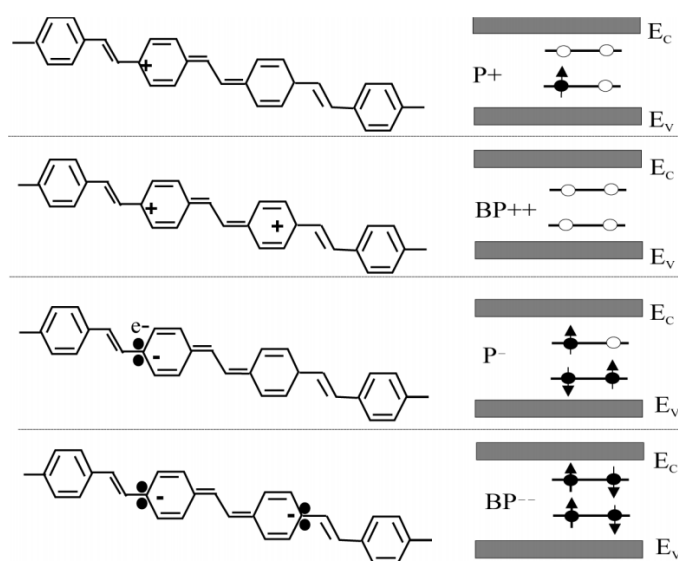


Figure 2.6 Schematic representation of polaron and bipolaron states in PPV.

2.1.2.3 Excitons

The concept of excitons is well known in the field of semiconductors and molecular crystals but its existence has been the subject of controversy in the polymer field. For inorganic semiconductors, the exciton is defined as an electron-hole pair bound by Coulomb attraction (Wannier exciton). In molecular crystals, the exciton can be considered as a bound electron-hole pair localised on one molecular unity (molecular exciton or Frenkel exciton). It is also electrically neutral, with just a dipole moment. When a photon of light of the appropriate energy interacts with an electron in the ground state, the electron is promoted from the HOMO (valence) to the LUMO (conduction) (π - π^* transition). However, the resulting electron and hole are bound, and their motion through the material is coupled. These coupled pairs are known as excitons. An exciton

can be considered as a Frenkel exciton, if the pair is confined to one molecular unit or as a Mott-Wannier exciton if it extends over many molecular units⁸. The intermediate case, where the exciton extends over a few adjacent molecular units, can be called the charge-transfer exciton. Also, the terms “inter-chain” and “intra-chain” exciton are used for polymeric semiconductors to indicate that the constituent charges are located on different or on the same polymer chains respectively.

The exciton binding energy of conjugated polymers depends strongly on the structure⁹. For highly crystalline polydiacetylene, the binding energy has been determined to be 0.5 eV, while for amorphous polymers like the polythiophene and PPV, is about 0.4 eV^{10,11}.

2.1.3 Polythiophenes

Polythiophenes (PTs)¹² result from the polymerization of thiophenes, a sulfur heterocycle, that can become conducting when electrons are added or removed from the conjugated π -orbitals via doping. Poly(3-hexylthiophene) (P3HT) is one of the most famous and commonly used polymers of this family. It simply has one additional carbohydrate chain in the position 3 of the sulfur heterocycle.

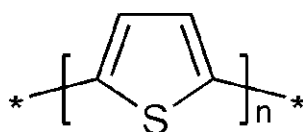


Figure 2.7 Repeating unit (monomer) of polythiophene

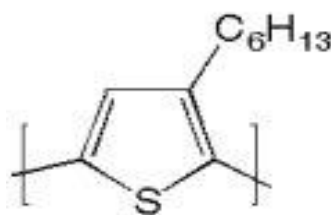


Figure 2.8 Repeating unit of P3HT

2.1.3.1 Mechanism of conductivity and doping

Electrons are delocalized along the conjugated backbones of conducting polymers, usually through overlap of π -orbitals, resulting in an extended π -system with a filled valence band. By removing electrons from the π -system (“p-doping”), or adding electrons into the π -system (“n-doping”), a charged unit called a bipolaron is formed.

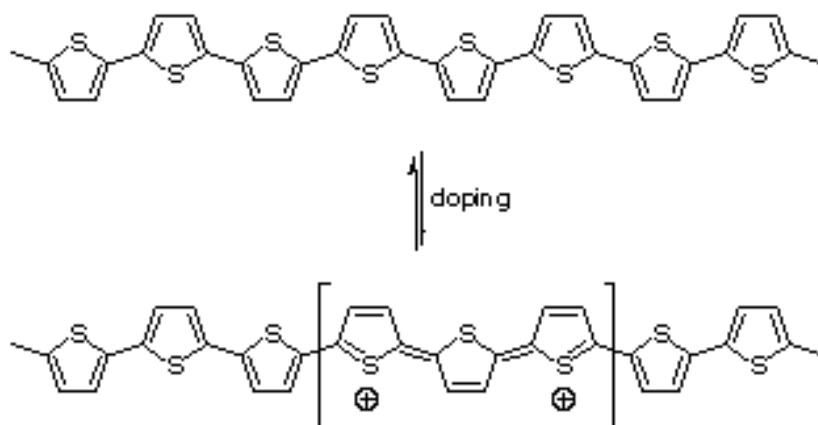


Figure 2.9 Removal of two electrons (p-doping) from a PT chain produce a bipolaron

2.1.3.2 Conjugation length and optical properties

The extended π -systems of conjugated PTs produce some of the most interesting properties of these materials—their optical properties. As an approximation, the conjugated backbone can be considered as a real-world example of the “electron-in-a-box” solution to the Schrödinger equation; however, the development of refined models to accurately predict absorption and fluorescence spectra of well-defined oligo(thiophene) systems is ongoing.[ref]Conjugation relies upon overlap of the π -orbitals of the aromatic rings, which, in turn, requires the thiophene rings to be coplanar.

The number of coplanar rings determines the conjugation length—the longer the conjugation length, the lower the separation between adjacent energy levels, and the longer the absorption wavelength. Deviation from coplanarity may be permanent, resulting from mislinkages during synthesis or especially bulky side chains; or temporary, resulting from changes in the environment or binding. This twist in the backbone reduces

the conjugation length (see Figure 2, bottom), and the separation between energy levels is increased. This results in a shorter absorption wavelength.

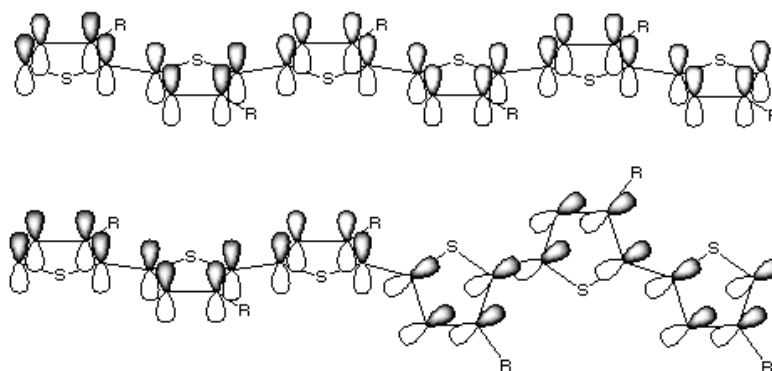


Figure 2.10 Conjugated π -orbitals of a coplanar and a twisted substituted PT.

Determining the maximum effective conjugation length requires the synthesis of regioregular PTs of defined length. The absorption band in the visible region is increasingly red-shifted as the conjugation length increases, and the maximum effective conjugation length is calculated as the saturation point of the red-shift. Early studies by ten Hoeve *et al.* estimated that the effective conjugation extended over 11 repeat units,^[18] while later studies increased this estimate to 20 units.¹⁹ More recently, Otsubo *et al.* synthesized 48-²⁰ and 96-mer²¹ oligothiophenes, and found that the red-shift, while small (a difference of 0.1 nm between the 72- and the 96-mer), does not saturate, meaning that the effective conjugation length may be even longer than 96 units.²¹

A variety of environmental factors can cause the conjugated backbone to twist, reducing the conjugation length and causing an absorption band shift, including solvent, temperature, application of an electric field, and dissolved ions. The absorption band of poly (3-thiophene acetic acid) in aqueous solutions of poly(vinyl alcohol)(PVA) shifts from 480 nm at pH 7 to 415 nm at pH 4. This is attributed to formation of a compact coil structure which can form hydrogen bonds with PVA upon partial deprotonation of the acetic acid group.²² Chiral PTs showed no induced circular dichroism (ICD) in chloroform, but displayed intense, but opposite, ICDs in chloroform–acetonitrile mixtures versus chloroform–acetone mixtures.²³ Also, a PT with a chiral amino acid side chain^[24] displayed moderate absorption band shifts and ICDs, depending upon the pH and the concentration of buffer.^[25]

Shifts in PT absorption bands due to changes in temperature result from a conformational transition from a coplanar, rodlike structure at lower temperatures to a nonplanar, coiled structure at elevated temperatures. For example, poly(3-(octyloxy)-4-methylthiophene) undergoes a color change from red–violet at 25 °C to pale yellow at 150 °C. An isosbestic point (a point where the absorbance curves at all temperatures overlap) indicates coexistence between two phases, which may exist on the same chain or on different chains.²⁶ Not all thermochromic PTs exhibit an isosbestic point: highly regioregular poly(3-alkylthiophene)s (PATs) show a continuous blue-shift with increasing temperature if the side chains are short enough so that they do not melt and interconvert between crystalline and disordered phases at low temperatures.^[citation needed]

Finally, PTs can exhibit absorption shifts due to application of electric potentials (electrochromism),²⁷ or to introduction of alkali ions (ionochromism).²⁸

2.1.3.3 Regioregularity

The asymmetry of 3-substituted thiophenes results in three possible couplings when two monomers are linked between the 2- and the 5-positions. These couplings are:

- 2,5', or head–tail (HT), coupling
- 2,2', or head–head (HH), coupling
- 5,5', or tail–tail (TT), coupling

These three diads can be combined into four distinct triads, shown in Figure 3.

The triads are distinguishable by NMR spectroscopy, and the degree of regioregularity can be estimated by integration.^{29,30} Elsenbaumer *et al.* first noticed the effect of regioregularity on the properties of PTs. A regiorandom copolymer of 3-methylthiophene and 3-butylthiophene possessed a conductivity of 50 S/cm, while a more regioregular copolymer with a 2:1 ratio of HT to HH couplings had a higher conductivity of 140 S/cm.³¹ Films of regioregular poly(3-(4-octylphenyl)thiophene) (POPT) with greater than 94% HT content possessed conductivities of 4 S/cm, compared with 0.4 S/cm for regiorandom POPT.³² PATs prepared using Rieke zinc formed “crystalline, flexible, and bronze-colored films with a metallic luster.” On the other hand, the corresponding regiorandom polymers produced “amorphous and orange-colored films.”³³ Comparison of the thermochromic properties of the Rieke PATs showed that, while the regioregular

polymers showed strong thermochromic effects, the absorbance spectra of the regioirregular polymers did not change significantly at elevated temperatures. This was likely due to the formation of only weak and localized conformational defects.

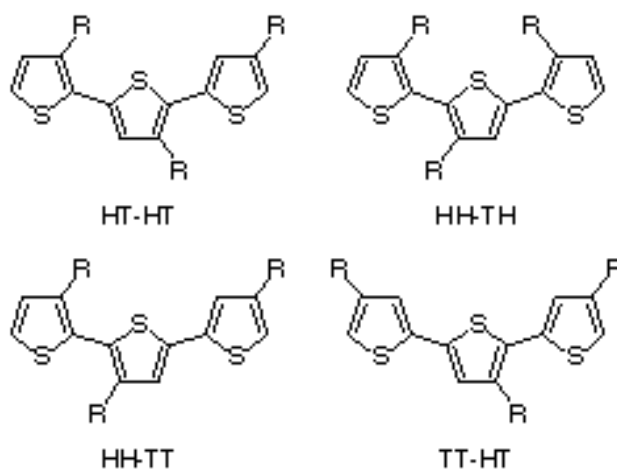


Figure 2.11 The four possible triads resulting from coupling of 3-substituted thiophenes.

Finally, Xu and Holdcroft demonstrated that the fluorescence absorption and emission maxima of poly(3-hexylthiophene)s occur at increasingly lower wavelengths (higher energy) with increasing HH dyad content. The difference between absorption and emission maxima, the Stokes shift, also increases with HH dyad content, which they attributed to greater relief from conformational strain in the first excited state.³⁴

2.2 *Fullerene acceptors*

Fullerenes were discovered by Robert Curl, Harold Kroto and Richard Smalley in 1985 as the third allotrope of carbon. For this discovery, they were awarded, the year 1996, by the Nobel Prize in chemistry. C₆₀ is the most abundant form of fullerenes, other forms are C₇₀, C₇₈, C₈₄, etc.

Fullerene is defined as an enclosed "cage" made of carbon hexagons and pentagons. Using Euler's theorem for polyhedra, we can ascertain that 60 carbons are located in 12 pentagons and 20 hexagons. Its shape is similar to a soccer ball: The black

leather pieces are pentagons and the white, hexagons. C_{60} took its name in honor of the architect Buckminster Fuller, who used the particular geometry to buildings.

High symmetry is responsible for the unique properties of C_{60} . Because of the degeneracy of LUMO, the material has very high electronic affinity and can accept up to 6 electrons. The energy gap HOMO-LUMO varies around the value 1.8 eV, but the visual transition from HOMO to LUMO is forbidden due to symmetry. C_{60} also has interesting mechanical properties that are used for drug design.

C_{60} is relatively insoluble. In order to achieve higher solubility in commonly used solvents, some derivatives were synthesized. Functionalization of fullerenes with specific side groups does not cause significant changes in electronic structure, but changes importantly the solubility

PCBM is the common abbreviation for the fullerene derivative [6,6]-phenyl-C61-butyrac methyl ester which is widely used in the manufacture of organic photovoltaics. It is a derivative of C_{60} , which was first synthesized by Fred Wudl et al¹³, and as is indicated by its full name, is a C_{60} with a lateral group. The structure shown in Figure 2.12. It shows increased solubility in organic solvents, for example 40mg/ml to 10mg/ml in chlorobenzene and toluene. The electrochemical reduction of PCBM is changing to more downward at 100mV (as compared to that of C_{60}), which means a worse electron acceptor. This is due to a loss of double bond in the "cage". However, PCBM remains an excellent electron acceptor and thus a good material to use in organic electronics.

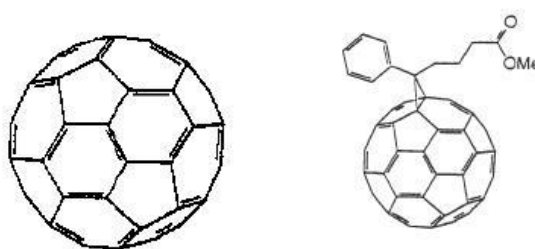


Figure 2.12 The structure of C_{60} and PCBM.

The mobility of electrons (electron mobility) in PCBM has been investigated using various techniques and found to range from $2 * 10^{-3}$ - $4.5 * 10^{-3}$ $cm^2 V^{-1} s^{-1}$.

Figure 2.13 shows the optical absorption and emission of light one layer PCBM. According to the symmetry of energy levels, the HOMO-LUMO transition is forbidden and so the absorption is weak at 700nm. The spectrum at room temperature shows a maximum at 740nm and a local increase in 810nm.

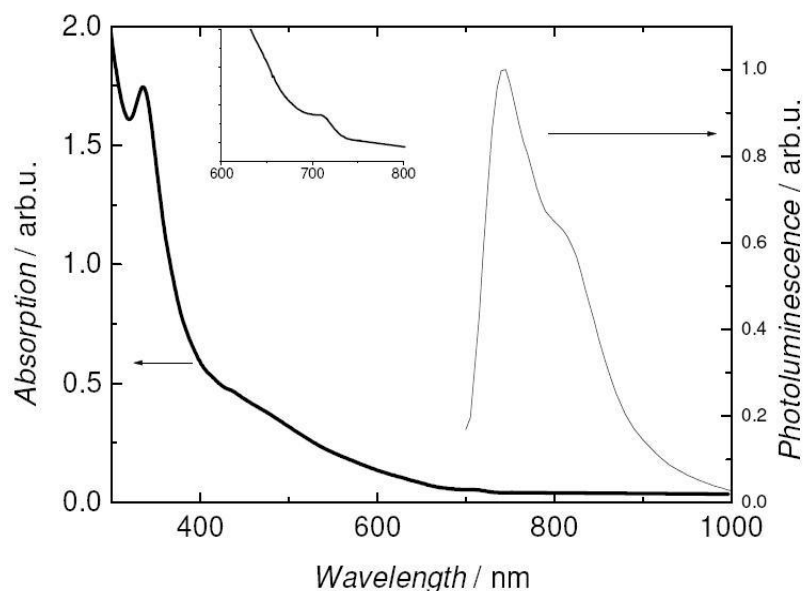


Figure 2.13 The absorption spectrum and emitting a thin layer of PCBM. The insert shows the absorption in this region.

2.3 Buffer Layer

PEDOT:PSS or Poly(3,4-ethylenedioxythiophene) poly(styrenesulfonate) (fig 2.14) is a polymer mixture of two ionomers. One component in this mixture is made up of sodium polystyrene sulfonate which is a sulfonated polystyrene. Part of the sulfonyl groups are deprotonated and carry a negative charge. The other component poly(3,4-ethylenedioxythiophene) or PEDOT is a conjugated polymer and carries positive charges and is based on polythiophene. Together the charged macromolecules form a macromolecular salt.

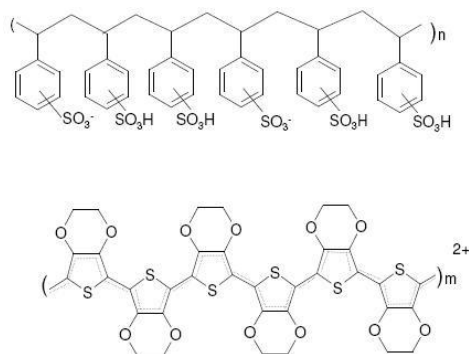


Figure 2.14 Chemical composition of PEDOT:PSS. The upper region exhibits the oligomer PSS, and the lower region the oligomer PEDOT:PSS

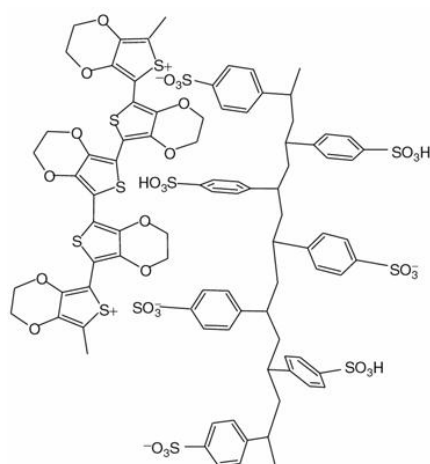


Figure 2.15 Conformation of PEDOT:PSS

This compound is generally applied as a dispersion of gelled particles in water. A conductive layer on glass is obtained by spreading a layer of the dispersion on the surface usually by spin coating and driving out the water by heat. Special PEDOT:PSS inks and formulations were developed for different coating and printing processes.

Water based PEDOT:PSS inks are mainly used in slot die coating, flexography, rotogravure and inkjet printing. If a high viscous paste and slow drying is required like in screen-printing processes PEDOT:PSS can also be supplied in high boiling solvents like propanediol. Dry PEDOT:PSS pellets can be produced with a freeze drying method which are redispersible in water and different solvents, for example ethanol to increase drying speed during printing. Finally, to overcome degradation to ultraviolet light and high temperature / humidity conditions PEDOT:PSS UV-stabilizers are available.

It is used as a transparent, conductive polymer with high ductility in different applications. These two materials exhibit high transparency in light of wavelength in the region 350-900 nm. The field of Organic Electronics is one of the fields that utilizes this material exploiting these very interesting characteristics. Furthermore, is reducing the roughness of the ITO layer and optimize the electric contact with the active layer. Additionally, increases the work function of the positive electrode from 4.7-4.9 eV (that fluctuates the work function of ITO) to 5eV.

-
- ⁴ J. J. M. Halls, Ph.D. thesis , Cambridge University, 1997.
- ⁵ M. J. Rice, Physical Letters A71 , 152 (1979)
- ⁶ W. P. Su, J. R. Shrieffer, and A. J. Heeger, Physical Review Letters 42 , 1698(1979).
- ⁷ T. Skotheim, J. Reynolds , and R. Elsenbaumer, Handbook of Conducting Polymers (Marcel Dekker, NY, 1986).
- ⁸ N. C. Greenham and R. H. Friend, Solid State Physics 49 , 1 (1995).
- ⁹ S. Mazumbar, M. Chandross , and N. S. Sariciftci, Primary photoexcitations in conjugated polymers (World Scientific, Singapore, 1997).
- ¹⁰ E. M. Conwell and H. A. Mizes, Physical Review B 51 , 6953 (1995).
- ¹¹ R. N. Marks, J. J. Halls, D. D. C. Bradley, R. H. Friend, and A. B. Holmes, Journal of Physics-Condensed Matter 6 , 1379 (1994).
- ¹² Street, G. B.; Clarke, T. C. *IBM J. Res. Dev.* **1981**,25, 51–57.
- ¹³ Hummelen, Jan C.; Knight, Brian W.; Lepeq, F.; Wudl, Fred; Yao, Jie; Wilkins, Charles L. (1995). "Preparation and Characterization of Fulleroid and Methanofullerene Derivatives". *The Journal of Organic Chemistry* **60** (3): 532–538.

Chapter 3

Photovoltaic technology

3.1 P-N Junction Solar Cells

At the heart of solar energy is the semiconductor p-n junction. A standard silicon solar cell consists of p-doped and n-doped semiconductor layers forming the p-n junction, an antireflection coating, current collectors and a metal substrate for the collection of photogenerated charge carriers from n-type (electrons) and p-type (holes) layers respectively. A schematic is shown in Figure 3.1.

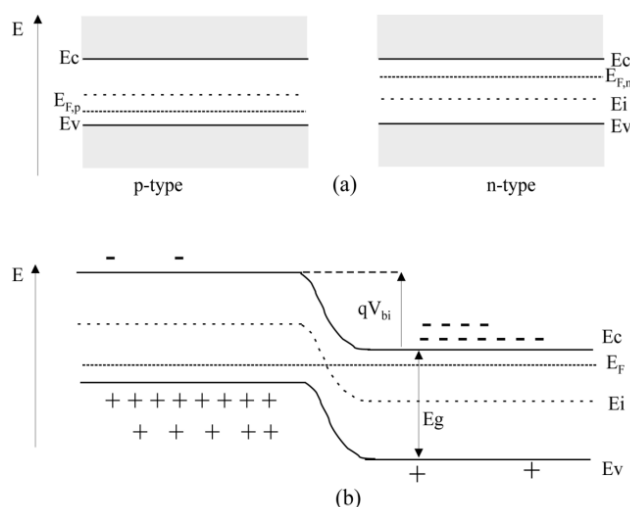


Figure 3.1 Schematic diagram of an p-n junction, (b) Diagram of energy levels showing creating of a contact potential. While in thermal equilibrium no external voltage is applied between the n-type and p-type material, there is an internal potential, qV_{bi} , which is caused by the work function difference between the n-type and p-type semiconductors.

N-type semiconductors are obtained by doping with impurity atoms having an excess valence electron with respect to the surrounding host atoms, while p-type semiconductors are obtained by doping with impurity atoms with one valence electron less than the surrounding atoms. The n-type doping results in localized energy states just below the conduction band edge of the host semiconductor lattice and occupied by the

excess electrons from the impurity atoms, while p-type doping results in (Figure 3.1) localized empty states with energy slightly above the valence band edge of the semiconductor.

The donor atoms in the n-type material are easily ionised by thermal excitation, due to the closeness of the donor states and the conduction band edge. The ionization of the donor atoms generates free electrons to the conduction band and leaves empty donor states behind. For the same reason in the p-type material the originally empty acceptor states are partly filled by electrons from the valence band leaving mobile holes to the valence band.

If a n-type and a p- type semiconductor are placed into contact with each other, the Fermi levels of the n- ($E_{F,n}$) and p-type ($E_{F,p}$) regions must be aligned to the same level, leading to the configuration in Fig 3.2. Then the higher concentration of electrons in the n- type material will result in electrons diffusing from the n- to the p- type material, and, in a similar way, holes will diffuse from the p- to the n-type material. As the electrons diffuse into the p- type semiconductor, they leave behind positively charged atoms causing the n-type semiconductor as a whole to become positively charged. Similarly, as (positively charged) holes diffuse out of the p- type semiconductor, they leave it the p-type material negatively charged.

The result of such a charge motion is that static charges build up in both p-type and n-type materials close to the junction. This charged area is called the depletion region. The charged area forms a potential difference between both materials, inducing a current to flow. This current is called the drift current. It flows in the opposite direction to the diffusion current, and consists of electrons moving from the negatively charged p-type semiconductor towards the positively charged n-type semiconductor. As the same time, holes move from positive n-type towards the negative p-type material. Initially the diffusion current dominates the drift current. But as more and more diffusion current flows, the potential causing the drift current builds up, causing larger and larger drift currents until eventually the drift current matches the diffusion current, and they balance each other out. Now there is no net current flowing between the p-type and n-type regions.

The shift of the bands, which is just the difference between the location of the Fermi level in the n-region and the Fermi level in the p-region, is called the built-in

potential, V_{bi} . This built-in potential keeps the majority of holes in the p-region, and the electrons in the n-region. It provides a potential barrier, which prevents current flow across the junction.

The existence of the built-in electric field in the p-n junction region is the source of photovoltaic activity in the cell. Under illumination, a large number of electrons and holes are generated in the semiconductor material. Minority charge carriers (holes in the n-type and electrons in the p-type layers) generated in the depletion region of the p-n junction, or within their diffusion length from it, are swept to the opposite side of the junction by the built-in electric field of the junction. Under illumination, electrons are therefore accumulated in the n-type material and holes in the p-type material, generating voltage between the opposite sides of the p-n junction and electrical contacts attached to them, as well as current through an external load attached between the contacts.

3.2 *Polymer Solar Cells*

3.2.1 Types of OPVs

Nowadays, there are three different types of organic solar cells using organic molecules: «Dye-sensitized nanocrystalline TiO₂ solar cells», «molecular organic solar cells» and «polymer solar cells». The higher efficiencies between these types of solar cells (11%) are reported for «Dye-sensitized nanocrystalline TiO₂ solar cell», which operates with photo-electrochemical principles. Originally discovered by Gerischer and Tributsch¹⁴, but named by M.Gratzel¹⁵, who reported efficiencies in the order of 11% using TiO₂ nanocrystals to achieve large areas interface with electrodes.

Molecular organic solar cells exploit organic dyes. The active layer is deposited by vacuum evaporation techniques. Organic dyes have a high absorption coefficient and an absorption spectrum similar to solar. However, efficiencies are limited by the small diffusion length of excitons and the small charge mobility in materials. Efficiencies of around 1% achieved already in 1986 by Tang, using copper-phthalocyanine and a perylene-tetracarboxylic derivative¹⁶. Manipulating with C₆₀ could slightly improve efficiency.

Recently, the use of doped pentacene, which indicates higher mobility carriers, increased efficiency up to 2% for thin films and 4.5% for monocrystalline provisions.

The third type of organic solar cells, the «polymer solar cells», is to be debated extensively since it is the basis of this work. The original «polymer cells», which consisted of one polymer layer enclosed between two asymmetric contacts, showed low efficiencies due to insufficient charge generation in polymer layer. The discovery of photoinduced charge transfer from a p-conjugated polymer to a fullerene opened new avenues for organic photovoltaics and LEDs. This process is done with almost no deviations since it is much faster than any competitors, radiant or not, path "relaxation." Bilayer devices with conjugated polymers and C₆₀ fullerenes showed improved efficiencies. But only the light absorbed within the distance of diffusion length of excitons in interface contributed to the current.

Sudden revolutionary progress in «polymer solar cells» came with the introduction of bulk heterojunction concept. Stirring conjugated polymer with C₆₀, or a more soluble fullerene derivative, led to a three dimensional heterojunction with the ability to generate efficiently charge throughout the layer. Very soon, efficiencies up to 1% could be achieved. The morphology and improvement of interfaces between the electrical contacts are critical for the efficiency of the device. Intensive polymer engineering and improving of contacts led to a rise of the efficiencies in the order of 9%.

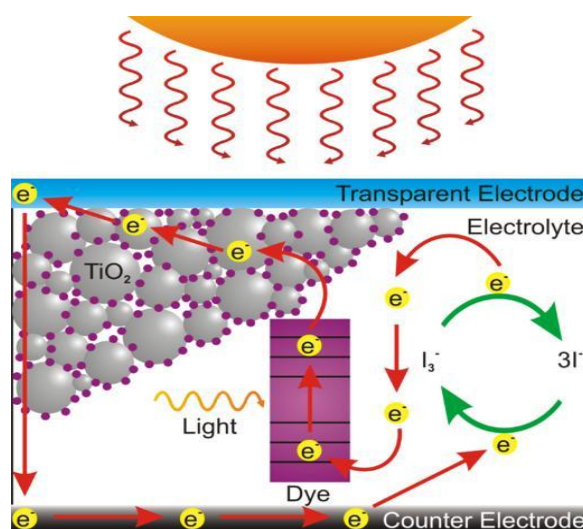


Figure 3. 1 Dye-sensitized solar cell

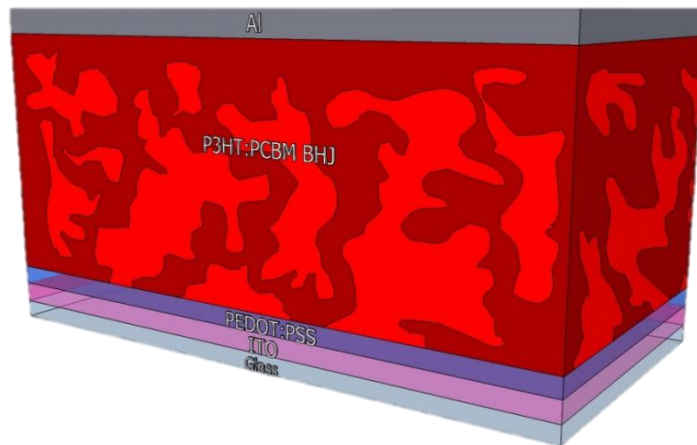


Figure 3. 2 Bulk heterojunction concept solar cell

3.2.2 Bulk heterojunction concept and operating principles

Basic principles

These are the three basic steps of light conversion into electricity by a photovoltaic cell:

- (i) Light absorption
- (ii) Charge carriers generation
- (iii) Selective transport of opposite charges on opposite contacts.

The general operating principles are the same for all photovoltaic cells, but a description for a BHJ cell of polymer-fullerene dispersion should be done.

This type of solar cell consists of a mixture of polymer-fullerene (or derivative) disposed between two planar electrodes as shown in Figure 3.2. An ITO layer deposited on glass serves as a transparent electrode of high work function, while a thin layer of metal, such as aluminum, is used as the electrode with the low work function.

The production of a photocurrent in an organic cell of this type, in which the built-in field (in rough analogy to a p-n junction) is provided by the difference in work functions of the electrodes, arises from the following phenomena (Fig.3.3)



Figure 3. 3 Conversion steps of an organic solar cell.

As mentioned previously, the photogeneration mechanism in organic semiconductor materials is very similar to that encountered in an inorganic p-n cell. A photon with energy $h\omega$ greater than the energy gap E_g can excite an electron from π to π^* orbital (HOMO-LUMO excitation). This will form an exciton, which should be separated to give the hole at one electrode (anode) and the electron at the cathode (i.e., to start the production of photocurrent). The exciton is separated at the interfaces of polymer-fullerene. We conclude that the absorption of light is directly associated with the short circuit current (I_{sc} for $V = 0$). The absorption spectrum and the thickness of the active substrate are important parameters. The thickness can not be increased above a certain limit due to the limited carrier mobility.

Charge generation occurs at the interfaces or in a p-n junction or a Schottky. As a p-n junction can be considered the mixture of polymer-polymer or polymer-fullerene, while Schottky semiconductor-metal interfaces. Only light that is absorbed in the collapse region of the interface or in the radius of the exciton diffusion length can create carriers.

The transfer of photoinduced charge (the electron) from conjugated polymer to the fullerene is an effective way to generate carriers. The photoinduced charge transport at the interface polymer-fullerene occurs in times of the order of 15 fs. This process is much faster than any radiative or non-radiative decay of electrons in conjugated polymer.

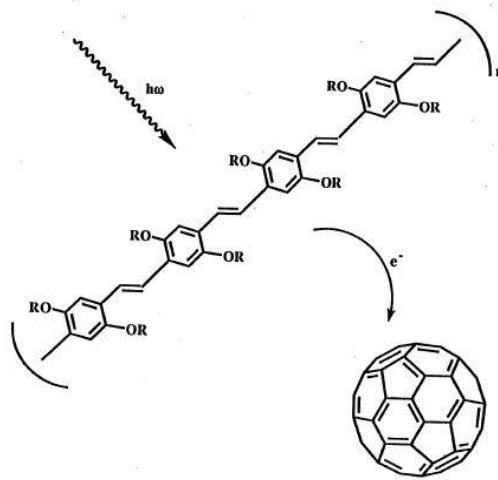


Figure 3. 4 An illustration of a photoinduced charge transport from PPV to C₆₀

Charge transport occurs in a procedure with several steps as it shown in figure 3.5

1. $D + A + h\nu \rightarrow {}^{1,3}D^* + A$	$\pi-\pi^*$ excitation of the donor
2. ${}^{1,3}D^* + A \rightarrow {}^{1,3}(D \cdots A)^*$	excitation delocalised on D-A complex, exciplex
3. ${}^{1,3}(D \cdots A)^* \rightarrow {}^{1,3}(D^{\delta+} \cdots A^{\delta-})^*$	charge transfer complex
4. ${}^{1,3}(D^{\delta+} \cdots A^{\delta-})^* \rightarrow {}^{1,3}(D^+ \cdots A^-)^*$	radical pair formation
5. ${}^{1,3}(D^+ \cdots A^-)^* \rightarrow D^+ + A^-$	charge separation

Figure 3. 5 Serial reaction for an ultra fast electron transport from a donor (p-conjugated polymer) to an acceptor (fullerene derivative). The corresponding hole transfer from a donor to an acceptor follows the same procedure.

D and A are donor and acceptor, respectively. Indicators 1,3 indicate the singlet and triplet excited states.

From thermodynamic principles, it is necessary that the potential needs the excited donor (electron) to ionized (I_D^*) is less than the sum of electron affinity of the acceptor with Coulomb interaction between the separated conditions of charge.

$$I_D^* - A_A - U_C \leq 0$$

I_D^* can be estimated from the inverse electronic affinity. That means that the LUMO of the donor is higher than the LUMO of the acceptor, neglecting Coulomb interactions.

During the third step, the charges that have been created are selectively transferred to the electrodes. The holes jump from fullerenes to polymers until they reach ITO, while the electrons from polymers to fullerene until Al contact. The conjugates polymers exhibit great mobility longitudinally to the chain, but the mobility is limited by the dialysis between the chains. Certainly, there are some factors for the efficient separation and collection of carriers, such as the association between the fullerene in the mixture, the crystallinity of the polymer, the dispersion of fullerene and will be discussed later.

MIM model

The better understanding of bulk heterojunction requires the understanding polymer diode. An easy and good model for the description of such a diode is a metal-insulator-metal (metal-insulator-metal) (MIM). The polymer may be considered to have a negligible amount inherent charge and thus be perceived as insulator. It should be noted that this assumption is inadequate in light. For contacts, we assume tunneling injection diodes. In Figure 3.6 this model is represented.

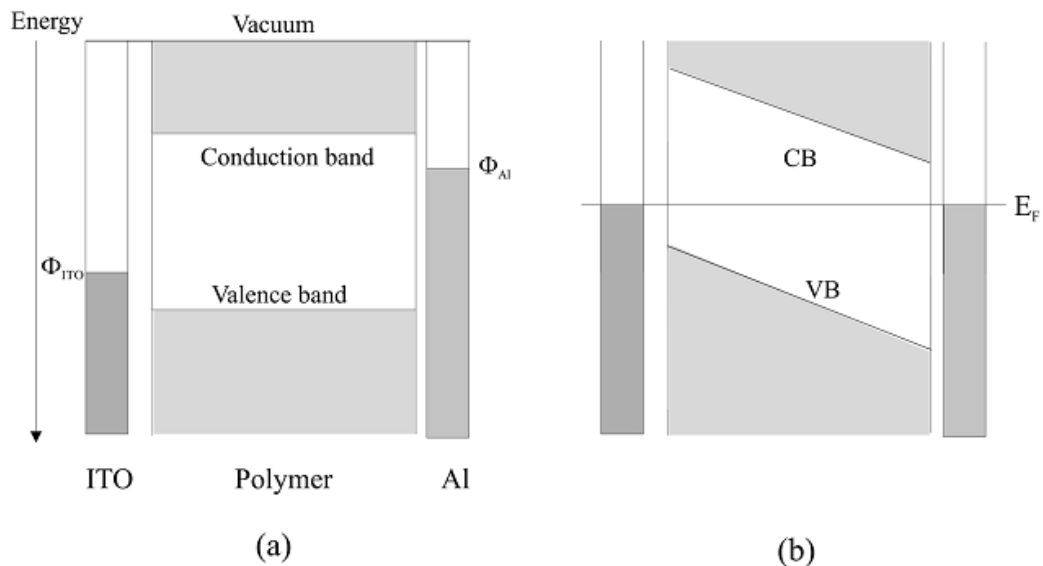


Figure 3. 6 Schematic representation of the energy levels in a polymer device (a) before the materials are placed in contact and (b) after contact with no external bias.

In Figure 3.7 is illustrated the operation a pure polymeric device under different operating conditions, through a MIM model. Figure 3.7 (a) shows the case of short circuit current (I_{sc}), where the light generates holes and electrons which are directed to contacts

ITO and aluminum respectively. The force that pushes a separation of charges is the built-in potential within the polymer substrate. The built-in potential is constant over the polymer layer and is induced by the difference in work function of contacts (as illustrated in Figure 3.6). Under illumination and open circuit conditions (Figure 3.7 (b)), the generated charges do not seem to prefer any direction. The open circuit voltage cancels the potential between the contacts. The maximum observed open circuit voltage (V_{oc}) is the difference between the work function of two contacts reduced by a factor.

Under reverse bias (negative polarity in ITO), the diode functions as photodetector (Figure 3.7 (c)). The photoinduced charges are selectively transported, induced by an external field, to the contacts, holes in ITO and electrons in Al. The diodes are very sensitive polymer photodiodes. For example, polythiophene show quantum yield of 80% at 15V potential.

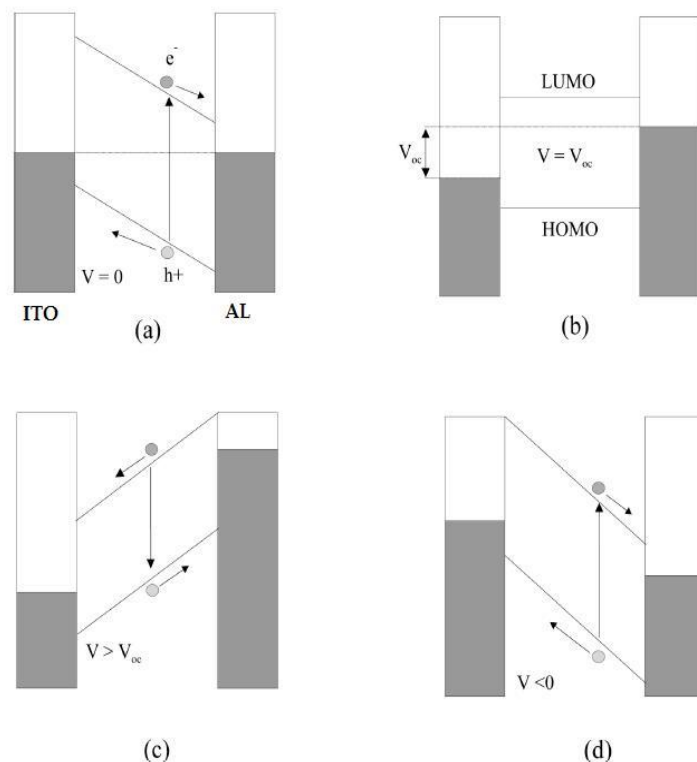


Figure 3. 7 Simple model following the MIM picture of the current-voltage characteristics of an ITO/P3HT/Al device under different working conditions. a) Under short circuit conditions, the holes are transported to the ITO, while the electrons to the Al. b) Under open circuit conditions (flat band condition at a small forward bias equal to the difference in the electrode work functions), the V_{oc} in the MIM picture is equal to the work function difference between the two electrodes c) Under forward bias greater than the difference of electrode work functions, the diode can work as a light emitting diode (LED). d) Under reverse bias, the diode can work as a photodetector (negative polarity on the ITO) .

Under forward bias, electrons inject by tunneling from aluminum to LUMO of the polymer and respectively the holes from ITO to HUMO. If electrons and holes recombine radiatively, we can observe photoluminescence. This phenomenon was first observed in 1990 by R.Friend and his team at Cambridge¹⁷. This discovery sparked a lot of research over the past decades and LED-based polymers (OLED) are one step before entering in the market.

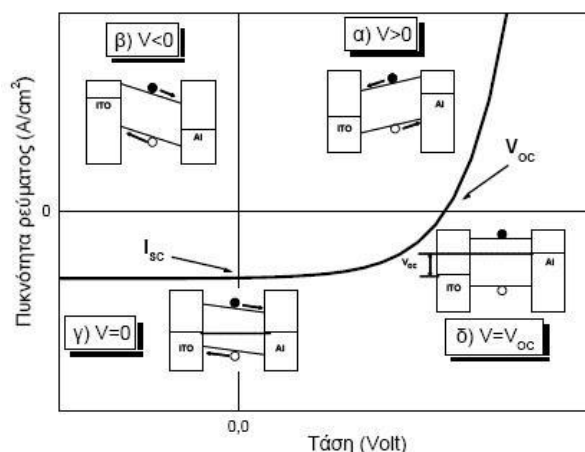


Figure 3. 8 Correlation between current-voltage characteristics and energy level of MIM model

The simulation of MIM model explains well the behavior of the polymer diode as well as the function of monolayer solar cell. However, in BHJ devices (e.g. P3HT/PCBM) the observed V_{oc} range at higher levels than the difference of the projects output ITO and Al (~ 0.4 V).

Bulk heterojunction solar cell

A bulk heterojunction solar cell consists of an active organic part with a donor and an acceptor material, the metal electrodes and the substrate. The substrate is responsible for mechanical stability and also should protect the organic material from moisture. Usually the substrate is transparent, so the light will first pass the substrate before it reaches the active material. The material of the substrate is usually glass, but it could also be a transparent plastic. The positive electrode in our device as illustrated in Figure 3.9(a) is indium tin oxide (ITO). The aluminum represents the negative electrode. The aluminum electrode is thick enough to reflect the unabsorbed light back into the device. Both electrodes have the task to transport the charges from the organic material to the electrical

connections with minimal losses. The level of the electrode work functions can be optimized for electron and hole extraction to selectively design a quality diode. If the work functions do not fit, it is possible to introduce an additional layer between the electrode and the organic material to adjust the work functions of the different materials. That's one of the tasks for PEDOT:PSS. Also, intermediate layers can block the transport of holes or electrons.

Finally, in the middle of the solar cell, the organic part is present. The organic donor and acceptor materials have different electron affinities, which means that the acceptor material rather receives electrons than releases. Whereas the donor material prefers to release electrons. The acceptor material in the presented example is PCBM. P3HT is the donor material. It absorbs most of the light in a bulk heterojunction solar cell.

The working principle of an bulk heterojunction solar cell is showed in Figure 1.1(b). If the incoming photon has an equal or higher energy than the optical bandgap in the absorber material, then there is a probability for the photon to be absorbed. The optical bandgap is defined by the difference of the band levels of the highest occupied molecular orbital (HOMO) and lowest unoccupied molecular orbital (LUMO) of the absorber material (P3HT). If the photon is absorbed, an exciton is generated. An exciton is a quasi neutral particle and contains a positive and negative charge. An exciton can diffuse maximum 20nm in its lifetime ¹⁸. If the exciton does not reach the donor acceptor interface it will recombine, and the absorbed energy is converted into thermal energy or as an emitted photon and cannot be used for power generation. If the exciton reaches the interface it can dissociate, with the electron transferring to the acceptor material. Some energy is lost due to the difference in the LUMO levels of the donor and acceptor material. The generated charges are driven by drift and diffusion to the electrodes, where they are free to move through the external circuit.

In inorganic solar cells the absorber material generates free charges, since the dielectric constant of the absorber material ($\epsilon_{Si} = 11$) is much higher compared to the organic absorber material ($\epsilon_{P3HT} = 3$). In OPV devices an acceptor and a donor material is needed to generate free charges. In a pure absorber material, excitons would be generated but not separated and therefore no photov generated charges should be visible. In this case excitons are only able to separate at impurities.

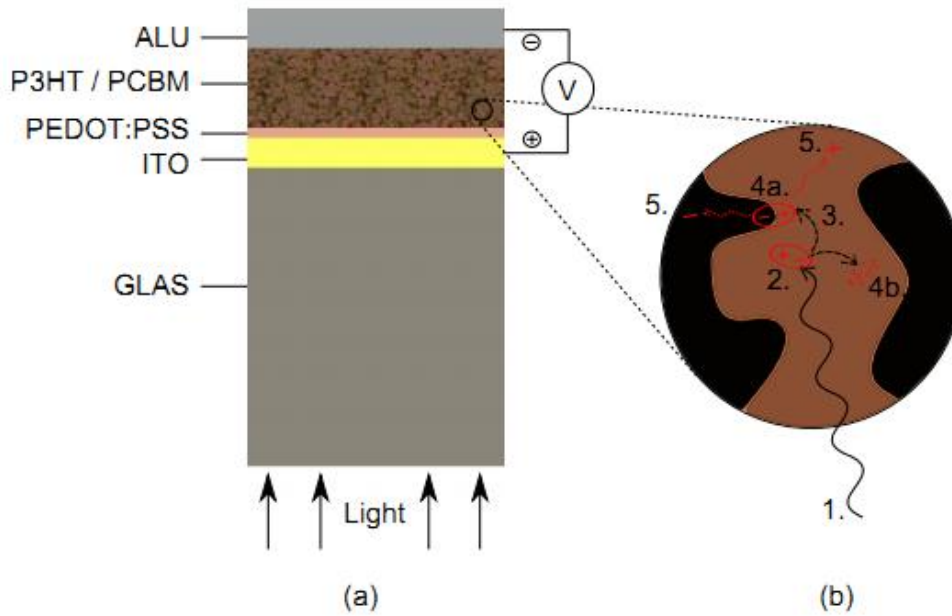


Figure 3.9 a) Intersection of a bulk heterojunction solar cell. b) Concept of the functionality of an organic solar cell: 1.Light with energy $E = h\nu$, 2.Exciton generation, 3.Exciton diffusion, 4a.Exciton dissociation, 4b.Exciton recombination, 5.Charge drift and diffusion to specific electrodes.¹⁹

According to the diffusion length of about 20 nm, the donor and acceptor material should interpenetrate each other in the nanometer scale, to keep a low probability for the recombination of the exciton. The separated charges also have a lifetime. If the thickness of the film is too high, the charges will recombine before they reach the electrodes. Therefore, the thickness of the device is limited by the mobility of the carriers in the organic semiconductor. In thin devices, on the other hand, many photons are not absorbed. Thus, there is an optimum to find, between high absorption rate and low recombination rate for separated charges. The system can be optimized by increasing the carrier mobility²⁰ and the optical absorption coefficient of the materials.

3.3 *Characteristics of a photovoltaic device*

3.3.1 Current-Voltage Characteristics

The light absorbed in the junction creates electron-hole pairs whose concentration is proportional to number of absorbed photons with energies larger than the energy gap (E_g) of the material. These electrons and holes are separated by the built-in electric field

and are responsible for the production of an electric current, I_L , called the light-generated current. By neglecting the recombination effect in the depletion region and including the effect of generation in this region, I_L can be expressed as follows:

$$I_L = q A \int_0^w G(x) dx \quad (3.1)$$

Here $G(x)$ is the generation rate of the electron-hole pairs, A is the device area, and w is the width of the depletion region. The direction (and, hence, the sign) of the light-generated current is opposite to the direction of the dark current, which can be calculated by the following equation:

$$|I_{dark}| = I_s [\exp(\frac{V}{nKT}) - 1] \quad (3.2)$$

whereas I_s is the saturation current of the diode, q the elementary charge, n the diode ideality factor, k the Boltzmann constant and T the temperature. If the light generated current is larger than the dark current, the device acts as a current source, that is, as a source of electricity. Then, the total diode current under illumination is given by the Schockley equation [9]:

$$I = I_L - I_s [\exp(\frac{V}{nKT}) - 1] \quad (3.3)$$

where, as customary for solar cells, we chose the sign of the light-generated current as positive. As can be seen from the above equation, setting I to zero, the ideal value of the open circuit voltage, V_{oc} , of a solar cell is given by:

$$V_{oc} = \frac{KT}{q} \ln(\frac{I_L}{I_s} + 1) \quad (3.4)$$

The built-in electric field separating the electrons and holes generated by light can at most provide the built-in potential, V_{bi} . Hence, the built-in voltage gives the upper bound of the open circuit voltage. The effect of the parasitic series and shunt resistances, R_S and R_{SH} due to its bulk resistivity and presence of defects can included in the Schockley equation as :

$$I = I_s \exp\left(\frac{q}{nKT}(V - IR_s)\right) - I_L + \frac{V - IR_s}{R_{SH}} \quad (3.5)$$

Figure 3.2 shows the equivalent circuit of p-n junction solar cell, in which the I-V curve of this circuit is described by the equation above. The circuit consists of the following three parts. A current source I_L that considers the light-generated current, a diode that accounts for the nonlinear voltage dependence and a shunt as well as a series resistor.

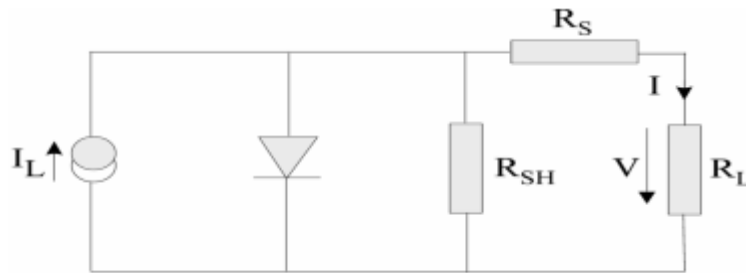


Figure 3. 2 Equivalent circuit of a p-n junction solar cell

The current source generates a current I_L up on illumination. I_L can be described as the number of free electron/hole pairs immediately after generation - before any recombination can take place. The series resistance R_S is due to the bulk resistance of the semiconductor material, the bulk resistance of the metallic contacts and the contact resistance between the metallic contacts and the semiconductor. The shunt resistance R_{SH} is caused by leakage across the p-n junction around the edge of the cell and in non-peripheral regions in the presence of defects and precipitates of foreign impurities in the junction region.

In conclusion, in the standard p-n junction solar cell, light absorption occurs via band gap excitation of electrons in the bulk of the semiconductor, charge separation in the internal electric field of the p-n junction and charge collection by transport of electrons and holes through the bulk of the semiconductor to the electrical contacts.

3.3.2 Solar cell efficiency

Respectively the net current density is given by

$$J(V) = J_{sc} - J_{dark} = J_{sc} - J_0 \left(e^{\frac{qV}{k_b T}} - 1 \right) \quad (3.6)$$

where J_s is the short-circuit current density and J_{dark} the current flowing under no illumination described by the ideal Shockley diode equation.

It is common to use I-V characteristics to indicate the efficiency of solar cells. The open-circuit voltage V_{oc} and the short-circuit current I_{sc} are determined by a given light level by the cell properties. The open circuit voltage can easily be derived from equation 3.5 given that there is no net current flowing:

$$V_{oc} = \frac{k_B T}{q} \ln \left(1 + \frac{J_{sc}}{J_0} \right) \quad (3.7)$$

An expression for the photocurrent density at short circuit can be given by

$$\begin{aligned} J_{sc} &= q \int_0^{\infty} \alpha(E) \eta_{coll}(E) [1 - R(E)] \Phi(E) d\lambda \\ &= q \int_0^{\infty} EQE(E) \Phi(E) d\lambda \end{aligned} \quad (3.8)$$

where $\Phi(E)$ is the incident spectral photon flux density and $R(E)$ the fraction of reflected photons as a function of the photon energy. $\alpha(E)$ and $\eta_{coll}(E)$ are the absorption coefficient and collection efficiency of the solar cell material, respectively. The product $\alpha(E) \times \eta_{coll}(E) \times [1 - R(E)]$ is known as the external quantum efficiency and reflects the probability of an incident photon generating one electron that is collected at the contacts. The EQE does not depend on the incident spectrum, hence it is therefore a key quantity in describing solar cell performance under different conditions.

The maximum power delivered to a load by a solar cell occurs when the product $V I$ is at its maximum, P_m , i.e. when the solar cell operates at its maximum voltage (V_m) and maximum current density (J_m). The fraction of maximum power and the product of V_{oc} and J_{sc} is defined as the fill factor, FF (Figure 2.1.4), which further can be related to the efficiency, η .

$$\eta = \frac{J_m V_m}{P_s} = \frac{J_{sc} V_{oc} FF}{P_s} \quad (3.9)$$

where P_s is the incident light power input from the sun.

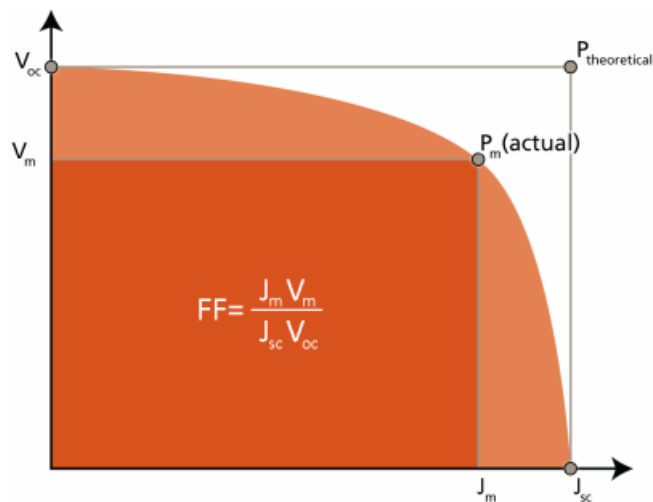


Figure 3. 10 Current-voltage characteristics and the fill factor of a solar cell

-
- ¹⁴ Gerischer, H.; Tributsch, H. *Ber. Bunsen-Ges. Phys. Chem.* 1968, 72, 437-445.
- ¹⁵ Brian O'Regan, Michael Grätzel (24 October 1991). "A low-cost, high-efficiency solar cell based on dye-sensitized colloidal TiO₂films". *Nature* **353** (6346):737–740.
- ¹⁶ Tang, C. W., Two-layer organic photovoltaic cell, *Applied Physics Letters* (1986), 48(2), 183-5.
- ¹⁷ Burroughes, J.H.,Bradley, D.D.C., Brown, A.R., Marks, R.N.,Mackay, K., Friend, R.H.,Burns, P.L., Holmes, A.B., *Nature* 347 (6293) , pp. 539-541
- ¹⁸ H. Hoppe and N. Sariciftci, \Organic solar cells: An overview," *J. Mater. Res.* , vol. 19,pp. 1924{1945, 2004.
- ¹⁹ S. Kraner, Master thesis
- ²⁰ J. Nakamura, K. Murata, and K. Takahashi, \Relation between carrier mobility and cell performance in bulk heterojunction solar cells consisting of soluble polythiophene and fullerene derivatives," *Appl.Phys.Lett.* , vol. 87, p. 132105, 2005.

Chapter 4

Plasmonic Theory

4.1 *Surface plasmons*

This part gives an introduction to surface plasmons and their origin. The text is gradually angled towards utilizing surface plasmons to increase the efficiency of photovoltaics and examples of previous work is discussed in this context.

Metal nanoparticles have been used as decorative pigments since the time of the Romans when it was discovered that silver and gold particles in the nano range embedded in dielectric surroundings exhibit unique optical properties²¹. The most famous example is maybe the Lycurgus Cup from the 4th century AD. Analysis have shown that the glass contains small amounts of nanoparticles of silver and gold approximately 70nm in diameter. The cup appears green in the reflected light and looks red when a light is shone from inside and is transmitted through the glass as seen in figure 4.1. This is due to the excitation of surface plasmon modes on the gold and silver particles embedded in it.



Figure 4. 1 The Roman Lycurgus cup from the 4th century AD in (a) reflected light and (b) transmitted light ²²

The energy of the surface plasmon resonance depends on the dielectric constants of both the nanoparticle and the surrounding medium. Mie was the first to explain the red color of colloidal gold nanoparticles in 1908, after Michael Faraday had stated in 1831 that particle size was the color-determining factor^{23,24}. Mie's biggest discovery was that

materials which real part of the dielectric function was negative, showed an anomalous peak in the absorption spectrum in form of small particles²⁵.

The reduction of the dimensions of materials has pronounced effects on the optical properties. The reason for this behaviour can generally be ascribed to two different phenomena. One is due to the quantum confinement, i.e. increased energy level spacing as the system becomes more confined, and the other is related to the surface plasmon resonance.

Metallic photonic materials demonstrate unique properties due to the existence of electro-magnetic surface waves known as surface plasmons. Surface plasmons are set to become part of the photonics revolution in which the interaction between light and matter is controlled by producing patterned structures that are periodic on the scale of the wavelength of light. Surface plasmons open up a wealth of new possibilities for photonics because they allow the concentration and propagation of light below the usual resolution limit, thus opening up such possibilities as sub-wavelength optical components.

4.1.1 Basic introduction to plasmons

A plasma is a medium with equal concentrations of positive and negative charges, of which at least one charge type is mobile. Plasmons are quanta of plasma oscillations. Plasmons are particularly related to materials that show metallic properties, i.e. that have free electrons. Consider a material of this kind in equilibrium conditions with its mobile negative charges stabilized by fixed positive ions (cations). This is what is known as the jellium model in metals. Now disturbing these ideal conditions by introducing an external electromagnetic field will give rise to a non-uniform charge distribution and hence an internal field as shown in figure 4.2. The negative charges will gain momentum from this field, but since they are simultaneously pulled back towards the positive charges and we assume they are not energetic enough to escape the electric field created by the nuclei, they end up oscillating about the positive charge distribution. This oscillation of mobile electrons from the conduction band is called a plasmon.

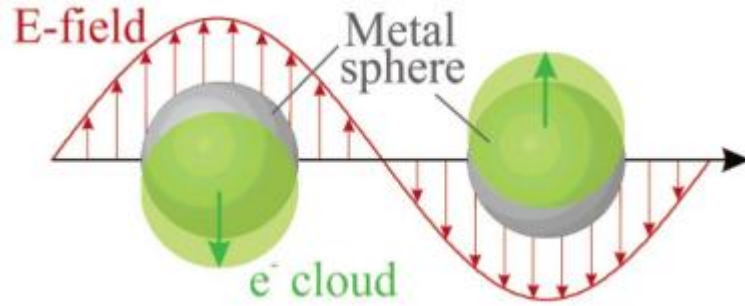


Figure 4. 2 Schematic of the plasmon oscillation of a sphere, showing the displacement of the conduction electrons relative to the nuclei²⁶

4.1.2 Bulk and surface plasmons

Most often one distinguishes only between plasmons that exist in the bulk and the ones that exist on the surface of materials. It is however, important to separate the surface-bound plasmons according to the geometry of their surroundings.

Bulk plasmons

When considering plasmons that exist in the bulk, one can think of longitudinal oscillation of free electrons in an infinite metallic medium. The frequency of this collective oscillation is called the plasma frequency, ω_p , and is given by²⁷

$$\omega_p = \sqrt{\frac{ne^2}{\epsilon_0 m}} \quad (4.1)$$

where n , e and m are the electron density, electronic charge and mass, respectively, and ϵ_0 the permittivity of free space. The bulk plasmons do not contribute in the same way as surface plasmons to the interesting optical properties of solids. This is because the probability of plasmon excitation in the bulk of a material is small since the energy of visible light provides too little momentum to the electrons in the crystal. The conduction electrons will thus simply relax back to equilibrium conditions when using light of optical wavelengths⁸. Hence, electron or x-ray spectroscopy is needed for bulk plasmon characterization²⁸.

Surface plasmon polaritons (SPPs)

Because of the long-range nature of the organizing forces in a plasma oscillation, it is reasonable to expect that for sufficiently small systems the electrons will sense the presence of the boundaries and modify their collective behavior accordingly. Indeed, surface plasmons are possible in thin films, propagating along the interface of a conductor and a dielectric medium where the real part of the dielectric function, ϵ , has opposite signs²⁹. Although analogous to bulk plasmons, these plasmons are restricted to the mobile electrons of surfaces. When the excitation of these plasmons is combined with that of a photon, a surface plasmon polariton is created. Two important properties of SPPs must be considered related to the photon-excitation of plasmons: First, there is a momentum mismatch between the SPP and the exciting photon. Second, the electromagnetic field caused by the oscillations has its maximum at the surface and will decay exponentially with the distance to the surface^{30,31}, this is said to be evanescent or near-field. Consequently, special techniques must be used to couple the light into plasmons and we can say that SPPs are non-radiative waves on the surface.

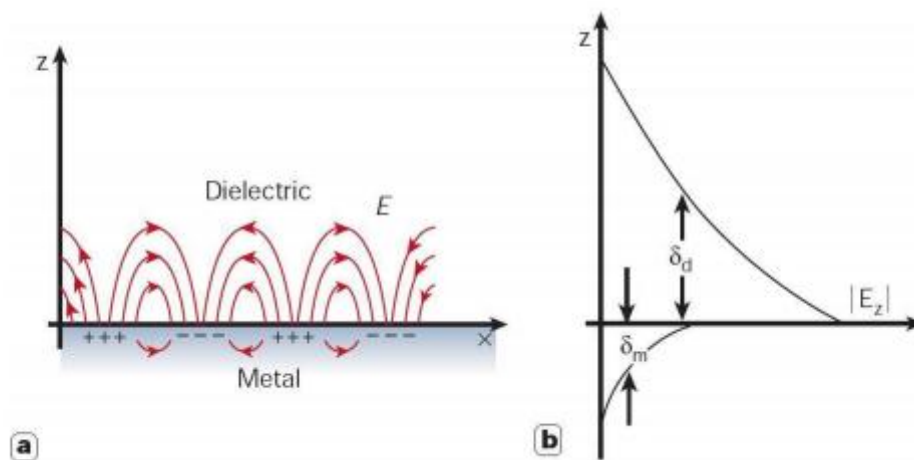


Figure 4. 3 The electric field perpendicular to the surface is enhanced near the surface and decays exponentially with distance away from it (a). This field is said to be evanescent, reflecting the bound surface plasmon modes and prevents power from propagating away from the surface (b)

At flat metal surfaces, excitations can only be achieved in the metal-dielectric interface by the use of special geometries that provides the required wavevector, k_{sp} , matching of the surface wave with that of the light producing it (e.g. Kretschmann³² or Otto³³ configuration). (3 principles: prism and total internal reflection; scattering from

topological defects like small holes in a thin film; periodic corrugations in the metal's surface).

SPPs have higher k -values and thus higher momentum ($\hbar k$) than light of the same frequency. This will give rise to a strong resonant interaction between oscillating electrons and the electro-magnetic field caused by the light, which again results in unique optical properties. This can be understood by looking at the surface plasmon dispersion relation derived from the Maxwell equations under appropriate boundary conditions¹³:

$$k_{sp} = k_0 \sqrt{\frac{\epsilon_m \epsilon_d}{\epsilon_m + \epsilon_d}} \quad (4.2)$$

where the free space vector is $k_0 = \omega/c$ and ϵ_m and ϵ_d the dielectric constants of the metal and the dielectric medium, respectively. The dielectric constant of the metal is frequency dependant and given by the Drude formula³⁴:

$$\epsilon(\omega) = 1 - \frac{\omega_p^2}{(\omega^2 + i\gamma\omega)} \quad (4.3)$$

where ω_p is given by eq (1) and is the collision frequency of the electrons usually termed the damping coefficient. Then, to get the surface plasmon k vector larger than that of light, the square root in equation 4.2 must be larger than 1. This is obtained when ϵ_m and ϵ_d have different signs. A metal will directly satisfy this criterion since its ϵ_m is negative and complex¹³. As a result of the higher momentum of SPPs than light, power will be prevented from propagating away from the surface. This is the fundamental principle behind surface plasmon waveguiding³⁵.

The frequency, ω_{sp} , of a surface plasmon on the flat surface of a nearly infinite piece of metal, can easily be determined from the frequency of a bulk plasmon in a metal, ω_p , because it corresponds to: $\text{Re } \epsilon_m(\omega_{sp}) = -\epsilon_d$, where $\epsilon_d > 0$ is the dielectric constant of the dielectric medium. By solving the equations given for the dispersion relationship and the dielectric function, the maximum frequency of the surface plasmon is found to be

$$\omega_{sp} = \frac{\omega_p}{\sqrt{1 + \epsilon_d}} = \frac{\omega_p}{\sqrt{2}} \quad (4.4)$$

for a metal with free electrons in contact with a vacuum medium. Once light has excited a surface plasmon mode on a flat metal surface it will propagate but also gradually degrade because of losses arising from absorption in the metal. The degree of degradation depends on the dielectric function of the metal at the frequency at which the SP oscillates. Silver, which is the metal with the lowest loss in the visible spectrum, has typically propagation distances in the range of 10-100 μm , and up to 1mm at wavelengths above 1.5 μm ³⁶. Most often, the surface plasmon resonance frequency ω_{sp} lies in the UV (ultra-violet) region for metals and the IR (infra-red) region for heavily doped semiconductors.

Localized surface plasmons (LSPs)

Consider again a flat metal surface. Now introducing curvature or roughness to this surface, and hence more confinement to the geometries that the surface plasmons are bound to, will give rise to a different kind of plasmon excitation. While SPPs are propagating surface modes along the interface between a thin, flat metallic film and a dielectric, localised surface plasmons (LSPs) are confined to curved metal objects, such as small metal particles or voids in metallic structures. These LSPs are characterized by frequencies which depend upon the size, shape and dielectric constant of the object to which the surface plasmon is confined. As described earlier, SPP modes can only be excited if both the frequency and wavevector of the exciting light match that of the SPP. In contrast, LSPs can be excited resonantly with light of appropriate frequency (and polarization), independent of the excitation light wavevector³⁷.

Localized surface plasmons are assigned not only to small particles, but also to features on metal surfaces. For the LSPs to be excited, the geometry to which they are confined needs to be finite and within a certain size. Variations in size and shape will affect the intensity as well as the peak-shift of the scattering produced by the particles or surface-features. The treatment of LSPs are only valid if the characteristic dimension of the system is much smaller than the wavelength of the exciting light. By considering a small metal particle, the positive charges can be assumed to be fixed while the negative charges are moving under the influence of an external field. This external field will now give rise to a displacement of the positive and negative charges, as described introductorily and shown in figure 4.2. Treating the electric field of the incoming light as constant, the problem can be treated with electrostatics rather than electrodynamics, the

approximation is said to be quasistatic. This electric field, $\sim E(t)$, on a nanoparticle with dimensions much smaller than the wavelength of the light creating it and with a dielectric constant ϵ_m , induces a dipole moment ³⁸.

$$\vec{p}(t) = \epsilon_0 \epsilon_m \alpha \vec{E}(t) \quad (4.5)$$

where ϵ_0 and ϵ_m is the dielectric constant of vacuum and is the polarizability of the particle. The internal field is given by ³⁹

$$E_i = E_0 \frac{3\epsilon_d}{\epsilon_m + 2\epsilon_d} \quad (4.6)$$

where ϵ_d is the relative permittivity of the dielectric medium and ϵ_m is the complex relative permittivity of the particle given by $\epsilon_m = \epsilon'_m + i\epsilon''_m$. This is again related to the index of refraction $N = n + ik$ by $\epsilon'_m = n^2 - k^2$ and $\epsilon''_m = 2nk$. The real term describes the polarizability, whereas the imaginary term is related to absorption and thereby dissipation of energy in the particle ⁵⁷. In fact, the imaginary term can be directly related to the absorption coefficient by $\alpha = 4\pi k/\lambda$ ⁴⁰. Materials which have negative values for the real part of the dielectric function have high reflectance and a small dissipation (i.e. $\epsilon'' = \epsilon' \ll 1$). Metals exhibit this property below its bulk plasma frequency and this is the reason for the high optical reflectivity of metals ⁴¹. The polarization, α , of a sphere can be found by

$$\alpha = 3V\epsilon_0 \frac{\epsilon_m - \epsilon_d}{\epsilon_m + 2\epsilon_d} \quad (4.7)$$

as given by Mie. Here, the dielectric constants are as given before, and r and V are the radius and volume of the particle. The polarizability is largest when the denominator in equation 2.2.7 equals to zero or is as small as possible, i.e. at the frequency where $\epsilon_m = -2\epsilon_d$ or $|\epsilon_m + 2\epsilon_d|$ is at its minimum. The solution to this is the frequency at which $\epsilon' = 2\epsilon_m$ and $\epsilon'' = 0$, which is sometimes termed the *Frölich frequency* ⁴². From equation 4.6 we see the same strong interaction of the spheres with the incident field at the same frequency. This frequency corresponds to the surface plasmon resonance, and is given by:

$$\omega_{lsp} = \frac{\omega_p}{\sqrt{1 + 2\epsilon_d}} \quad (4.8)$$

For a metal sphere in vacuum where $\epsilon_d = 1$, $\omega_{sp} = \omega_p/\sqrt{3}$. In the case of voids in the bulk of a metal, the LSP frequencies of a particle and a void of the same shape can be estimated from each other as they are related like¹⁹

$$\omega_{particle}^2 + \omega_{void}^2 = \omega_p^2 \quad (4.9)$$

Since LSPs are confined to a particle, this can result in selective photon absorption, scattering and a significant enhancement of the electromagnetic field in the particle-vicinity when the volume to which it is localized gets very small. Enhancements of 100-10.000 times the incident field has been observed in the vicinity of small metal nanoparticles and with a spatial resolution in the order of 10-50nm. The spectrum of LSPs associated with an ensemble of particles depends significantly on the size and shape of these particles, the distance between them, and also the dielectric properties of the surrounding substrate and medium¹⁹.

Most often one uses a dipole approximation where the electrons are driven to the surface of the particle as shown in figure 4.2. This is however, only applicable to very small particles, as higher order multipoles will influence the charge distribution when the particles grow bigger¹⁹. This will be explained in further details when dealing with the size and shape of the particles.

4.1.3 Extinction by metallic nanoparticles

Extinction is the sum of absorption and scattering of the incident light by the metallic nanoparticles. Ideally we want scattering processes to provide for all of the extinction, as the energy from the light is merely lost into heat when absorbed by the particles⁴³. When the incident radiation is in the frequency range near that of the surface plasmon resonance, the polarizability of the particles increases and the field lines are more strongly affected in a larger distance from the particle. As a consequence, light may

interact with the particle over a cross-sectional area larger than the geometrical cross-section of the particle. These cross-sections can be defined as follows⁴⁴

$$C_{abs} = \frac{2\pi}{\lambda} \text{Im}[\alpha] \quad (4.10)$$

$$C_{scat} = \frac{1}{6\pi} \left(\frac{2\pi}{\lambda} \right)^4 |\alpha|^2 \quad (4.11)$$

Where α is here the polarizability of the particle, given by

$$\alpha = 3V \frac{\epsilon_m - \epsilon_d}{\epsilon_m + 2\epsilon_d} \quad (4.12)$$

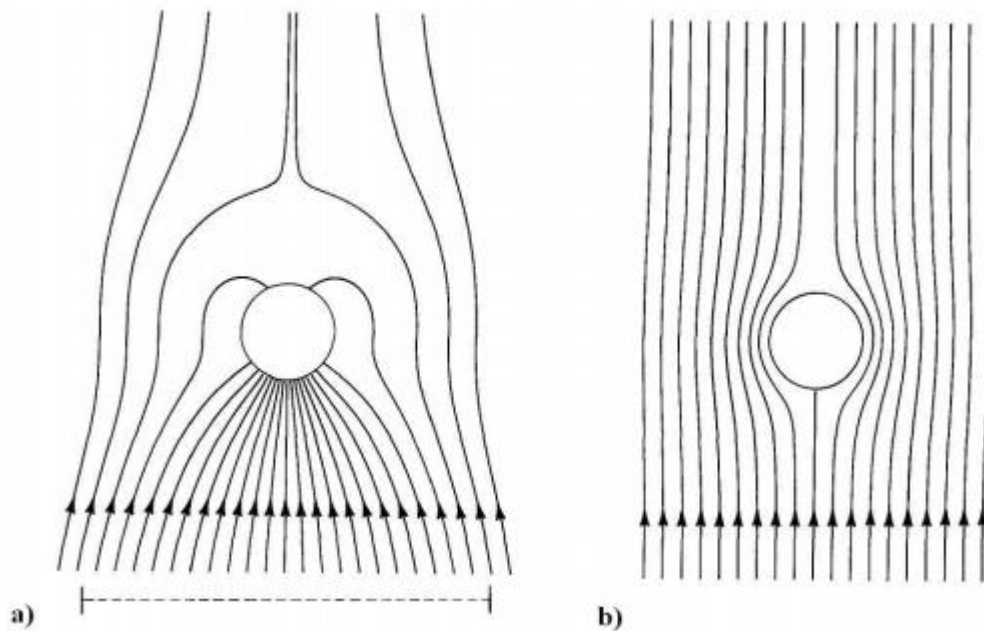


Figure 4.4 Field lines around a small aluminium sphere illuminated by light of energy 8.8eV (a) and 5eV (b). The dashed, horizontal line represents the effective radius of the sphere for absorption of light²⁹

Figure 4.4 shows the field lines of the total pointing vector (shows the magnitude and direction of energy flow in an electromagnetic field) around a small Al sphere illuminated by light of energy 8.8 eV and 5 eV, respectively. The result is an absorption

cross section 18 times greater than the geometrical cross-section of the particle in the case of 8.8 eV, which is the characteristic energy of the surface plasmon in aluminium.

A scattering efficiency, Q_{scat} can also be defined as the ratio between the scattering and geometric cross-section. This is a useful term which describes the contribution to cross-sections related to the excitation of surface plasmons, and is frequently used throughout the thesis.

$$Q_{scat} = \frac{C_{sca}}{\pi r^2} = \frac{8}{9} \cdot r^4 \cdot \left(\frac{2\pi}{\lambda}\right)^4 \cdot \left|\frac{\epsilon_m - \epsilon_d}{\epsilon_m + 2\epsilon_d}\right|^2 \quad (4.13)$$

For example, by considering Ag nanoparticles deposited on a substrate having a $Q \approx 10$ at resonance, the substrate needs only to be covered with a 10% areal density to have the possibility to fully absorb and scatter the incident light of that frequency⁴⁵.

Another popular term is the radiative efficiency Q_{rad} , which is the scattering efficiency divided by the total extinction. It is beneficial for understanding the relative significance of the processes for e.g. certain particle sizes and at certain wavelengths.

From the strong dependence upon the radius of the particle, it seems like the scattering efficiency will increase with increasing particle size. This is indeed true for particles within a certain order of size. Based on photocurrent measurements from metal islands of different sizes on SOI (silicon-on-insulator) devices, a strong size-dependence was observed on the scattering intensity of the particles⁴⁶. Larger nanoparticles have larger polarizabilities and likewise higher radiative efficiencies, both factors increasing the effective cross-section and thereby the particle interaction with the incident light. For very small metallic particles, absorption dominates the extinction processes in the material. As the particles grow larger, scattering processes will prevail until it reaches a certain size where the external electric field is no longer able to polarize the whole particle homogeneously. The result is the excitation of higher order plasmon modes (quadrupole, octopole) and radiation damping which will constitute important corrections to the quasi-static expressions given for the polarizability and cross-sections. For particles larger than the wavelength, a large fraction of the light will be reflected rather than excite plasmons

⁴⁷.

4.1.4 Tuning the plasmon resonance

One big advantage of metal nanoparticles is that their optical properties depend strongly upon the material, size and shape of the particles, which in turn makes it possible to tune the resonance peak according to area of application. Apart from the characteristics of the single particles, the environment in which the particles are dispersed is also of relevance to the optical properties. The distance between neighbouring particles as well as the refractive index of the surrounding medium has been shown to influence the spectral properties, as will be described below.

Choice of material

The first discussions on surface plasmon modes concerned colloidal silver and gold, but in the more recent years many observations have been made on surface modes in various metals and metal-like materials. As the surface plasmon resonance frequency in a particle mainly depends on the density of free electrons in the particle, the resonance can be shifted by changing the material. The SPR frequency red-shifts with decreasing free electrons density, leading to a SPR in the UV region for aluminium ($\sim 8.8\text{eV}$) and silver ($\sim 4\text{eV}$) [15], whereas it is located in the visible part of the spectrum for copper ($\sim 2.1\text{eV}$) and gold ($\sim 2.5\text{eV}$). Experiments that have been done on making alloys of silver and gold show a linear dependence of the composition on the SPR frequency and may be a convenient way of controlling the resonances in between those of the pure materials^{48,49}.

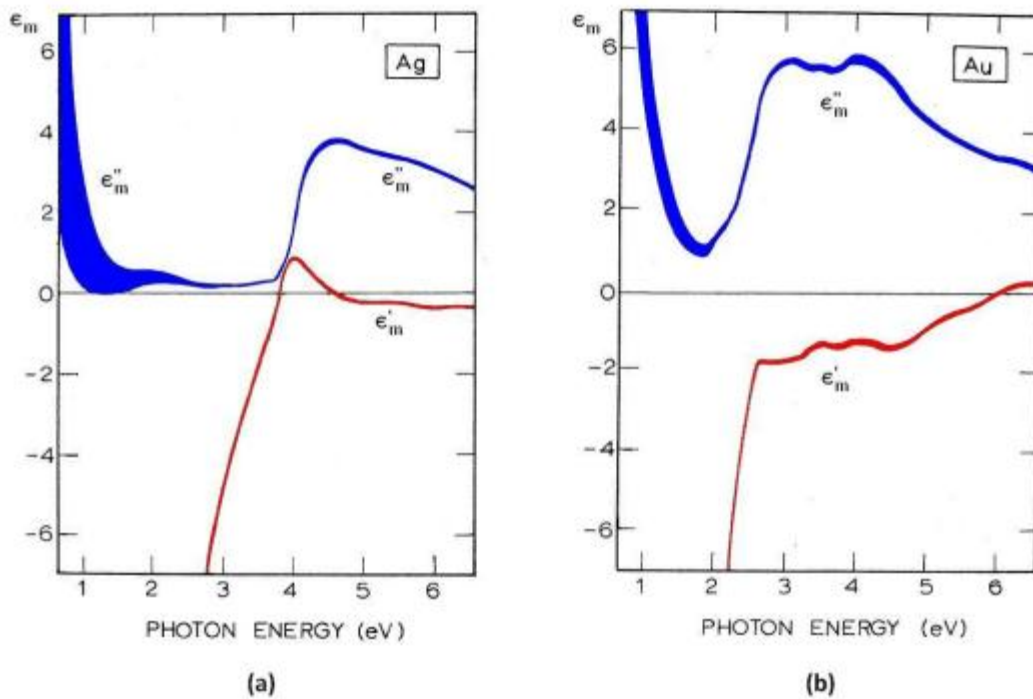


Figure 4. 5 The dielectric permittivity of silver and gold, showing the real part (ϵ'_m) with a red line and the imaginary part (ϵ''_m) with a blue line. The width of the curves represents the instrumental error of the measurements.⁵⁰

Figure 4.5 shows the dielectric constants of silver and gold. Spherical silver and aluminium particles have intense surface plasmon absorption peaks because ϵ'' is small at the frequency at which $\epsilon' = 2$, whereas gold and copper are more absorbing because of much greater values of ϵ'' ²⁸. This behaviour can be seen for silver and gold in the figure for photon energies most interesting for solar cell applications (1.12eV- \approx 4eV). As pointed out earlier, ϵ'' , which is the imaginary term of the dielectric function, is related to the absorption and hence the dissipation of heat into the metal. Silver, due to its lower ϵ'' -value and lower cost is thus a better choice than gold, although possibly negative oxidation effects must be taken care of that are not present in gold^{51,52}. As for copper it is cheaper than silver but the absorption is comparable to that of gold (has a high value for ϵ'') and there is also a big concern regarding oxidation. Aluminium being cheaper, more abundant and having a small dissipation of heat seems like an even better alternative than silver for surface plasmon applications. Experiments have shown that nanodisks of Al support strong, long-lived excitations of localized surface plasmons that have good possibilities for tuning over the entire spectral range interesting for solar applications. However, an interband transition at around 1.5eV related to the specific band structure of

Al gives rise to an enhanced instability of the LSPR at this frequency⁵³ and hence can be a problem regarding the use of aluminium in solar cell applications.

Size and shape of the particles

The decrease of the particle sizes induce limitations to the mean free path of the electrons due to the particle boundaries⁵⁴. This will result in a sharpening of the absorption peak, and as the particles grow larger they generally show a stronger resonance peak because of the increased extinction cross-section, but no significant shift of the resonance frequency is observed⁵⁵. When the particles grow beyond a certain diameter depending on the dielectric properties of the material, the resonance peak will broaden and shift to lower energies because of retardation effects and the excitation of higher order multipoles²⁸. These multipole excitations are observed as shoulders or distinct peaks in absorption spectra^{56,57,58}.

Experiments that have been done on nanosphere lithography with silver nanoparticles show that the normalized extinction can be tuned all the way from near UV, through the visible spectrum and far into the IR region (4000nm) by varying the size and shape of the particles^{59,60}. The red-shift and broadening of the absorption peak would generally be an advantage for solar cell applications, since light trapping should happen over a large wavelength range and most importantly at long wavelengths where silicon absorbs poorly. Even though an increase of the particle size leads to a larger absolute scattering cross-section, it is in fact lowered when normalized by size²⁶.

Surface plasmons are unevenly distributed in non-spherical metallic nanoparticles and this is clear from the the absorption spectra of such particles. Generally, different absorption bands correspond to oscillations along axes of different scales in the particles, each having its own polarizability. Besides spheres, silver nanoparticles have been synthesized in a wide variety of shapes including cubes, oblates, prisms, ellipsoids, rods and wires to name a few^{61,62,63,64}. In the case of ellipsoids, going from spheres to needles as the extreme cases, the electric polarizability for an incident field direction parallel to the principle axis is given as

$$\alpha = V \frac{\epsilon_m - \epsilon_d}{\epsilon_d + L(\epsilon_m - \epsilon_d)} \quad (4.14)$$

where V is the volume of the ellipsoid ($V = 4\pi/3 abc$) and L is a geometrical factor that may take any value from 0 to 1. As for spheres, the resonance occurs and a surface mode is excited when the denominator of α vanishes. For ellipsoids this occurs when ¹⁶

$$\epsilon_m = \epsilon_d \left(1 - \frac{1}{L} \right) \quad (4.15)$$

and the surface plasmon frequency is given by⁸

$$\omega_{sp} = \omega_p L \quad (4.16)$$

The number of distinct geometrical factors, L , depends on the number of principal axes in the particle. In a sphere ($a = b = c$) there is only one, hence only one extinction peak is observed. For spheroids ($a = b \neq c$) and ellipsoids ($a \neq b \neq c$) there are two and three distinct peaks, respectively, related to the number of different axes. Knowing that a deviation from a spherical shape will lower the value of the geometrical factor, the red-shift of the resonance frequency is clearly evident from equation 4.16 ¹⁶. Similarly, metallic nanorods will give rise to a splitting of the plasmon resonance corresponding to electron oscillations along the major and minor axis of the rod. As the aspect ratio of the nanorods increases, the separation of the two resonance peaks will be more pronounced ⁶⁵.

Effect of dielectric environment

As seen in the equations for the plasmon resonance and the polarizability of a metallic particle (equations 4.4 and 4.7), the dielectric constant of the surrounding medium plays a big role. An increase of the dielectric constant will lower the surface plasmon frequency and hence red-shift the resonance ^{66,67,68,38,35}. The plasmon peak of a particle in vacuum ($\epsilon_d = 1$) will accordingly get redshifted when placed on a substrate and even get further redshifted by fully embedding it in a medium of higher dielectric constant. Remembering that the dielectric constant is simply the square of the (complex) refractive index, relevant work has been done that clearly shows the linear relationship between the refractive index of an underlying substrate and the surface plasmon resonance peak ⁶⁹. Modeling done in

connection with the same work also shows the redshifting of the peak as a silver nanoparticle gradually sinks into a substrate of muscovite mica ($n = 1.6$). To simplify, the permittivity of the surrounding medium can be taken as the average of the substrate and the external medium, written as $\epsilon_d = (\epsilon_{sub} + \epsilon_{ext})/2$ ⁴⁶. All in all, fully or partially changing the dielectric surroundings of metallic nanoparticles may enhance the tunability of the surface plasmon resonance wavelength significantly³⁵. In fact, experiments have shown that introducing underlying substrates and overcoating mediums of different dielectric properties and thicknesses to silver islands, give rise to a wide tunable wavelength range of 506-1310 nm⁴⁶. A study done on coating identical nanoparticles with an oxide overcoating, shows that the localized surface plasmon frequency can be shifted 4nm per nm thickness of the oxide⁴⁰.

Metal shell particles

In the case of spherical core-shell particles composed of a dielectric core and a metal shell, plasmon modes can be excited on both the inner and outer surface of the metal shell. The plasmon resonances of these nanoshells are sensitive to the inner and outer radius of the metallic shell. Because of the finite thickness of the shell layer, the plasmons on each interface interact with each other depending on the thickness of the shell and the finite penetration depth of the exciting light. Coupling between these plasmon modes gives rise to a splitting of the plasmon resonances into two new resonances: one at lower energy, according to the symmetric polarization of the inner and outer surface, and one mode at higher energy related to the inner and outer surfaces being oppositely polarized⁷⁰. The symmetric mode has a large net dipole moment and can interact strongly with incident electromagnetic radiation in the optical regime; the antisymmetric mode however, does not couple strongly and hence is not observed in the optical spectrum. The result of introducing a dielectric core to the bulk metal particles is a red-shift of the plasmon resonance and a further redshifting as the thickness of the metallic shell-layer is reduced³⁸. The plasmon frequency can thus be tuned over a large wavelength range by changing the ratio between the inner and outer radius of the shell⁷¹.

4.1.5 Utilizing surface plasmons in solar cells

Surface plasmon effects offer a range of exciting possibilities for photovoltaics. In addition to increasing the absorption in thin films, by utilization of the reverse process, increased emission from thin films has been reported with the potential of increasing the efficiency of LEDs^{72,73,74}. Surface plasmons also raise the possibility of absorbing photons that are normally lost by transmission using the concept of up-conversion. It is the giant local field created by the excitation of surface plasmons that is responsible for this possible frequency conversion for photovoltaics^{54,53}. Also, utilizing surface plasmons in textured emitters have been proposed as a way of increasing the efficiency of thermophotovoltaic systems. This way the waste radiant heat, which is mostly emitted by sub-bandgap radiation, can be trapped more efficiently inside the system before they can be converted into electricity⁵³.

Using light of a certain frequency may excite surface plasmons on metal nanoparticles which in turn scatters the light into the underlying substrate. This emitted light will travel along a longer path within the semiconductor or even be bound to a guided mode (experience total internal reflection), and hence the possibility of absorption is increased in the relatively poor absorbing silicon⁵³. A principle schematic can be seen in figure 2.2.8.

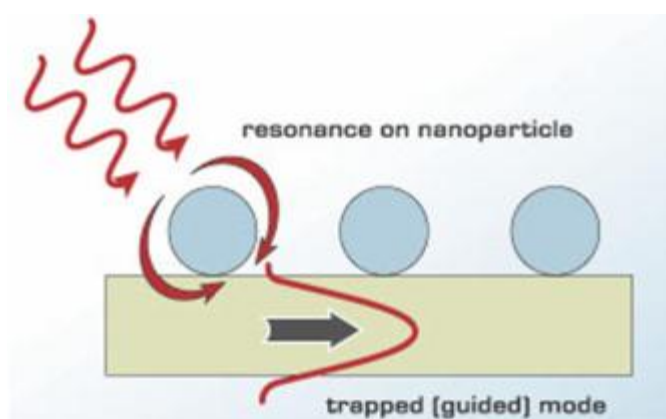


Figure 4. 6 A surface plasmon is excited on a metal nanoparticle by light of suitable frequency, which then re-radiates the light into a trapped waveguide mode in the silicon⁷⁵

The most popular way of looking at the situation is by considering a dipole located at an interface between air and silicon. The dipole mode can emit light into angles that should normally not be accessible when light goes from air into silicon. This can be

related to the fact that light scattered with high in-plane wavevectors are evanescent in air but can propagate in silicon²⁶.

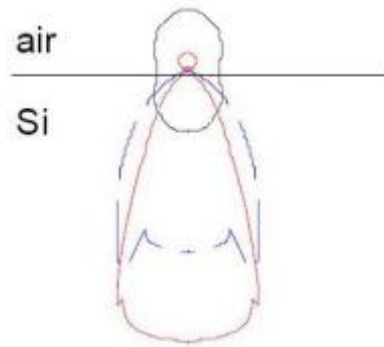


Figure 4. 7 Shows radiation patterns for a point dipole at a distance of 20 nm from a Si substrate (blue dashed line), for the case of free space (black solid line) and for a point dipole 60 nm from the Si substrate (red line)²⁷

Figure 4.7 shows the radiation patterns for a point dipole located at and above a surface with index of refraction 3.5 together with that of a dipole in free space. It is clear that only a tiny fraction of the light is radiated into the air while the vast majority (96%) goes into the silicon. This is in good agreement with experiments showing the effective energy transfer from a dipole into a higher index substrate¹⁰, and is related to the high density of optical modes in a semiconductor compared to air²⁶. As the dipole is placed at 60 nm above the same surface, a smaller but still significant fraction of the light (84%) is radiated into the silicon. The radiation is also directed less horizontally in the substrate as the distance to the dipole increases, as observed in the figure, possibly reducing the path that light travels inside the silicon. However, as the same distance is increased, the effective cross-section decreases, leaving us with a trade-off between increasing the cross-section and the fraction of light coupled into the silicon. It has been shown theoretically that the particle shape is of crucial importance in determining the light trapping efficiency, and for optimized shapes the path length in thin films were estimated to be enhanced up to a factor of 30⁷⁶.

Metallic nanoparticles as back reflectors In the case of plasmonic light trapping, metallic nanoparticles can also be deposited on the rear of solar cells as this have been found to increase the reflectance back into the silicon⁷⁷. This ensures short wavelength light to be absorbed in the silicon before reaching the particles, rather than being lost as it tends to be dissipated as heat in the metallic nanoparticles.

Plasmonic light trapping by different mechanisms The enhanced absorption in plasmonic solar cells is usually ascribed the increased optical path length inside the wafer, caused by the light being reemitted in directions along the wafer after the interaction with small metal nanoparticles ⁷⁸. It is possible however, that the electric field created in the immediate vicinity of the particles can excite electron-hole pairs without phonon assistance ⁷⁹. As opposed to the former approach, this absorption mechanism is based on a direct generation where the conservation of momentum is preserved through a transfer of momentum to the metal particle instead of through phonons. However, as simulations have shown ^{80,81}, the near-field of the particle resides outside of the semiconductor volume when the particles are deposited on top of the surface. Hence, to get the biggest contribution from the direct carrier generation and to study the effects more thoroughly, the particles should be fully embedded inside the active region of the semiconductor, as shown in figure 4.8b. The direct absorption gives an extra contribution to the indirectly generated electron-hole pairs. This effect may constitute important corrections to the total absorption in plasmonic solar cells.

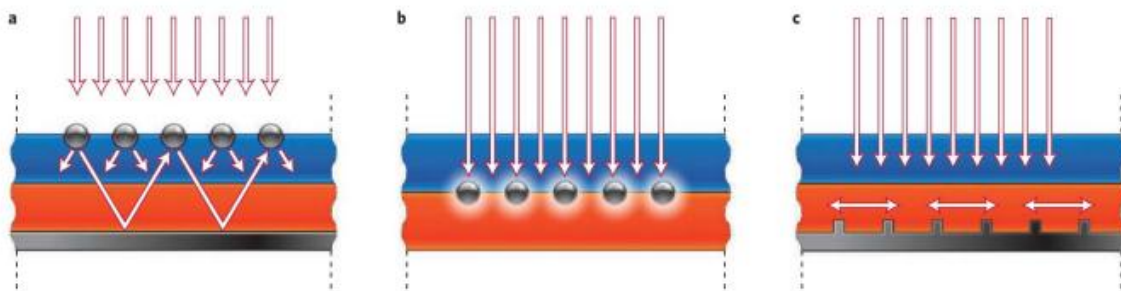


Figure 4. 8 Different geometries for plasmonic light trapping in thin-film solar cells - (a) scattering from metal nanoparticles into high angles in the semiconductor, causing increased optical path lengths in the cell. (b) The near-field of the excited metal nanoparticles causes the direct generation of electron-hole pairs. (c) Excitation of surface plasmon polaritons at the metal/semiconductor interface ensures the coupling of incident light to photonic modes propagating in the semiconductor layer plane.⁸²

²¹ Luis M. Liz-Marzán. Nanometals: Formation and color. *Materials Today*, 7:26–31, 2004. 29, 61, 114, 115

²² Tim Kelf. Surface plasmon polaritons. 7, 29

-
- ²³ Kenneth Klabunde. *Nanoscale Materials in Chemistry*. Wiley-Interscience, first edition, 2001. 29
- ²⁴ Guozhong Cao. *Nanostructures & Nanomaterials - Synthesis, Properties & Applications*. Imperial College Press, 57 Shelton Street, London, UK, 2004. 29
- ²⁵ Uwe Kreibig and Michael Volmer. *Optical properties of metal clusters*. Springer, 1995. 29, 30, 37
- ²⁶ K. L. Kelly, E. Coronado, L. L. Zhao, and G. C. Schatz. The optical properties of metal nanoparticles: The influence of size, shape, and dielectric environment. *J Phys Chem B*, 107:668–677, 2003. 7, 30, 36
- ²⁷ Charles Kittel. *Introduction to Solid State Physics*. John Wiley and Sons, New York, Chichester, seventh edition, December 1996. 30
- ²⁸ Brian J. Soller, Howard R. Stuart, and Dennis G. Hall. Energy transfer at optical frequencies to silicon-on-insulator structures. *Opt. Lett.*, 26(18):1421–1423, 2001. 30, 42
- ²⁹ Harry A. Atwater and Albert Polman. The optical properties of metal nanoparticles: The influence of size, shape, and dielectric environment. *MRS Bulletin*, 30(3):385–389, 2005. 31
- ³⁰ Harry A. Atwater and Albert Polman. The optical properties of metal nanoparticles: The influence of size, shape, and dielectric environment. *MRS Bulletin*, 30(3):385–389, 2005. 31
- ³¹ Luis Prill Sempere. Surface plasmon polaritons (spp) and their use in subwave-length optics. Term paper for Physics of Nanostructures. 31, 32
- ³² Paras N. Prasad. *Nanophotonics*. Wiley-Interscience, 2004. 31
- ³³ Andreas Otto. Excitation of nonradiative surface plasma waves in silver by the method of frustrated total reflection. *Zeitschrift für Physik A*, 216:398–410, 1968. 31
- ³⁴ Craig F. Bohren and Donald R. Huffman. *Absorption and scattering of light by small particles*. John Wiley and Sons, Inc., Weinheim, Germany, 1983. 7, 31, 33, 34, 35, 36, 37, 73, 109, 115, 119
- ³⁵ Stefan A. Maier, Paul E. Barclay, Thomas J. Johnson, Michelle D. Friedman, and Oskar Painter. Low-loss fiber accessible plasmon waveguide for planar energy guiding and sensing. *Appl. Phys. Lett.*, 84(25):3990–3992, 2004. 32
- ³⁶ William L. Barnes, Alain Dereux, and Thomas W. Ebbesen. Surface plasmon sub-wavelength optics. *Nature*, 424:824 – 830, 2003. 7, 31, 32
- ³⁷ Anatoly V Zayats and Igor I Smolyaninov. Near-field photonics: surface plasmon polaritons and localized surface plasmons. *Journal of Optics A: Pure and Applied Optics*, 5(4):S16, 2003. 32, 33
- ³⁸ David Blazquez Sanchez. *The Surface Plasmon Resonance of Supported Noble Metal Nanoparticles: Characterization, Laser Tailoring, and SERS Application*. PhD thesis, The University of Kassel, Germany, 2007. 33
- ³⁹ Leung Tsang, Jin Au Kong, and Kung-Hau Ding. *Scattering of electromagnetic waves: Theories and applications*. Wiley-Interscience, 2000. 33
- ⁴⁰ Martin Green. *Silicon Solar Cells - Advanced Principles & Practice*. Centre for Photovoltaic Devices and Systems, UNSW, Sydney, N.S.W. 2052m, Australia, 1995. 33
- ⁴¹ Supriya Pillai. *Surface plasmons for enhanced thin-film silicon solar cells and light emitting diodes*. PhD thesis, School of photovoltaic and renewable energy engineering, University of New South Wales, Australia, 2007. 8, 33, 51, 52

-
- ⁴² Craig F. Bohren and Donald R. Huffman. Absorption and scattering of light by small particles. John Wiley and Sons, Inc., Weinheim, Germany, 1983. 7, 31, 33, 34, 35, 36, 37, 73, 109, 115, 119
- ⁴³ R. H. Ritchie. Plasma losses by fast electrons in thin films. *Phys. Rev.*, 106(5):874–881, Jun 1957. 34
- ⁴⁴ R. H. Ritchie. Plasma losses by fast electrons in thin films. *Phys. Rev.*, 106(5):874–881, Jun 1957. 34
- ⁴⁵ K. R. Catchpole and A. Polman. Plasmonic solar cells. *Opt. Express*, 16(26):21793–21800, 2008. 8, 15, 35, 37, 41, 42, 61, 119
- ⁴⁶ Howard R. Stuart and Dennis G. Hall. Enhanced dipole-dipole interaction between elementary radiators near a surface. *Phys. Rev. Lett.*, 80(25):5663–5666, Jun 1998. 35, 40, 119
- ⁴⁷ Craig F. Bohren and Donald R. Huffman. Absorption and scattering of light by small particles. John Wiley and Sons, Inc., Weinheim, Germany, 1983. 7, 31, 33, 34, 35, 36, 37, 73, 109, 115, 119
- ⁴⁸ Kazutaka Baba, Toshiaki Okuno, and Mitsunobu Miyagi. Silver-gold compound metal island films prepared by using a two-step evaporation method. *Appl. Phys. Lett.*, 62(5):437–439, 1993. 35
- ⁴⁹ S. Link, Z. L. Wang, and M. A. El-Sayed. Alloy formation of gold-silver nanoparticles and the dependence of the plasmon absorption on their composition. *The Journal of Physical Chemistry B*, 103(18):3529–3533, 1999. 35
- ⁵⁰ B. Johnson and R. W. Christy. Optical constants of the noble metals. *Phys. Rev. B*, 6(12):4370–4379, Dec 1972. 7, 36, 73
- ⁵¹ D. J. Nash and J. R. Sambles. Surface plasmon-polariton study of the optical dielectric function of silver. *Journal of Modern Optics*, 43:81–91, 1996. 35, 36
- ⁵² M. D. McMahon, H. M. Meyer, R. Lopez, L. C. Feldman, and R. F. Haglund. Rapid tarnishing of silver nanoparticles in ambient laboratory air. *Applied Physics B: Lasers and Optics*, 80(7):915–921, 2005. 36, 77, 116
- ⁵³ Langhammer C., Schwind M., Kasemo B., and Zoric' I. Localized surface plasmon resonances in aluminum nanodisks. *Nano Letters*, 8(5):1461–1471, 2008. 36
- ⁵⁴ U. Kreibig and C. v. Fragstein. The limitation of electron mean free path in small silver particles. *Zeitschrift für Physik A Hadrons and Nuclei*, 224(4):307–323, 1969. 36
- ⁵⁵ F. J. Beck and K. R. Catchpole. Red-shifting the surface plasmon resonance of silver nanoparticles for light trapping in solar cells. In *Mater. Res. Soc. Symp. Proc. Vol.*, volume 1101. Materials Research Society conference, San Francisco, 2008. 36, 37, 40
- ⁵⁶ K. L. Kelly, E. Coronado, L. L. Zhao, and G. C. Schatz. The optical properties of metal nanoparticles: The influence of size, shape, and dielectric environment. *J Phys Chem B*, 107:668–677, 2003. 7, 30, 36
- ⁵⁷ Jack J. Mock, David R. Smith, and Sheldon Schultz. Local refractive index dependence of plasmon resonance spectra from individual nanoparticles. *Nano Letters*, 3(4):485–491, 2003. 36, 37
- ⁵⁸ Johanna Jacoba Penninkhof. Tunable plasmon resonances in anisotropic metal nanostructures. PhD thesis, Utrecht University, Netherlands, 2006. 33, 36, 37, 38, 41
- ⁵⁹ A Haes, J. Haynes, C. L. McFarland, A. D. Schatz, G. C. Van Duyne, and R. P. Zou. Plasmonic materials for surface-enhanced sensing and spectroscopy. *MRS Bulletin - Materials research society*, 30(5):368 – 375, 2005. 33, 36

-
- ⁶⁰ Traci R. Jensen, Michelle Duval Malinsky, Christy L. Haynes, and Richard P. Van Duyne. Nanosphere lithography: Tunable localized surface plasmon resonance spectra of silver nanoparticles. *J. Phys. Chem. B*, 104(45):10549–10556, 2000. 36, 38
- ⁶¹ Rongchao Jin, YunWei Cao, Chad A. Mirkin, K. L. Kelly, George C. Schatz, and J. G. Zheng. Photoinduced Conversion of Silver Nanospheres to Nanoprisms. *Science*, 294(5548):1901–1903, 2001. 12, 37, 111
- ⁶² Yugang Sun and Younan Xia. Shape-controlled synthesis of gold and silver nanoparticles. *Science*, 298(5601):2176–2179, 2002. 37
- ⁶³ Y. Sun, B. Mayers, and Y. Xia. Metal nanostructures with hollow interiors. *Advanced Materials*, 15(7-8):641–646, 2003. 37
- ⁶⁴ Sang Hyuk Im, Yun Tack Lee, Benjamin Wiley, and Younan Xia. Large-scale synthesis of silver nanocubes: The role of hcl in promoting cube perfection and monodispersity. *Angewandte Chemie International Edition*, 44(14):2154–2157, 2005. 37
- ⁶⁵ Eliza Hutter and Janos H. Fendler. Exploitation of localized surface plasmon resonance. *Adv. Mater.*, 16(19):1685–1706, 2004. 37
- ⁶⁶ G. Xu, M. Tazawa, P. Jin, S. Nakao, and K. Yoshimura. Wavelength tuning of surface plasmon resonance using dielectric layers on silver island films. *Appl. Phys. Lett.*, 82(25):3811–3813, 2003. 37, 38
- ⁶⁷ H. Mertens, J. Verhoeven, A. Polman, and F. D. Tichelaar. Low-loss fiber accessible plasmon waveguide for planar energy guiding and sensing. *Appl. Phys. Lett.*, 85(8):1317–1319, 2004. 37
- ⁶⁸ Jack J. Mock, David R. Smith, and Sheldon Schultz. Local refractive index dependence of plasmon resonance spectra from individual nanoparticles. *Nano Letters*, 3(4):485–491, 2003. 36, 37
- ⁶⁹ Michelle Duval Malinsky, K. Lance Kelly, George C. Schatz, and Richard P. Van Duyne. Nanosphere lithography: Effect of substrate on the localized surface plasmon resonance spectrum of silver nanoparticles. *J. Phys. Chem. B.*, 105:2343–2350, 2001. 37
- ⁷⁰ E. Prodan, C. Radloff, N. J. Halas, and P. Nordlander. A hybridization model for the plasmon response of complex nanostructures. *Science*, 302(5644):419–422, 2003. 38
- ⁷¹ S. J. Oldenburg, R. D. Averitt, S. L. Westcott, and N. J. Halas. Nanoengineering of optical resonances. *Chemical Physics Letters*, 288(2-4):243–247, 1998. 38
- ⁷² W. L. Barnes. Electromagnetic crystals for surface plasmon polaritons and the extraction of light from emissive devices. *J. Lightwave Technol.*, 17(11):2170, 1999. 41
- ⁷³ K. R. Catchpole, S. Pillai, and K. L. Lin. Novel applications for surface plasmons in photovoltaics. In *Photovoltaic Energy Conversion, 2003. Proceedings of 3rd World Conference on*, volume 3, pages 2714–2717 Vol.3, 2003. 8, 41, 42
- ⁷⁴ S. Pillai, K. R. Catchpole, T. Trupke, G. Zhang, J. Zhao, and M. A. Green. Enhanced emission from silicon-based light-emitting diodes using surface plasmons. *Applied Physics Letters*, 88(16):161102, 2006. 38, 39, 40, 41
- ⁷⁵ K. R. Catchpole, S. Pillai, and K. L. Lin. Novel applications for surface plasmons in photovoltaics. In *Photovoltaic Energy Conversion, 2003. Proceedings of 3rd World Conference on*, volume 3, pages 2714–2717 Vol.3, 2003. 8, 41, 42

-
- ⁷⁶ K. R. Catchpole and A. Polman. Design principles for particle plasmon enhanced solar cells. *Applied Physics Letters*, 93(19):191113, 2008. 42, 119
- ⁷⁷ K. R. Catchpole and A. Polman. Design principles for particle plasmon enhanced solar cells. *Applied Physics Letters*, 93(19):191113, 2008. 42, 119
- ⁷⁸ S. Pillai, K. R. Catchpole, T. Trupke, and M. A. Green. Surface plasmon enhanced silicon solar cells. *Journal of Applied Physics*, 101(9):093105+, 2007. 8, 15, 38, 39, 42, 43, 44, 51, 119, 121
- ⁷⁹ M. Kirkengen, J. Bergli, and Y. M. Galperin. Direct generation of charge carriers in c-si solar cells due to embedded nanoparticles. *Journal of Applied Physics*, 102(9):093713, 2007. 43
- ⁸⁰ S. H. Lim, W. Mar, P. Matheu, D. Derkacs, and E. T. Yu. Photocurrent spectroscopy of optical absorption enhancement in silicon photodiodes via scattering from surface plasmon polaritons in gold nanoparticles. *Journal of Applied Physics*, 101(10):104309, 2007. 43
- ⁸¹ D. Derkacs, S. H. Lim, P. Matheu, W. Mar, and E. T. Yu. Improved performance of amorphous silicon solar cells via scattering from surface plasmon polaritons in nearby metallic nanoparticles. *Applied Physics Letters*, 89(9):093103, 2006. 43, 119, 120, 122, 123
- ⁸² Harry A. Atwater and Albert Polman. Plasmonics for improved photovoltaic devices. *Nat Mater*, 9:205–213, 2010. 8, 28, 43

Chapter 5

Experimental procedures

In this chapter, the process of manufacturing of BHJ plasmonic organic photovoltaic device will be described and analyzed. The preparation of materials used, the fabrication and characterization procedures are presented.

5.1 Materials preparation

Preparation of Active Blend

Regioregular P3HT was purchased from Rieke Metals and PCBM was purchased from Nano-C. Regioregular P3HT and PCBM were dissolved in dichlorobenzene in a 1:1 ratio and stirred for 24h at 100° C. Then the metallic NPs were blended into the P3HT:PCBM solution at different weight ratios (wt%), determined from the initial concentration of Au NPs in ethanol which was $5 \times 10^{-5} \text{ mg mL}^{-1}$. Composite blends with many different concentration (wt%) of Ag NPs and Au NPS were prepared.

Surfactant-free NPs preparation

The generation of NPs was performed by ultrafast laser ablation of metallic targets (Au/99.99% ,Ag/99.98%). This technique provides the possibility of generating a large variety of NPs that are free of both surface-active substances and counter-ions.⁸³ The targets were placed into a Pyrex cell and covered by a layer of absolute ethanol (Figure 5.1) A femtosecond (pulse duration $\approx 100 \text{ fs}$ and repetition rate $\approx 1 \text{ kHz}$) laser beam was focused onto the target through the ethanol layer. The cell was mounted on a computer-driven XY stage and translated during laser exposure. More experimental details can be found elsewhere.⁸⁴ Laser irradiation gives rise to a high temperature gradient in the metal bulk and melting of a thin layer of the target. A fraction of the molten layer of the target is dispersed into the liquid as NPs. The morphology of NPs was characterized with high-resolution transmission electron microscopy (HRTEM).

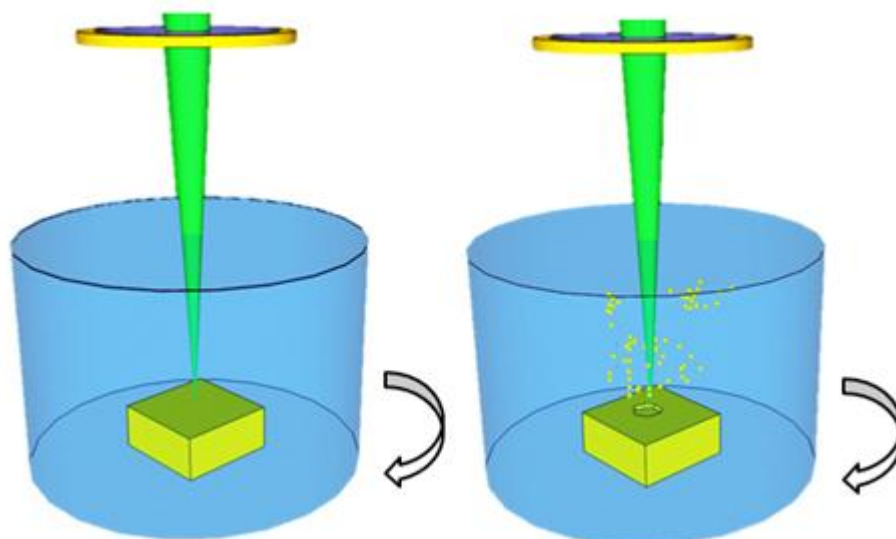


Figure 5. 1 Schematic illustration of laser-assisted production of surfactant-free NPs

Synthesis of Gold nanoparticles (AuNPs) stabilized with P3HT

Firstly, AuNPs stabilised with tetraoctylammonium bromide (TOAB) were prepared in a water/toluene two-phase system. In detail, an aqueous solution of hydrogen tetrachloroaurate (3 ml, 30 mM) was mixed with a solution of TOAB (8 ml, 50 mM) in toluene and stirred until the tetrachloroaurate was quantitatively transferred into the organic phase. Then, a freshly prepared aqueous solution of sodium borohydride (2,5 ml, 0.4 M) was slowly added with vigorous stirring. After further stirring for 20 min the ruby coloured organic phase obtained was separated and washed once with dilute sulphuric acid (20 ml, 0.1 M) twice with sodium carbonate solution (20 ml, 1 M), then with water (20 ml) and dried with anhydrous sodium sulphate. Finally, 100 μ l of a freshly prepared solution of P3HT (2.5 mg in 600 μ l of chloroform) were added to a mixture of 1 ml of the TOAB stabilized AuNPs and 500 μ l of toluene. The nanoparticles solution was stirred for 1 hour and stored at room temperature.

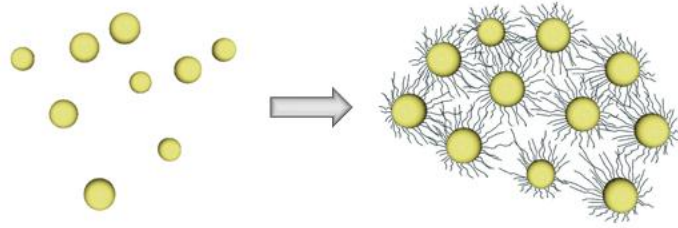


Figure 5. 2 Schematic illustration of NPs stabilized with P3HT

5.2 *Device Fabrication*

There are six basic steps which lead from the substrate to the integrated device:

- Cleaning of substrates
- Deposition of PEDOT: PSS
- Active Layer Deposition
- «Solvent annealing»
- Deposition of Cathode
- «Thermal annealing»

The three types of the completed devices are illustrated in figure 5.3 .In the next subchapters the details of each step for the optimal production method are presented.



Figure 5. 3 The three types of completed devices

Cleaning of substrates

Glass substrates coated with ITO and 15x15x0.7 mm size were purchased by Luminescence Technology Corp. The ITO layer is of ... thickness and a surface resistance of 15 Ω /sq.

The cleaning procedure of ITO-coated glass substrates from any surface contamination, is constituted by six steps:

- Placement of the substrates in the holder and immersion in a solution of soap (10%)-deionized water in a beaker. Ultrasonic bath for 10 minutes.
- Rinse with deionized water.
- Immersion in acetone into a beaker. Ultrasonic bath for 10 minutes.
- Rinse with deionized water.
- Immersion in isopropanol in a beaker. . Ultrasonic bath for 10 minutes.
- Transfer the samples in a Petri dish. Placement of the dish in oven at 120 °C for 10 minutes for drying. The right side is easy found by using a multimeter as such the ITO layer is not visible to the naked eye.

Deposition of PEDOT: PSS

As mentioned above PEDOT: PSS performs three functions-smoothing the surface of ITO, produces a better interlayer with P3HT («energy match») and most importantly, acts as the transport layer only holes («electron blocking»). Ensuring a good layer of PEDOT: PSS is of great importance for an efficient layout. PEDOT: PSS requires a very clean and hydrophilic surface in order to make the best quality of coating layer, which can be achieved by the cleaning referred above.

PEDOT: PSS was purchased by HC Starck Clevios P AI 4083. Afterwards it was filtered with filters 0.45 micron PVDF, before a deposition, to remove any imperfection.

The deposition occurred by spin coating. Spin coating is a very useful technique for deposition of thin uniform films on planar substrates. It's a very simple process, illustrated in Figure 5.4. A solution is placed on the substrate, the substrate is rotated at an adjustable angular velocity resulting to the spreading of the liquid due to centripetal force. The rotation continues for an adjustable time. The time and the speed of rotation determine the amount of solution that will remain on the substrate (and hence the layer thickness) as shown by the formula 5.1 with layer thickness (t), the (η) the viscosity of material in connection with the concentration and ω rotational speed. Once the rotation terminates the sample is allowed to dry and the procedure repeated with another solution for the manufacture of multilayer.

$$t = \frac{\eta(c)}{\sqrt{\omega}} \quad (5.1)$$

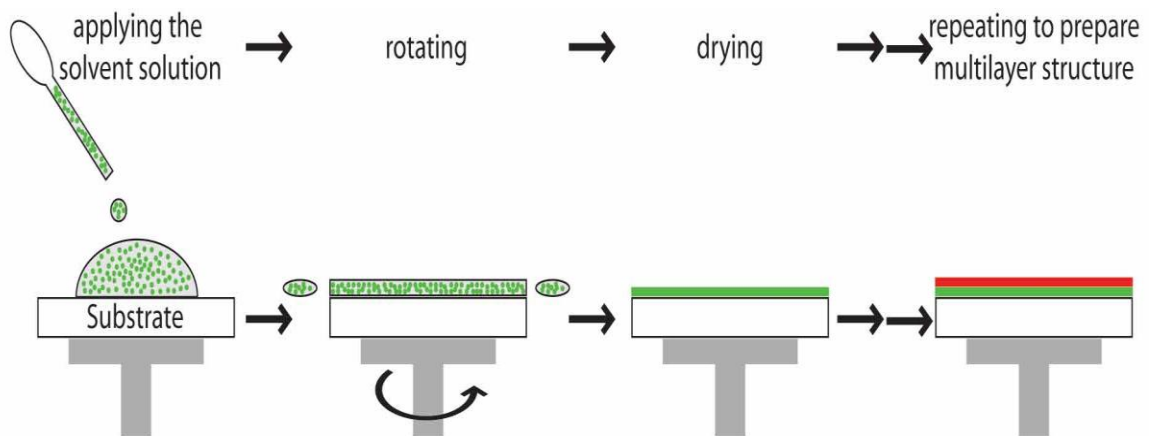


Figure 5. 4 Spin coating procedure

Studies have shown that this type of PEDOT: PSS layer is optimal at 5000rpm for 30sec to achieve layer thickness $\sim 30\text{nm}$ (and surface resistance $<800/\text{sq}$). To minimize the use of material (and therefore the cost) deposition can be done by pipetting, leaving only 30ml center of the substrate. To maximize the performance, the samples with imperfections that can be observed by the naked eye, rejected.

Following the spin coating process, a stripe of PEDOT: PSS layer at one of the edges of the square substrate, swabbed with a cotton bud wetted with deionized water. This strip is removed in order to ensure the contact of the electrode with the ITO layer and not with PEDOT: PSS. The PEDOT: PSS removal is very easy, since it is water soluble.

The whole process carried out outside glovebox since there was no infrastructure. Finally, the substrates were placed in an oven at 120⁰C for 10 minutes in order to remove any humidity residues.

It is extremely important to note that the exposure time of PEDOT: PSS in the air should be minimized because the performance deteriorates rapidly. The humidity of the atmosphere is a negative factor because can lead to morphological changes due to the creation of an insulating layer on the surface, which is rich in PSS and deteriorate the performance.

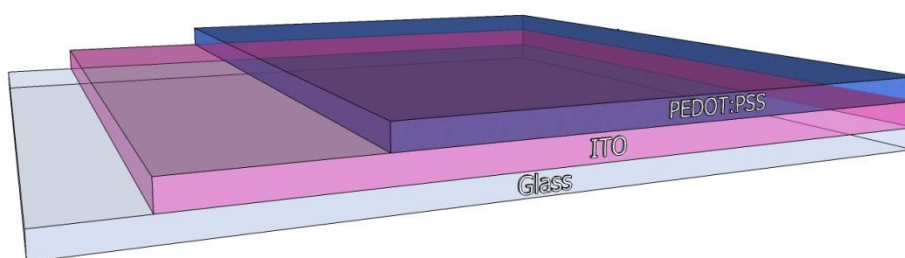


Figure 5. 5 Second production step of a device. In this figure is illustrated a microscopic view of spin coated PEDOT:PSS film on etched ITO

Deposition of Photoactive layer

The third main step in the manufacture of an organic solar cell is the deposition of the most important element in the device, the photoactive layer. After the preparation of active blend (5.1) layers of approximate thickness 100-400nm were deposited by spin coating method. The most efficient device was observed at 1000rpm until the drying of the device.

Afterwards, the stripe of photoactive layer which is above the removed PEDOT:PSS stripe, was swabbed by the same procedure and chloroform.

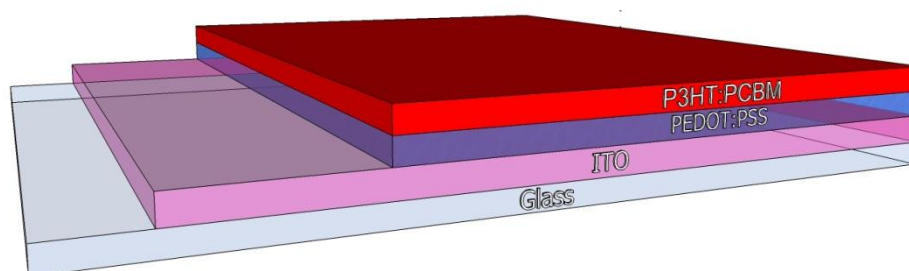


Figure 5. 6 Third production step of a device. Microscopic view of spin coated P3HT:PCBM film.

Deposition of Cathode

A different deposition technique is the vacuum thermal evaporation (VTE). In this process, small pieces of material, which we want to deposit, are placed in a cavity which is located within the vacuum chamber. The substrate which is to become the coating is placed on a special base over the cavity. The cavity is supplied with current, due to resistance is heated and the material pieces melt and evaporate. The vaporized molecules of the material overlay on the substrate and form the coating. The coating thickness depends on the distance of the substrate from the cavity (source evaporation) and the time of supply with electricity. The overlay can be made on specific parts of the substrate with the use of masks, leaving uncovered the points we want cover with the material (Figure 44).

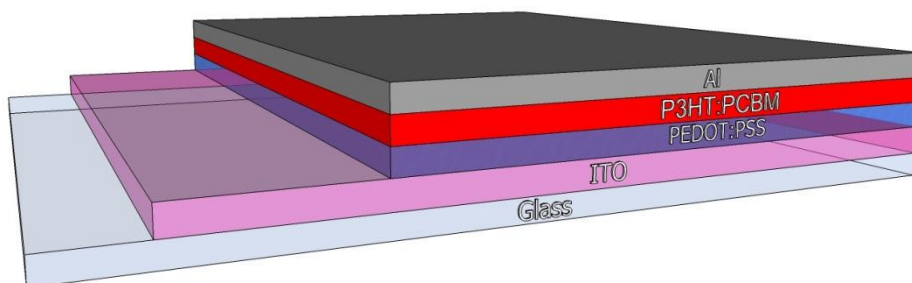


Figure 5. 7 Forth production step of a device. Microscopic view of evaporated Al film on top.

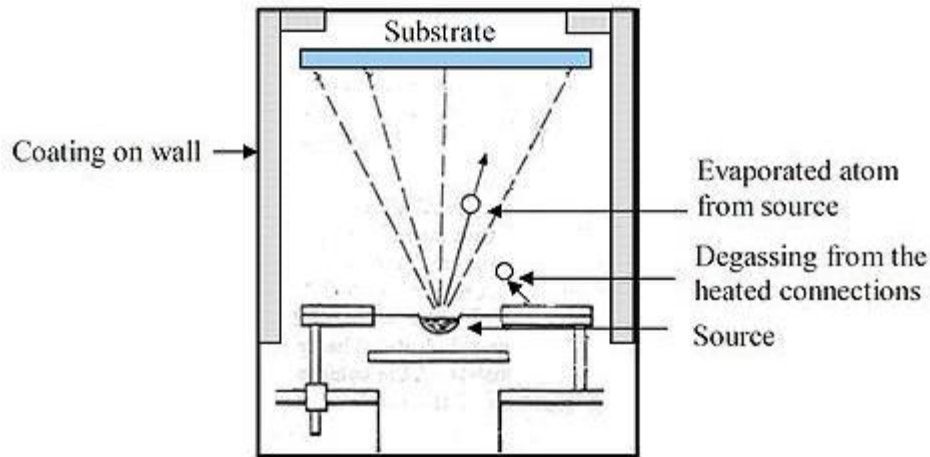


Figure 5. 8 Vacuum chamber

Tests with different times of current supply and different amounts of aluminum were made. The best results were taken with 18mg aluminum and evaporation time 35 seconds.

The entire cathode evaporation procedure is described below:

- Immediately after the deposition of the active layer, the samples are placed in the specially designed mask, which exposes the area in which we want to deposit the aluminum layer. Every sample is numbered in order to be distinguished.

Afterwards, the mask is screwed on the arm of the vacuum chamber, in a specific distance from the cavity. Finally the cavity is filled with the amount of aluminum we desire.

- The chamber is sealed and the electric parts are put in operation by turning the main switch on the display ON.
- As soon as the vacuum indication in the TM1 channel of COMBIVAC CM 31 reaches $\sim 9 \times 10^{-3}$ mbar we turn on the turbo pump and the water supply. The moment that the first channel terminates we switch to PM channel in order to monitor the high vacuum values.
- After ~ 3 hours of vacuum pumping and vacuum order of 10^{-6} mbar, the evaporation is ready to take place. Thus, the current supply is activated, by pushing the right button, and by the analogic ampermeter we set slowly the current supply at ~ 400 A. The evaporation time is 35''.

- The pressure in the chamber is balanced with the atmosphere by a lateral valve and is opened with great care. The samples are taken, the water supply is turned off and the chamber is cleaned with acetone.

Thermal annealing

Thermal treatment can be applied either to the final device (post-annealing), or the device prior to deposition of the cathode (pre-annealing). In our device fabrication we apply only post-annealing. Time and temperature are the two main factors in this process. However, the most important factor to decide these time and temperature options is the materials which were used for the device. More information on this issue will be analyzed in chapter 6.

The efficiency of the device depends largely on the manufacturing conditions, which affect the self-organization of the polymer and the related optical and electrical properties. It has been shown that the crystallinity of the P3HT may be increased by heat treatment, forming crystallites with conjugated chains parallel to the substrate. The improved crystallinity increases the absorption of light in the near infrared range, holes mobility and reduces carrier recombination due to improved refining pathways. All of the above contribute to a better cell performance. Kim et al. reported the importance of regioregularity to self-organization of P3HT, and to increment of crystallinity through thermal treatment.

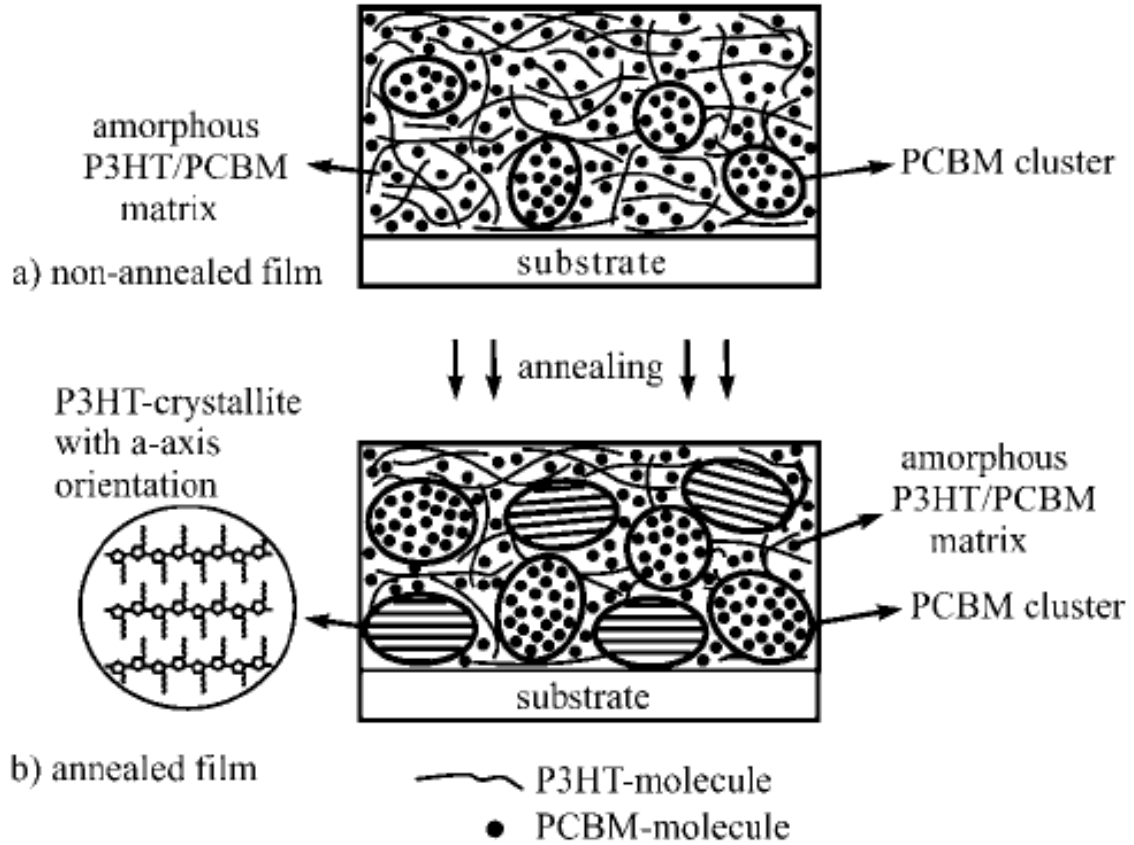


Figure 5. 9 Illustration of the microscopic reorganization during the thermal treatment of the active layer. The clusters of PCBM (after the thermal treatment) grow, thus there is more space for self-organization, crystallization of P3HT chains.

Device Characterization

The basic characterization of solar cells, includes measurements of the current of the device as a function of applied voltage under conditions of darkness and light. The voltage is applied from a voltage source and measurement of the current from a digital multimeter. These instruments are controlled by the computer B1500A (Semiconductor Device Analyzer) of Agilent Technologies. The software that is used is Easy EXPERT. The main light source is a device simulation helium emission spectrum with equal illumination AM 1.5. The device was placed on a base, where the light ends via a mirror, the ITO side facing the image of the light source.

Voltage-current

After positioning of the device, the necessary wiring follows. Initially, we bring together the two electrodes to the device. The one electrode contacts the coated with ITO surface, while the other electrode contacts to the cathode (aluminum metal). The electrodes were rimmed with rounded edges, in order not to take the risk of etching the samples.

Afterwards, the whole layout is covered with a black cloth to start the measurement process in a dark environment. We launch the Easy EXPERT, choosing solar cell mode, then we set the range and step voltage, and the time that will elapse between the measurements, finally we obtain the corresponding current-voltage curve in the dark. The algorithm of the program calculates important values for solar cells like current density (J) and short circuit current density (J_{sc}), open circuit voltage (V_{oc}), maximum efficiency (P_{max}), fill factor (FF), cell efficiency (n%).

The lamp is turned on and the power is set in order to act as sun simulator ($100\text{mW}/\text{cm}^2$). Then, a similar procedure occurs to obtain the current-voltage curve under illumination.

Finally the curves and the values which obtained by Easy Expert are processed by Origin Pro 8. Where, useful curves also are designed (logarithmic, zoomed curves from J_{sc} to V_{oc}).

Aging effect

Aging effect is called the decay of the device as a function of time. It is important, for understanding the quality of a solar cell to be examined under illumination. The measurements carried out under illumination relates to the change made by time in all major values, such as J_{sc} , V_{oc} , FF and n%.

The same wiring is kept by examining current-voltage under illumination. We launch the Easy EXPERT, pick ... mode and after setting ... we get a current-voltage curve at a time. After completion of the process, diagrams of short circuit current-time, open

circuit voltage-time, fill factor and efficiency-time are made. In these graphs can be seen the reduction of these factors in relation to the time and essentially assume the life of the solar cell.

The timing of measurements varies depending on the technology of the photoactive layer. Cells with photoactive layers without nanoparticles were measured for 45 hours, plasmons solar cells with nanoparticles of gold and silver, were measured for 65 hours.

⁸³ E. Stratakis , M. Barberoglou , C. Fotakis , G. Viau , C. Garcia , G. A. Shafeev
Opt. Express 2009 , 17 , 12650 .

⁸⁴ E. Stratakis , V. Zorba , M. Barberoglou , C. Fotakis , G. A. Shafeev ,
Nanotechnology 2009 , 20 , 105303 .

Chapter 6

Results and discussion

6.1 Overview of research in Plasmonic OPVs

Organic photovoltaic technology is one of the most up-and-coming section of solar energy conversion technologies. Since the invention of bulk-heterojunction (BHJ) theory, this branch acquired a potentiality because of the fact that you can take advantage of the high absorption coefficient of the organic materials, without having major problems to dissociate and collect carriers under the condition of using a thin film⁸⁵. However, the increase of efficiency of a BHJ device demands reduction of layer thickness in order to exploit the dissociation of carriers, but that of course would also lead to a decrease of absorption of the BHJ film⁸⁶.

Metallic NPs can vitiate this balance by interesting properties, such as LSPR, SPP and scattering of light as was referred in Chapter 4. According to this theoretical background previous research has been done in the addition of different metallic nanostructures (e.g nanowires, nanoparticles) in electrodes ,in buffer layer or active layer. Below, the milestones of plasmonic organic photovoltaic cells are represented.

Incorporation of metallic nanostructures in active layer

In 2004, Rand, Peumans and Forrest were one of the first groups that attempt to exploit and investigate the incorporation of silver (Ag) nanoclusters in organic tandem thin-film solar cells by embedding them between two active layers. They provided experimental results which indicate that the enhancement of an incident optical field persists into an organic dielectric for distances of up to 10 nm from the center of an array of approximately 5-nm-diameter nanoparticles. Furthermore, they showed that the enhancement exists far from the resonant particle surface-plasmon excitation energy. They propose a model to explain this long-range enhancement and investigate the role that cluster spacing, shape, and an embedding dielectric medium with a complex dielectric constant play in determining plasmon enhancement. This effect was shown to increase the efficiency of tandem organic solar cells, and it would trigger several extensive research for the application of plasmonics in solar cell improvement⁸⁷.

Kyungkon Kim and David L. Carroll showed in 2005 that the embedment of chemical synthesised, stable and high conductive Au and Ag NPs into the poly(3-octylthiophene)/C₆₀ active layer of a BHJ photovoltaic devices leads to an improvement to efficiency of 50-70%⁸⁸. Ag NPs exhibited the greatest increase. This enhancement was ascribed to the introduction of “dopant” levels within the HOMO-LUMO gap of the P3OT and it was suggested by the group that that a dominate mechanism for the efficiency enhancement of a doped PV device is the improved electrical conductivity, with the enhancement of active layer absorption (due to NP scattering) playing only a secondary role.

In 2009 W.J Yoon et al. demonstrated improved optical absorption and photocurrent for polythiophene–fullerene bulk heterojunction photovoltaic devices using a unique self-assembled monolayer of Ag nanoparticles formed from a colloidal solution. They could tailor the particle-to-particle spacing by suitable nanoparticle organic capping groups that inhibit its propensity to agglomerate. The induced photo-current efficiency (IPCE) measurement demonstrated that the maximum IPCE increased to 51.6% at 500nm for the experimental devices with the self-assembled layer of Ag nanoparticles, while the IPCE of the reference devices without the plasmon-active Ag nanoparticles is 45.7% at 480nm. The enhancement was attributed to photogeneration of excitons near the plasmon resonance of the Ag nanoparticles⁸⁹.

Later on this year K. Topp et al. further investigate the positive impact that was suggested that the addition of small amounts of dodecylamine-capped Au nanoparticles into the active layer of organic bulk heterojunction solar cells consisting of poly(3-octylthiophene) (P3OT) and C₆₀ had due to improvement of electron transport. Au nanoparticles were chemically prepared with either P3HT or dodecylamine as ligands for additives to P3HT:PCBM system. Additionally, efforts were undertaken to incorporate nearly ligand-free Au nanoparticles into the system. For this reason a chemical procedure was successfully developed to remove the dodecylamine ligand shell by a postpreparative ligand exchange with pyridine, a much smaller molecule that can later partly be removed from solid films by annealing. This research conclude that the performance of the P3HT/PCBM solar cells decrease with the Au particles as an additive to the active layer, meaning that adding Au nanoparticles is not a suitable strategy in the case of the P3HT/PCBM system⁹⁰.

During the next year the effect of arrays of Au nanopillars of controlled size and spacing on the spectral response of a P3HT:PCBM bulk heterojunction solar cell were reported by S.J. Tsai et al. The patterned devices do show higher external quantum efficiency and calculated absorption in the wavelength range from approximately 640 nm to 720 nm, where the active layer is not very absorbing. The peak enhancement was approximately 60% at 675 nm. Finally it was evidenced that the corresponding resonance involves both localized particle plasmon excitation and multiple reflections/diffraction within the cavity formed by the electrodes⁹¹.

In 2011 C.H. Kim et al. developed hybrid photovoltaic device using the BHJ concept. Specifically, they compared the photovoltaic performance of silver nanowires (Ag NWs) embedded in P3HT:PCBM to that of silver nanoparticles (Ag NPs). The results indicated that the optimal hybrid photovoltaic device composed of Ag NWs generated in this effort exhibits a power conversion efficiency of 3.91%, measured by using an AM 1.5G solar simulator at 100mW/cm² light illumination intensity⁹².

More recently, Heeger et al. demonstrated enhancement to power conversion efficiency in PCDTBT/PC₇₀BM and other BHJ photovoltaic devices by embedment of Ag NP clusters and Au NPs^{93,101}. The group implied that the local field enhancement from the narrow band plasmon resonances was not the dominant mechanism but also multiple scattering leads to longer optical paths within the BHJ material and is therefore responsible for the enhancement of the PCE.

Incorporation of metallic nanostructures in buffer layer

F.C Chen et al. researched the effect of Au NP -induced surface plasmons on the performance of organic photovoltaic devices during 2009. The power conversion efficiency of these OPVs was improved after blending the Au NPs into the anodic buffer layer. The addition of Au NPs increased the rate of exciton generation and the probability of exciton dissociation, thereby enhancing the short-circuit current density and the fill factor. The group attributed the improvement in device performance to the local enhancement in the electromagnetic field originating from the excitation of the localized surface plasmon resonance⁹⁴.

Later Marina Stavvytska-Barba and Anne Myers Kelley used Raman spectroscopy in order to investigate the interaction of Au and Ag NPs when they are incorporated into or on the PEDOT:PSS film. They show that Raman spectra of PEDOT:PSS films in contact

with gold or silver nanoparticles exhibit not only enhancement but also changes in frequency and relative intensity that suggest effects of the metal on PEDOT chain morphology. Furthermore, the spectra also suggest that silver nanoparticles facilitate reoxidation of chemically reduced PEDOT to its original doped form. Finally it was assumed that these morphological and/or chemical effects may contribute to the performance of organic polymer solar cells which incorporate metal nanoparticles into or in contact with PEDOT:PSS⁹⁵.

More indications about this conclusion were added by D.D.S. Fung et al. when they investigate device mechanisms in incorporation of Au NPs into the hole collection buffer layer. Specifically, they demonstrated ~13% improvement in PCE for OPVs incorporating PEG-capped Au NPs in PEDOT:PSS, with enhancements mainly originating from J_{sc} and FF. The contribution of LSPR effect to performance improvement has been investigated through rigorous modeling and experiment. Both theoretical and experimental results showed that absorption enhancement due to incorporation of Au NPs is insignificant and provides only minor contribution to PCE improvement. They found that the reason was due to the lateral distribution feature of the strong near-field of plasmonic resonance around the metallic NPs. Regarding the electrical characteristics, they show that the incorporation of an appropriate amount of Au NPs reduces the resistance of PEDOT:PSS layer⁹⁶.

Finally, in 2012 R.S. Kim et al. report the plasmon-assisted photocurrent enhancement in Ag-nanoparticles (Ag-NPs) embedded PEDOT:PSS/P3HT:PCBM organic solar cells, and systematically investigate the causes of the improved optical absorption based on a cylindrical Ag-NPs optical model which is simulated with a 3-Dimensional finite difference time domain (FDTD) method. They demonstrated an increased optical absorption of an organic BHJ solar cell that utilizes the LRPRs of Ag-NPs, and performed a device simulation to interpret the photocurrent enhancement mechanism via a 3-D cylindrical Ag-NPs FDTD model. The solar cell efficiency was increased as a function of Ag-NPs thickness, and at a thickness of 50Å, a 60% increase of the PCE was achieved with compared to a cell that does not have Ag-NPs⁹⁷.

Incorporation of metallic nanostructures in electrodes

In 2008 S.S.Kim et al. incorporated to OPVS uniform-sized metal nanoparticles of ~13 nm via pulse-current electrodeposition, a solution process that can control the density

and size of metal nanoparticles. They embed plasmonic Ag nanoparticles on surface modified transparent electrodes to see the overall power conversion efficiency was increasing from 3.05% to 3.69%, mainly resulting from the improved photocurrent density as a result of enhanced absorption of the photoactive conjugate polymer due to the high electromagnetic field strength in the vicinity of the excited surface plasmons⁹⁸.

Next year it was demonstrated that thermally-transformed gold nanodots deposited on the ITO substrate with the layer-by-layer technique enhance the far-field propagating plasmon field via surface plasmon excitation by J.H. Lee et al. The PCE was found to be increased from 3.04% to 3.65% by the incorporation of the plasmonic gold nanostructures because of the presence of the plasmon field proximate to the gold nanodots. These results suggested that the strong coupling between the organic excitons and plasmons of the gold nanostructures results in more efficient charge transfer in the bulk heterojunction blend⁹⁹.

A new thin solar cell design with plasmonic nanostructures integrated with an optical layer, through incorporating patterned Ag NPs atop of the transparent forward electrode with a conductive optical layer inserted between the active layer and the opaque back electrode was proposed by W. Ren et al. in 2011. Through their design, a striking and broadband absorption enhancement for the active layer has been achieved. Nicely large J_{sc} enhancement factors >1.5 with respect to the reference cell can be easily realized within rather a large geometric parameter range, and a maximal J_{sc} enhancement factor as large as 1.67 can be obtained. The mechanisms responsible for this large and broad enhancement have been revealed and attributed to a synergistic effect of plasmonically field enhancement and optically interference modulation¹⁰⁰.

Lately, plasmonic Ag nanograting in backcontact of the inverted P3HT:PCBM solar cell with TiO_2 as an optical spacer were proposed and design of nanograting for effective light trapping to enhance optical absorption in active layers. The modal analysis in the multilayered solar cells provided a design guide for the optimal period to boost optical absorption in the wavelengths above 600 nm. The FDTD calculations combined with the modal analysis allowed for the optimization of nanograting for maximization of optical absorption under a standard solar radiation, and the absorption enhancement of 23% in a random polarization with nanograting of a 60 nm height and a 200 nm width at the period of 380 nm was numerically demonstrated¹⁰¹.

Yet, in this work we report the incorporation of surfactant-free NPs, made by laser ablation, in different concentration into PEDOT:PSS/active layer interphase and in the photoactive layer, and a comparison of the properties that they lend to the film. This comparison can determine the critical quantity of Au NPs into BHJ matrix for the P3HT:PCBM BHJ concept and clarify the source of the problems that can arise by adding a greater amount of NPs. Moreover the role of NPs surface termination is investigated by monitoring the performance of PV devices doped with various types of coated NPs.

6.2 *Surfactant free Nanoparticles*

The absorption spectrum of the colloidal Au NPs and Ag NPs solution in ethanol is shown in Figure 6.1 with the distinct peak at ~530 nm and ~465 nm respectively, which correspond to the theoretically predicted enhanced absorption due to plasmon resonance. The respective size distribution determined from a series of TEM images (figure 6.2) indicates that the majority of Au NPs exhibit sizes ranged from 1.5 to 20 nm with an average of ~10 nm. However, a small fraction of NPs with sizes higher than 40 nm is present as well. All the colloids prepared were stable against sedimentation for at least several months with no addition of any surface-active substances. The remarkable stability of both types of NPs is further indicated by the slow evolution of the absorption spectrum upon exposure to air.

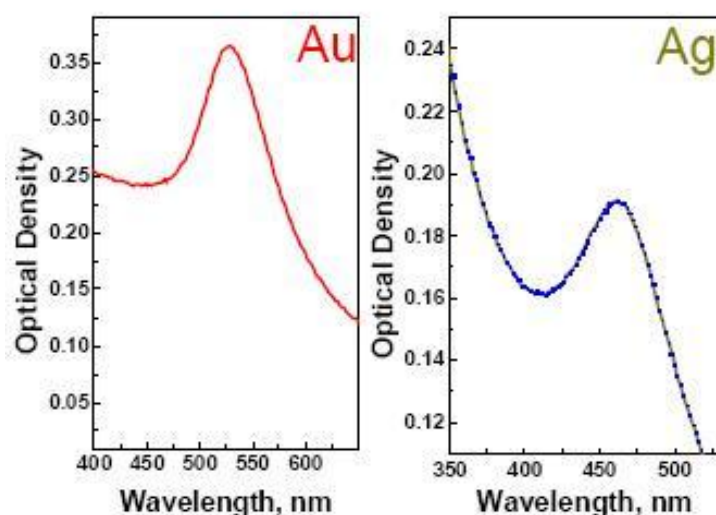


Figure 6. 1 The measured optical densities of the two types of NPs produced namely Ag and Au. Reference is absolute ethanol.

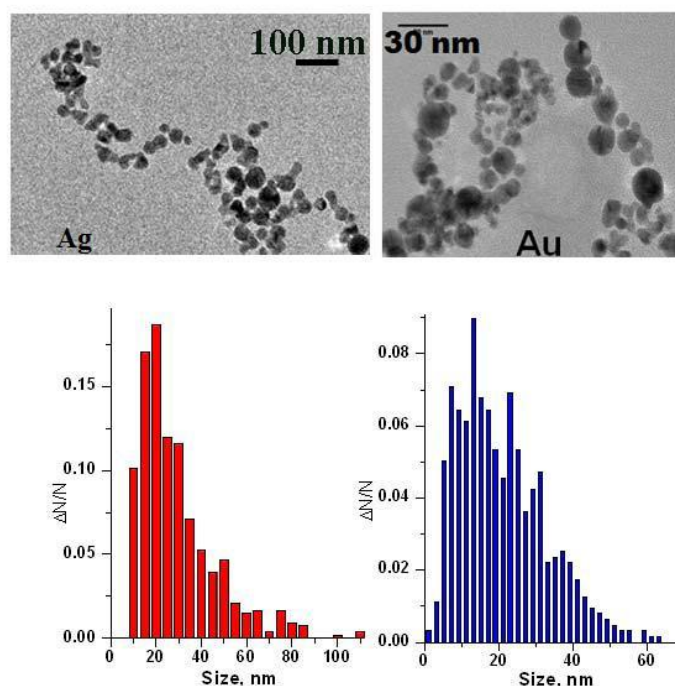


Figure 6. 2 (Top) TEM image of Ag and Au NPs generated via ablation of a bulk targets in ethanol using fs laser radiation. (Bottom) Distributions of NPs size calculated from the respective TEM images

6.3 *Incorporation of surfactant free nanoparticles in active layer/PEDOT:PSS interface*

The current density –voltage ($J - V$) characteristics are shown in Fig. 4 and the corresponding photovoltaic parameters are listed in Table 6.1 . The pristine device corresponds to that fabricated without the incorporation of the NPs layer exhibiting a PCE of 1% and a fill factor (FF) of 48%. It is important here to note that all devices were fabricated in air without the use of inert atmosphere; this is the reason for the low PCE values, which of course are expected to be improved when working at controlled atmosphere. Furthermore, several devices incorporating metallic NPs were fabricated and tested with the same PCE enhancement, indicating a fair good reproducibility. The results show that the best device attained is that included an Au NPs interfacial layer. Interestingly, the addition of NPs has greatly improved the FF and J_{sc} values, whereas the V_{oc} values were not changed much. As a result, the cell efficiency has advantageously been doubled in the case of Au NPs, while for the Ag NPs addition the PCE was increased to 1.5%.

Device	J_{sc} (mA/cm ²)	V_{oc} (V)	FF	η (%)
Pristine	3.75	0.55	0.48	1.0
Ag	4.90	0.55	0.54	1.5
Au	5.86	0.61	0.66	2.4

Table 6. 1 Photovoltaic properties of the produced devices

Figure 6.3(a) shows the optical density of P3HT:PCBM blend films with and without layer of NPs with the red shoulder (at 602 nm), indicating effective self-organization of the regioregular P3HT¹⁰². An enhanced optical absorption is observed in the spectral range of 350–650 nm where the P3HT:PCBM blend film is absorbing. Figure 6.3 (b) presents the ratios of the absorption spectra of the NPs-based devices to that of the pristine one. In the spectral range of 350–650 nm, it is observed a ~15% and ~30% increase of the total optical absorption of the Au- and Ag-based devices respectively. More importantly this absorption enhancement become maximum at the positions of the respective plasmon resonance peaks. The above results indicate that the enhanced absorption is due to the increased electric field in the active photo active layer by excited localized surface plasmons around the metallic NPs

In order to investigate the under lying mechanism responsible to the enhanced performance of the devices, we have measured the incident photon-to-electron conversion efficiency curves of the pristine and the Au NPs cell shown the best efficiency. As shown in Fig. 6 , within the wavelength range from 350 to 600 nm the photocurrent increased notably after incorporating the Au NPs. It is important that the maximum of the spectra I response enhancement coincides with the excitation peak of Au NPs indicating that the excitation of the localized surface plasmon resonance indeed improved the photocurrent. Such an improvement is probably due to the enhancement in the number or the rate of the photo generated excitons ¹⁰³. Although we have observed a greater absorption enhancement in the case of Ag compared to the Au- based devices we found an opposite behavior in the electrical characteristics. These results suggest that there might be a critical NPs concentration for optimum number and/or rate of photogenerated excitons and thus PV performance.

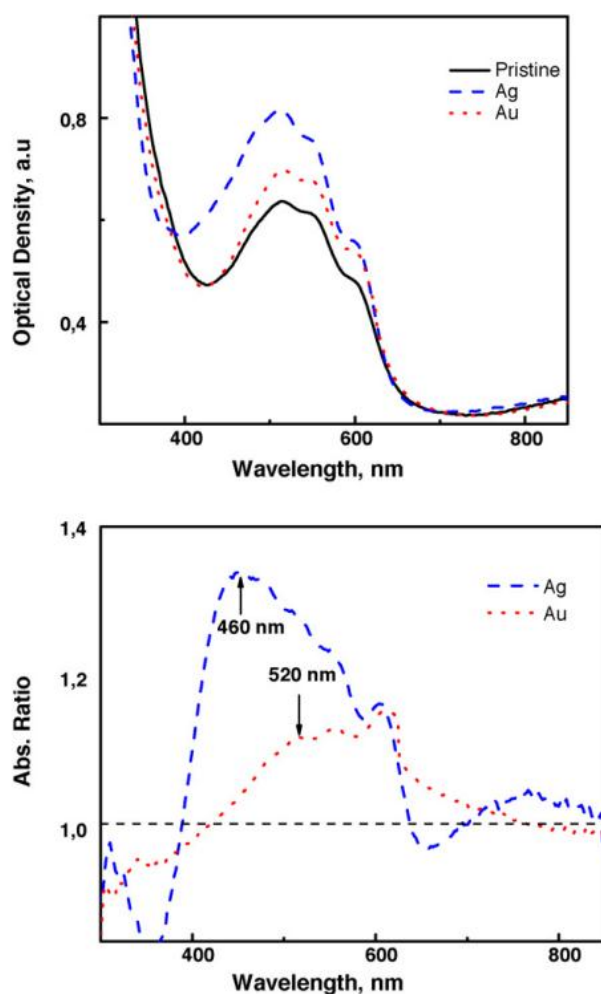


Figure 6. 3 (a) Optical absorption spectra of the P3HT:PCBM bulk heterojunction cells with and without (pristine) an intermediate layer of NPs (the absorbance is baseline corrected with the PEDOT:PSS/ ITO/glass substrate as a reference). (b) Relative ratios of the absorption spectra of NPs-based devices to that of the pristine one. The arrows indicate the positions of the plasmon resonance peaks of the respective NPs colloids

In conclusion , the efficiency of OPVs after blending metallic NPs at the interface between the active and a buffer PEDOT:PSS layer is improved. The observed improvement is attributed to the unique optical properties of the LSPR induced by the metallic NPs, which led to a noticeable enhancement of the photo current. Moreover, doping with Au NPs leads to the best efficiency improvement. The approach used in this work is quite simple and may be suitable for application to the low-temperature processes used to form OPVs on plastic substrates.

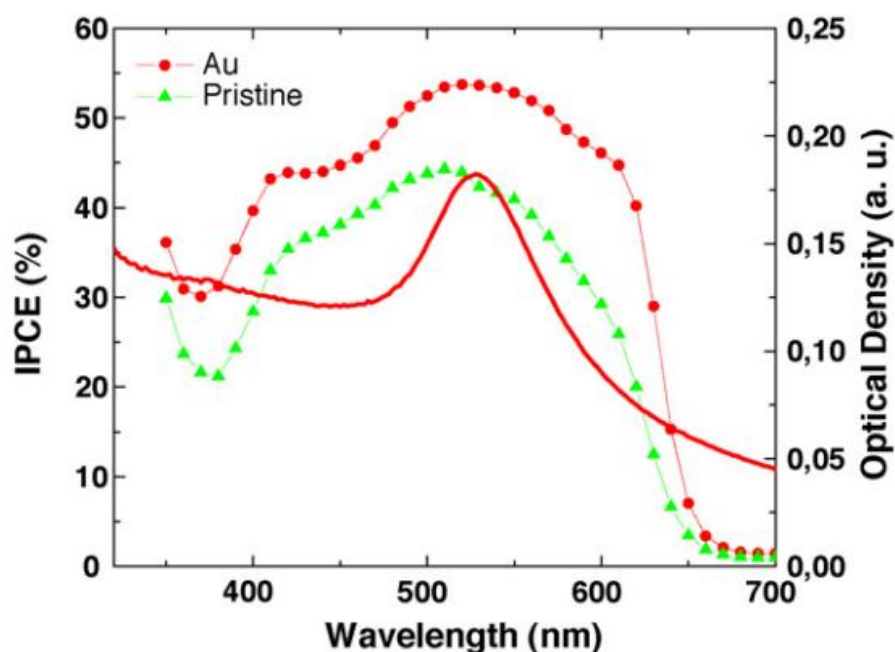


Figure 6. 4 IPCE of the investigated photovoltaic devices as a function of the wavelength of monochromatic irradiation. The absorption spec-trum of the Au NPs in ethanol (solid line) is also presented.

6.4 *Incorporation of surfactant free nanoparticles in active layer.*

In the present work , surfactant free Au NPs with various diameters are embedded in the poly(3-hexylthiophene) (P3HT):phenyl-C 61-butyric acid methyl ester—(PCBM) active layer of OPV devices for enhanced device performance. An improvement in power conversion efficiency by 40% compared to the pristine device without NPs was achieved. Notable, the spectral ranges of both the enhanced light absorption and quantum efficiency comply with the individual LSPR region of the Au NPs used. The efficiency is postulated to be enhanced by exploiting increased absorption around the small diameter NPs integrated into the active layer as well as strong light scattering from the large diameter NPs, both effects stemming from the excitation of the LSP waves at the NP/photoactive layer interface.

The technique of laser ablation generates a large variety of NPs that are free of both surface-active substances and counter- ions. More details for the experimental setup can be found elsewhere^{104,105}.The concentration of the initial colloidal solution, determined from gravimetric measurements of the target before and after the completion

of the ablation process, was equal to 0.029 g/ml. OPV devices based on the ITO/PEDOT:PSS/P3HT:PCBM/Al structure with Au NPs embedded in the active layer at different concentrations were fabricated and characterized (inset Figure 6.6(a)). The active layers were fabricated by mixing respective solutions of P3HT and PCBM at 1:1 ratio and Au NPs, in dichlorobenzene and spin-coated on PEDOT:PSS/ITO. The corresponding volume ratios of the P3HT:PCBM and the Au NPs solutions were ranged from 3%–6%. The devices were post-annealed at 160°C for 15 min in a glove box under nitrogen atmosphere. In all cases, the final active layer thickness, determined from cross-sectional SEM images (not shown), is measured to be (100 ± 5) nm.

The UV-Vis absorption spectra of the BHJ devices with Au NPs embedded in the active layer in various concentrations are shown in Figure 6.5(a). The red shoulder at 602 nm indicates the effective self-organization of the regioregular P3HT.¹⁰⁶ In the spectral region between 450 and 650 nm where the P3HT:PCBM absorbs, an increase in the percentage of absorbance is occurred proportionally to the volume ratio of Au NPs. Figure 6.5(b) presents the absorption enhancement measured on the devices (ratios of the absorption spectra of the Au NPs-based devices to that of the pristine one), together with the extinction (scattering plus absorption) spectra for Au NPs embedded in P3HT:PCBM media, as calculated using Mie theory.¹⁰⁷ For the calculation of these extinction spectra, the optical constants were changed from those of ethanol to those of P3HT:PCBM,¹⁰⁸ leading to a red-shift of the dipole resonance peak to 595 nm for Au NPs with an average diameter of 10 nm.¹⁰⁹ Notably, the absorption enhancement for 5% and 6% Au NPs concentrations exhibits maximum at 610 nm, which fairly coincides with the extinction peak of the Au NPs, indicating that an LSPR effect does indeed improve the absorption. Additionally, the observed absorption enhancement may also be partly attributed to the larger diameter Au NPs acting as efficient scatterers for solar light.¹¹⁰

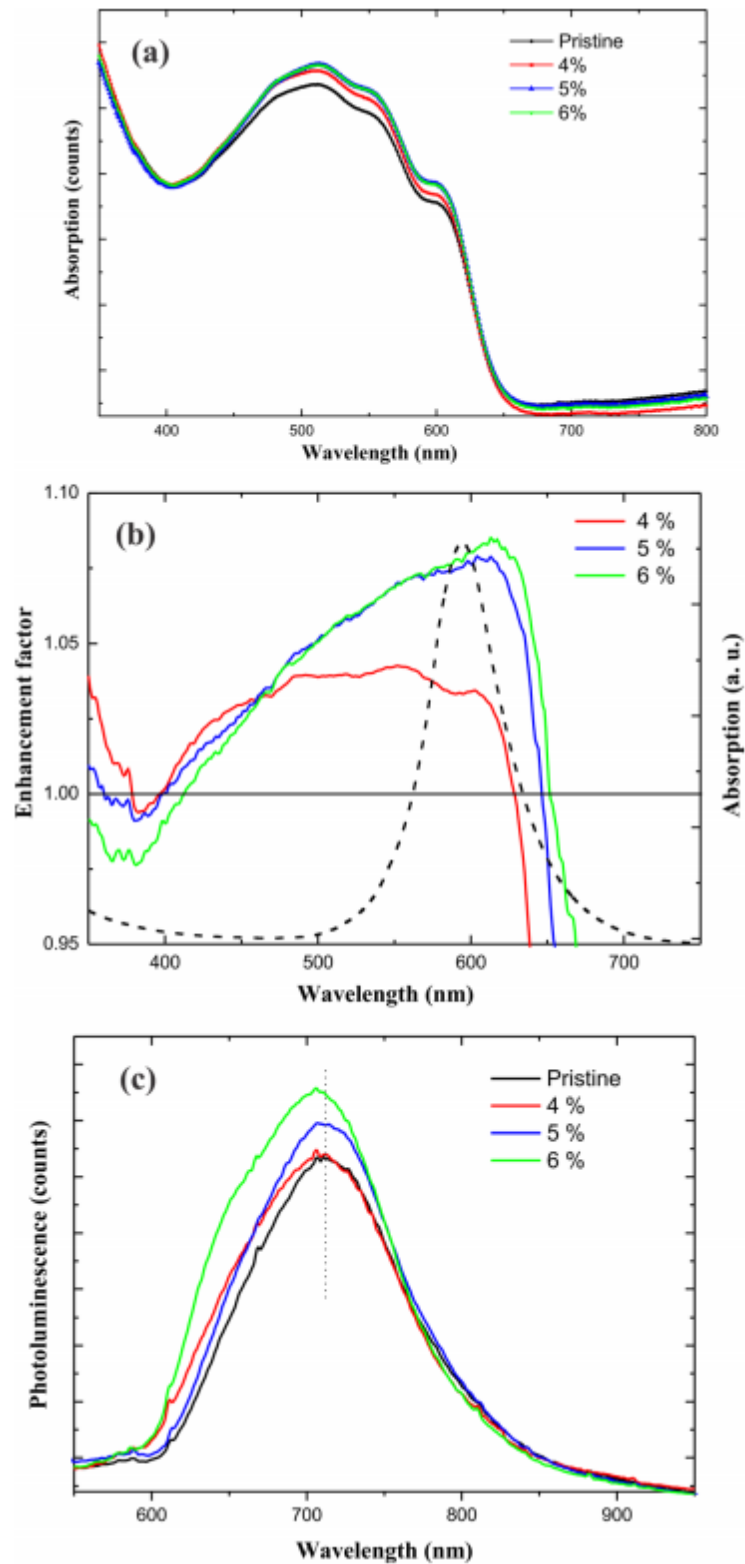


Figure 6.5 a) Absorption spectra of the BHJ devices with Au NPs embedded in the active layer in various concentrations (the absorbance is baseline corrected with the PEDOT:PSS/ITO/glass substrate as a reference). (b) Absorption enhancement factor of the devices with different concentration of Au NPs. (Relative ratios of the absorption spectra of NPs-embedded devices to that of the pristine one). The calculated extinction spectrum of the Au NPs embedded in the P3HT:PCBM medium is plotted for comparison. The dielectric constants of P3HT:PCBM were obtained from Ref.33. (c) Normalized PL spectra of P3HT:PCBM for different Au NP concentrations in P3HT:PCBM.

The photoluminescence (PL) spectra of the BHJ devices with Au NPs embedded in the active layer in various concentrations are shown in Figure 6.5 (c). The incorporation of the Au NPs, leads to broader PL spectra and an increase of the PL intensity by 20%, while its maximum at 711 nm is blue shifted to 706 nm. The broadening and enhancement of the PL intensity can be attributed to the fact that the LSPR excitation increases the degree of light collection and, thereby, enhanced the light excitation rate.¹¹¹ Moreover, the enhanced PL intensity can arise from the strong coupling between the excitonic state of P3HT and the plasmonic field of the NPs, which is due to the propagating oscillation of the surface plasmon dipole plasmonic field and excitons.¹¹² Figure 6.6 (a) displays the current voltage (J-V) characteristics of the pristine and OPV devices with different NPs fractions, under illumination with 100 mW/cm² power intensity. The respective averaged photovoltaic characteristics are summarized in Table I. It is shown that the incorporation of Au NPs in the active layer induces a significant improvement of both the device short-circuit current (J_{sc}), by 18%, and the fill factor (FF), by 19%, whereas the open-circuit voltage (V_{oc}) remains constant. As a result, a 40.5% increase in the device efficiency (η) is obtained for the device with the optimum Au NPs concentration of 5%. An increase at concentrations higher than 6% has negative effect on the device performance, probably due to the fact that the excessive content of the NPs may disturb the formation of P3HT

	J_{sc} (mA/cm ²)	V_{oc} (V)	FF (%)	η (%)
Pristine	8.27 ± 0.12	0.6	53.22 ± 0.30	2.64 ± 0.05
4% Au	8.90 ± 0.20	0.6	61.03 ± 0.40	3.26 ± 0.09
5% Au	9.77 ± 0.24	0.6	63.38 ± 0.54	3.71 ± 0.12
6% Au	9.60 ± 0.15	0.6	61.32 ± 0.48	3.53 ± 0.08

Table 6. 2 Photovoltaic characteristics of OPVs with various concentrations of Au NPs solutions into the photoactive P3HT: PCBM layer.

and PCBM domains leading to an inhomogeneous surface morphology and to lower carrier mobility. Furthermore, it can be attributed to the occurrence of local shunts due to NPs aggregates directly bridging the ITO or Al electrode. Assuming NPs of equal size of 10 nm that are homogeneously dispersed into the active layer volume (100 nm x 1cm x 1cm) and that no aggregation occurs, one can make a rough estimation of the distance

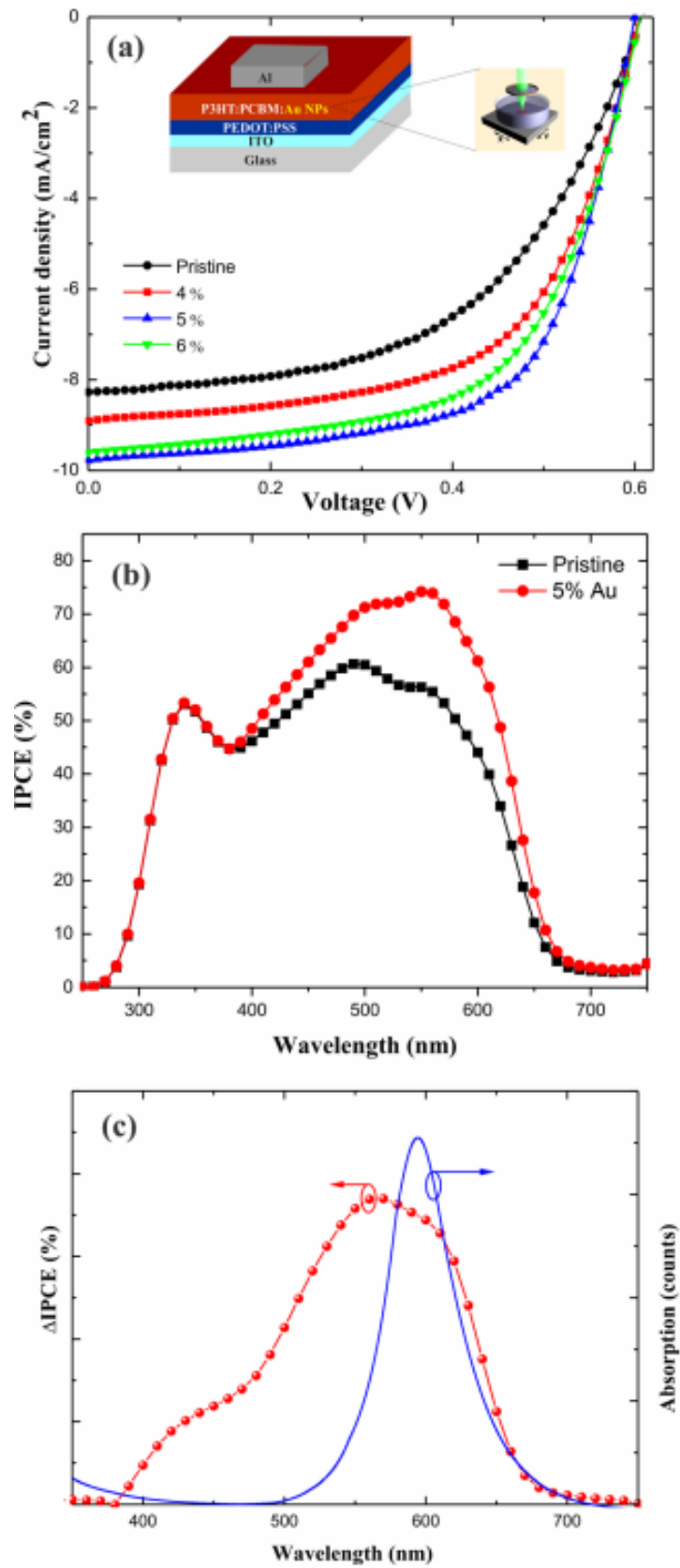


Figure 6. a) J-V characteristics of the OPV devices with Au NPs embedded in the active layer. (b) corresponding IPCE curves of these OPV devices. (c) Comparison between the curve of the increase in IPCE (Δ IPCE) after incorporating Au NPs and the calculated extinction spectrum of the Au NPs in the P3HT:PCBM medium.

among neighboring NPs inside the blend. For a volume ratio of 6% and taking into account the concentration of the initial colloidal solution, this distance is calculated to be on the order of 30 nm. This value suggests that NPs aggregation is expected to occur at higher volume ratios and thus shunting may become more important and could contribute to the observed reduction in the photovoltaic performance. On the other hand, the above estimated distance is expected to be higher considering that a fraction of NPs in the initial solution form aggregates. Local shunts within the active layer cannot be excluded for low NPs contents as well; however the J-V characteristics indicate that the optimum plasmonic device does not suffer from shunting. It can be suggested that the regions where NPs aggregates penetrate into a large extent or even through the active layer have a reduced photocurrent production.

In order to investigate the underlying mechanism responsible to the enhanced performance of the devices, the incident photon-to-electron conversion efficiency (IPCE) curve of the device exhibited the best efficiency is measured and compared with the pristine one (Figure 6.6 (b)). The corresponding increase in IPCE (DIPCE) after incorporating Au NPs is also presented together with the theoretically predicted extinction spectrum of 10 nm Au NPs embedded in the P3HT:P CBM medium (Figure 6.6 (c)). As shown in Figure 6.6 (b) , the IPCE increases remarkably upon the incorporation of Au NPs, which complies with the enhanced J_{SC} observed. In particular , compared to the pristine cell, the IPCE of the device with 5% Au NPs, becomes enhanced in a broad spectral range (400 to 700 nm), while it maximizes at 570 nm. This wavelength regime practically coincides with the spectral range in which the optical absorption of the Au-NPs embedded in P3HT:PCBM medium is enhanced due to the LSPR effect (Figure 6.5(b)).

The IPCE enhancement due to LSPR effects can be first attributed to the local enhancement of the incident electro-magnetic irradiation field in the vicinity of the small-sized NPs and second to multiple scattering by the larger diameter NPs. Moreover, it was recently demonstrated that the incorporation of NPs in the photoactive layer does not only lead to an increase in the performance, but gives rise to enhanced structural stability of the blend.¹¹³ This behavior can explain the observed disparity between the absorption and IPCE enhancement, whereas the NPs additionally enhance its structural stability, leading

to superior performance. Therefore, the performance enhancement can be also attributed to the improvement of the photoactive layer morphology due to the presence of NPs.

The use of surfactant-free NPs appears to be an efficient way to suppress exciton quenching via elimination of recombination pathways taking place on the capping layer of chemically synthesized NPs.¹¹⁴ Besides this, the laser production method employed gives rise to a rather broad NPs distribution, so that small-sized NPs will contribute to LSPR, while higher-sized ones to multiple scattering effects, respectively.

In conclusion, it was demonstrated that the incorporation of surfactant-free Au NPs in the active layer of OPV devices can significantly enhance the device performance by 40% due to LSPR and scattering effects. The spectral range of IPCE enhancement was found to comply with the theoretically predicted extinction spectra of Au NPs embedded in the active medium, indicating that LSPR effects are primarily responsible for the efficiency enhancement.

6.5 *The Effect of surfactant-free nanoparticle Incorporation on Cell Aging*

Our next goal was to address the major limitations for the poor stability of OPV devices at the typical temperatures at which they operate. The effect on NPs incorporation on the active layer stability and device aging was investigated by means of: a) in-situ time-resolved EDXR and AFM measurements complemented by EDXD, during light exposure and b) electrical stability measurements under prolonged illumination.

6.3.1 The Effect Nanoparticle Incorporation on the BHJ Morphological Properties

A comparative investigation of the structural/morphological properties of different blends, incorporating NPs and NPs-free-reference, was performed by time-resolved EDXR, applied in situ, together with AFM, during exposure to light (see the Experimental Section). The issue of the BHJ morphological stability is particularly critical and severe aging effects were observed for similar blends due to long-lasting light exposure.¹¹⁵

It is important to note that the present work takes advantage of an unconventional approach, based on the combination of X-ray and AFM measurements, allowing for

original in situ structural/morphological monitoring studies. The method requires the AFM tip to reach the active layer surface, thus imposing the exclusion of the metallic top layer. On the other hand, the reliability of the results is not compromised by the electrode absence. Indeed, we aim to detect the occurrence of possible structural rearrangements, due to thermal effects. In this case, the only relevant parameter is the sample temperature. In turn, heating of the active layer of the OPV cell is essentially due to light absorption, while the heat released when the cell is working, through the Joule effect, is negligibly low. Therefore, the picture gained will be representative of the modification of the BHJ structural properties in conditions equivalent to the real working ones.

Before discussing the results of our study, it worth remembering that, when a multilayered sample is under investigation, it is not obvious to identify the contributions of each layer to the overall EDXR signal. To overcome this problem, here, a well-established experimental protocol was adopted.¹¹⁶ First, an experimental procedure was used to maximize the signal coming from the BHJ with respect to that coming from the other layers. The sample is slightly tilted under the X-ray beam, by means of a rotating cradle. Secondly, preliminary EDXR measurements on samples representing the subsequent stages of the multilayer construction were performed: the corresponding reflection patterns are shown in Figure 6.7 .

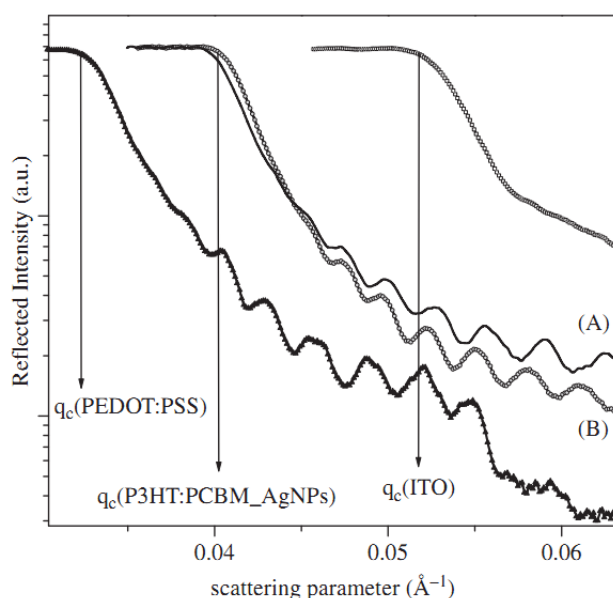


Figure 6. 7 Preliminary EDXR measurements on samples representing the subsequent stages of the multilayer construction: glass/ITO, glass/ITO/PEDOT:PSS, glass/ITO/P3HT:PCBM_AgNPs (curve (A)) and glass/glass/ITO/PEDOT:PSS/P3HT:PCBM_AgNPs (curve (B)). These measurements allowed the determination of the total reflection edge with high accuracy, providing the scattering length densities of the various layers: ITO: $\rho_e=5.8(1) E^{-5} \text{ \AA}^{-2}$, PEDOT:PSS: $\rho_e=1.9(1)E^{-5}\text{\AA}^{-2}$, P3HT:PCBM-AgNPs $\rho_e=3.3(1) E^{-5}\text{\AA}^{-2}$

These measurements allowed the determination of the total reflection edge with high accuracy and provided the scattering-length densities of the various layers. In particular, within the experimental resolution, the same scattering-length density is measured when depositing the P3HT:PCBM_AgNPs film on glass/ITO substrates (curve (A)) or on glass/ITO/PEDOT:PSS systems (curve (B)). Reversely, for the PEDOT:PSS film a lower scattering-length density is gained. These experimental evidences assign the oscillations visible at higher scattering vectors of curve (B) in Figure 6.7 to the P3HT:PCBM_AgNPs film, allowing to identify the contributions of the BHJ to the overall EDXR signal. In the following discussion of the in situ results it must be stressed that in the present case, the samples were prepared following a different procedure with respect to former studies (for example, deposition is performed in ambient conditions and a buffer layer of PEDOT:PSS between the active film and the substrate is used), as described in the Experimental Section. Therefore, an initial characterization of P3HT:PCBM reference samples (structure: glass/ITO/PEDOT:PSS/P3HT:PCBM) was performed, to provide a stringent comparison of the characteristics and of the behavior of the two systems.

The results of the in situ EDXR measurements on the reference sample are reported in Figure 6.8 , left-hand side, where the raw patterns are shown as a function of the scattering parameter, q , and of illumination time, t . Each pattern was acquired for 2 h, for an overall exposure to light of 72 hours. A shift of the oscillation towards lower q - values during light exposure is visible by the naked eye and evidenced by the arrows, suggesting that the film is getting thicker. Using an accurate data processing method (Parratt fitting procedure),¹¹⁷ the time evolution of the morphological parameters film thickness (d) and roughness (σ) were obtained, as shown in Figure 6.7 , right-hand side. The $d(t)$ and $\sigma(t)$ curves are well described by Boltzmann growth functions, and the corresponding amplitudes and time constants of the overall variations are approximately: $\Delta d = 8 \text{ \AA}$, $\tau_d = 20 \pm 2 \text{ h}$, and $\Delta \sigma = 4.5 \text{ \AA}$, $\tau_\sigma = 16 \pm 2 \text{ h}$, respectively. The overall thickness increase is about 0.6%. Such modifications in the morphological parameters evidence a bulk reorganization of blend molecules, due to heating effects consequent to illumination.¹¹⁸ The time-resolved AFM study of the reference sample, performed by periodically monitoring a fixed portion of the sample surface during exposure to light, is reported in Figure 6.9 . The sample appears to have a uniform topography, since the observed structures exhibit a height in the 4–6 nm range and a characteristic in plane size within the 100–120 nm range. This latter value, being

very close to the lateral resolution limit, represents a superior limit of the structures' in-plane dimensions. It is observed that the surface morphology does not change at all throughout the sequential collection of AFM topography images during illumination (see Figure 6.9 a) and 6.9 b) comparing the first and the last ($4 \mu\text{m} \times 4 \mu\text{m}$) images and line profiles). This steadiness of the sample topography is confirmed by the corresponding evolution of the sample surface root mean square (rms) roughness, deduced from each AFM image. Indeed, as shown in Figure 6.9 c), the rms value remains practically constant throughout the illumination time.

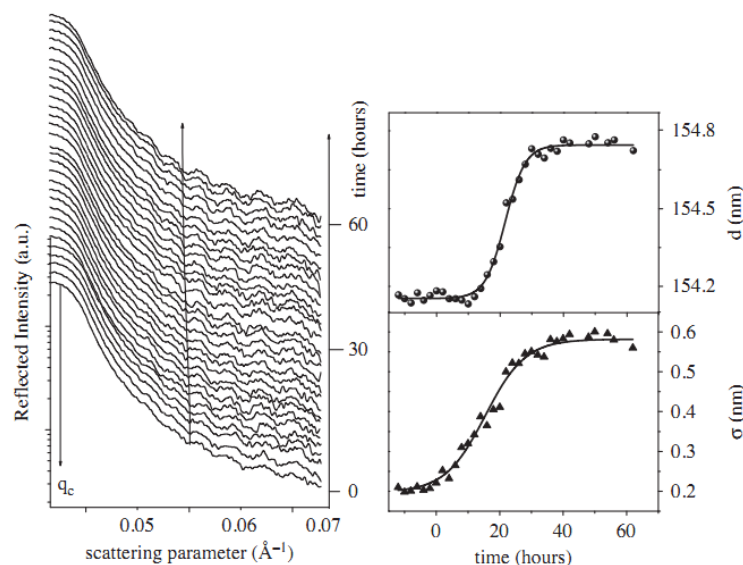


Figure 6. 8 Results of the time-resolved EDXR measurements on the reference sample. Left: the raw patterns are shown as a function of the scattering parameter, q , and the illumination time, t . Right: time evolution of the morphological parameters film thickness, d , and roughness, σ .

Since the surface roughness remains constant with illumination time, as detected by the AFM measurements, the variation of film roughness indicated by the EDXR measurements may solely be attributed to a roughening effect of the buried film interface. Therefore, the combined X-ray/AFM approach allowed the detection and evaluation of the dynamics of morphological changes occurring within the active layer during illumination and revealed two major dynamical phenomena; a bulk reorganization process indicated by the film thickness increase and a degradation effect taking place at the interface between the active and the buffer PEDOT:PSS layers. The bulk phenomenon is related to a secondary crystallization process of the blend polymeric component as observed by diffraction studies on similar blends.⁹⁸ The interface aging effect is also well consistent with the literature studies reporting swelling of the hole transport layer and subsequent etching of the transparent electrode.¹¹⁹ Alternatively, Indium diffusion from

ITO into the organic layer, observed in either OPV devices⁹⁸ or in polymer light-emitting diodes,¹²⁰ may also be at the origin of interface effects.

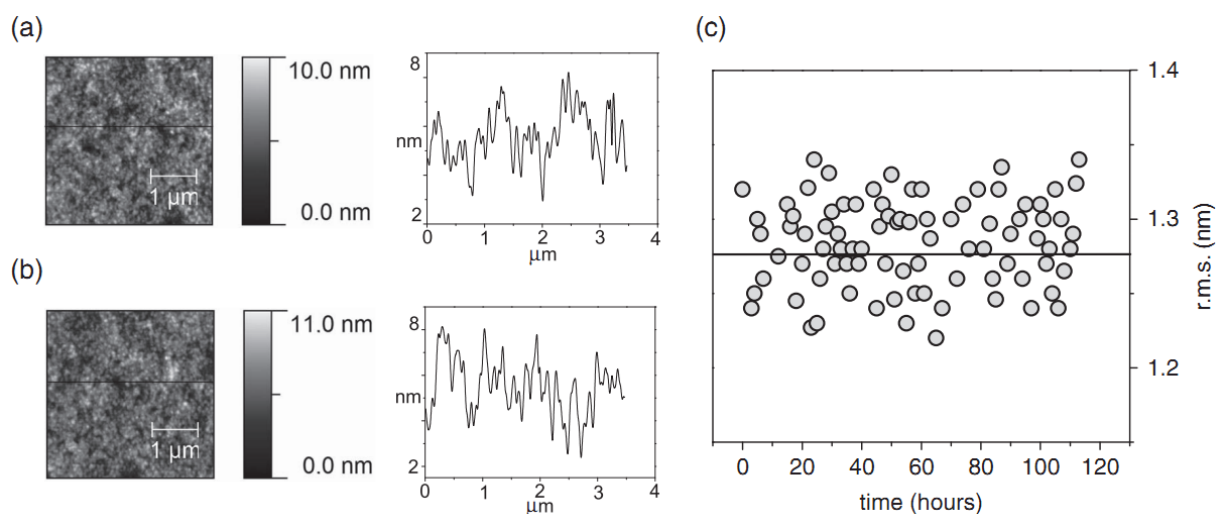


Figure 6. 9 Results of the time-resolved AFM study of the reference sample. A,B) Comparison of the first and the last images ($4\ \mu\text{m} \times 4\ \mu\text{m}$) and line profiles (extracted in correspondence of the lines in figure a and b). Figure 4c: time evolution of the sample surface roughness (rms).

The second step of this joint X-ray/AFM study is devoted to blends incorporating Ag NPs (structure: glass/ITO/PEDOT:PSS/P3HT:PCBM-NPs). Each pattern was acquired for 30 minutes, for an overall monitoring of more than 100 hours. The Parratt fitting applied to each pattern provided the time evolution of the morphological parameter with the corresponding results presented in Figure 6.10. It is observed that the overall thickness remains unchanged during light exposure; d values follow a steady distribution around their mean value. On the other hand, the EDXR roughness σ (joint interface and surface contribution) remains constant for the first 20 hours, and sub-sequently undergoes a fast rise up to an asymptotic value. The $\sigma(t)$ curve evolution can be fitted by a Boltzmann growth (red line), having a characteristic time of $\tau_{\sigma} = (18.0 \pm 0.5)$ hours. The overall roughness increase is about $2\ \text{\AA}$ ($\Delta\sigma = 2\%$). This relative change is much lower than that measured in the case of the reference BHJ blend.

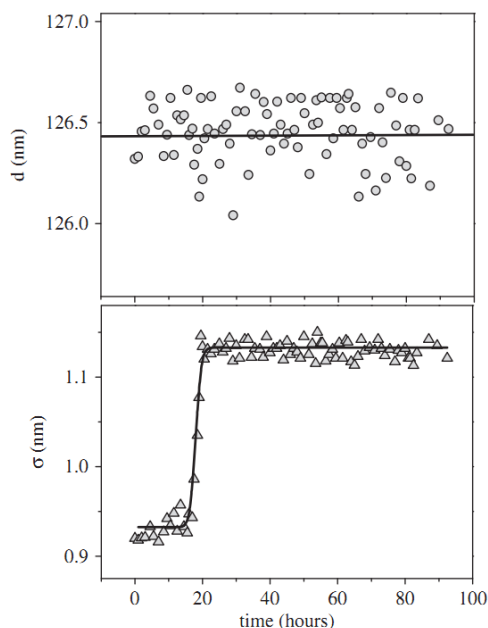


Figure 6. 10 Results of the time-resolved EDXR measurements on the P3HT:PCBM-NPs sample. Time evolution of the morphological parameters, film thickness (d) and roughness (σ).

Therefore, EDXR experiments indicate that the NPs doped film, unlike the reference one, showed a limited modification of the morphological parameters, exhibiting only a minor film roughening effect. A deeper understanding of the origin of such effect was provided by time resolved AFM studies, allowing the evolution of surface topography to be monitored as well. Figure 6.11 reports the comparison between the first (figure 6.10 A, upper part) and last (figure 6.10 B, lower part) of the AFM ($6 \mu\text{m} \times 6 \mu\text{m}$) images collected upon illumination. The corresponding line profiles presented in Figure 6.11.

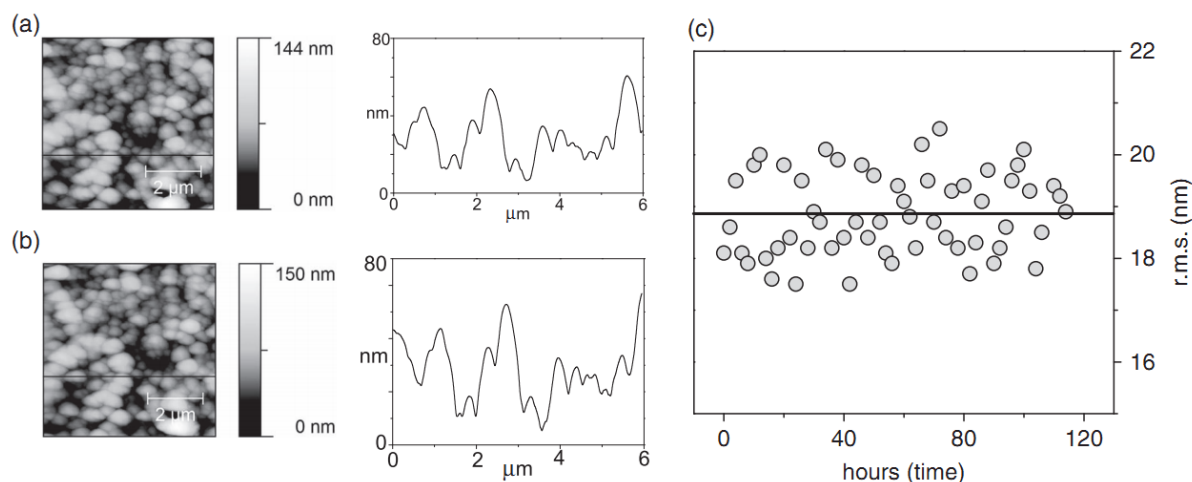


Figure 6. 11 Results of the time-resolved AFM study of P3HT:PCBM-NPs sample. Figure 6A and 5B comparison of the first and the last ($4 \mu\text{m} \times 4 \mu\text{m}$) images and line profiles (extracted in correspondence of the lines in figure A and B). Figure 6C: time evolution of the sample surface roughness (rms).

clearly evidence that the very same topographical features are present, even after 100 hours of continuous illumination. In this case, globular structures are present, the characteristic dimensions of which range from $x_{\min} = y_{\min} = 200$ nm to $x_{\max} = y_{\max} = 700$ nm (in-plane size) and from $z_{\min} = 10$ nm to $z_{\max} = 60$ nm (vertical dimension), respectively. The corresponding time evolution of the rms surface roughness deduced by the analysis of each AFM image collected during the sample illumination (2 hours acquisition time) is reported in figure 6.11 C indicating that the rms value remains constant, distributed around the mean value of ~ 19 nm.

At this point it is important to stress the elevated sensitivity of in situ time-resolved AFM measurement, which is able to detect a surface roughening of the sample in the order of 1 \AA .^{98, 121} In the present case, small changes in the top surface roughness, consistent with the 2 \AA roughness increase measured by EDXR, would be well detectable. We can, therefore, conclude that the roughening process established by EDXR involves the active-layer buried interface only.

In conclusion, combined EDXR and AFM experiments suggest that the incorporation of Ag NPs into BHJ blends essentially leads to an enhanced structural stability of the bulk of the photoactive layer, so that the only source of instability is related to a minor roughening process taking place at the blend/PEDOT:PSS interface. This is an important result, considering that the film under study was not subjected to any prior thermal treatment, usually mandatory to enhance its structural characteristics.

6.3.2 The Effect of Nanoparticle Incorporation on the Bulk Blend Structural Properties

EDXD analysis provided additional information on the interesting structural properties of the plasmonic active layer. EDXD was applied in-situ during exposure to light. The patterns in the sequence of Figure 6.12 show by both an amorphous and a crystalline contribution. On the right-hand side of Figure 6.12 a magnification of the q regions of interest, showing the P3HT (020) reflection at $q = 3.32(1) \text{ \AA}^{-1}$ and the PCBM signal at about $q = 2.11(1) \text{ \AA}^{-1}$, is shown. The data indicate that the active layer can be described as a composition of P3HT crystallites embedded in an amorphous polymer matrix. This finding is in agreement with literature data on P3HT:PCBM films,⁹⁸

demonstrating that the incorporation of NPs does not perturb the structural properties of the blend.

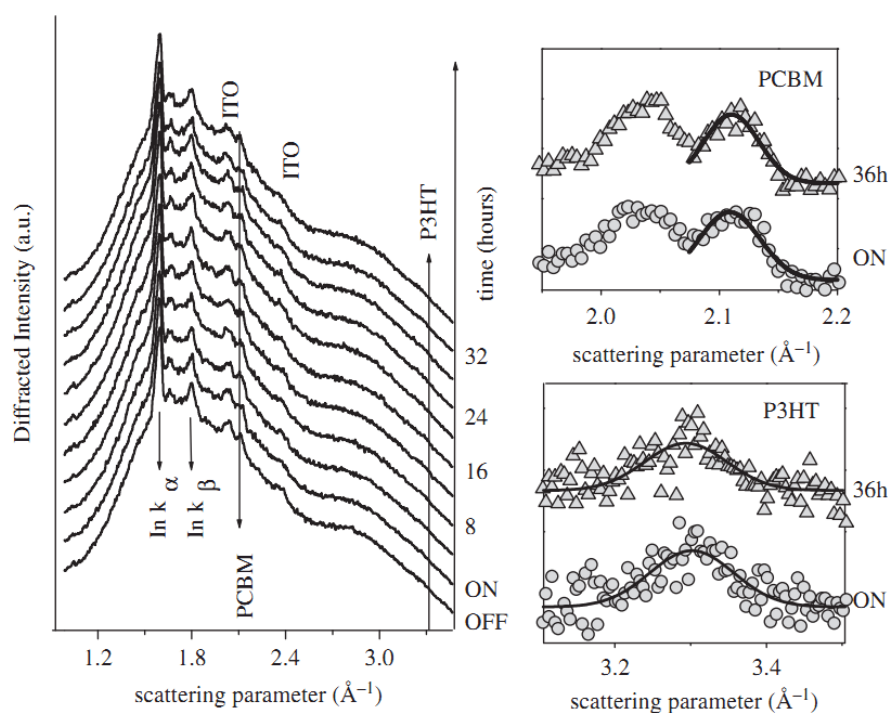


Figure 6.12 Results of the time-resolved EDXD measurements. Left: the raw patterns are shown as a function of the scattering parameter, q , and of the illumination time. Right: a magnification of the regions shows the P3HT and PCBM signals: comparison of the first (bottom) and last (top) patterns acquired during illumination.

Figure 6.13 shows the result of the analysis of the time-resolved diffraction data (in Figure 6.12). No appreciable modification of the crystalline scattering intensities is observed during illumination, indicating that the number of crystallite nanodomains for a unit volume (crystallinity) remains unchanged. The average crystal-lite size of P3HT and PCBM nanodomains was estimated from the diffraction pattern, by means of an equation based on the Laue relations (equivalent to the Scherrer formula valid for the angular dispersive X-ray diffraction mode).⁹⁸ The results in Figure 6.12 show that the average size of the crystallites of both film components remains constant during illumination.

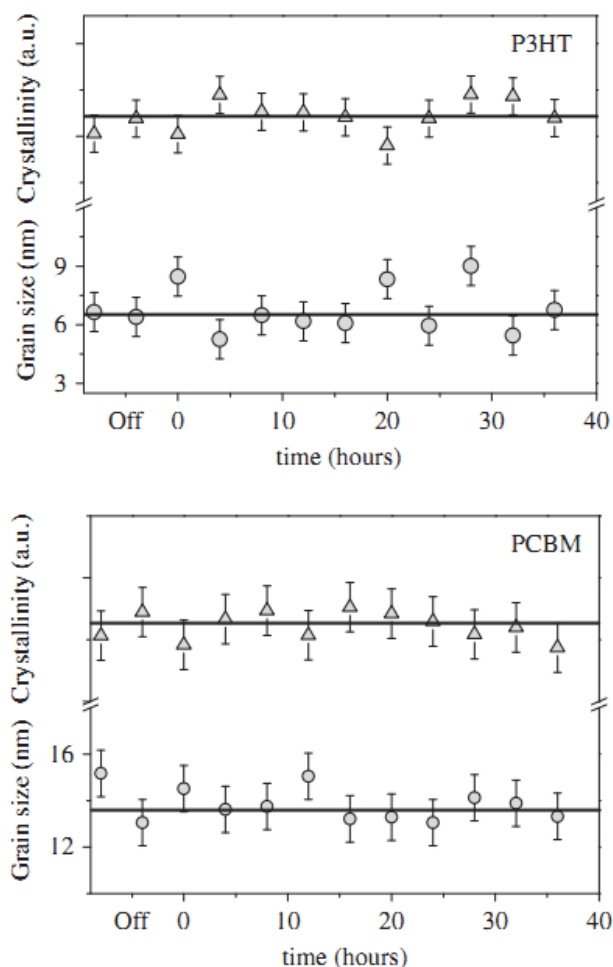


Figure 6. 13 Time dependence of the cristallinity and of the average crystal-lite size for P3HT and PCBM components, estimated from the diffraction patterns in Figure 6.12.

Therefore, time-resolved diffraction analysis demonstrates that the initial structural properties are preserved upon light exposure. This finding is an important result considering our previous observation that illumination induces relevant modification of the structural properties in NP-free blends.^{98,122} Indeed, different from what we observe here for the plasmonic blends, for undoped P3HT:PCBM films a raise in both the number of P3HT crystallite for a unit volume and in the nanodomain size was detected. This fact is an indication that, when the NPs are not included in the BHJ, a secondary crystallization process of the blend polymeric component occurred during illumination (see the Supporting Information). On the contrary, incorporation of NPs into the blend may well hinder the segmental motions of the polymer chains, leading to an effective increase in its glass-transition temperature and therefore to a mitigation of the detrimental rearrangements of the polymer structure. In conclusion, by comparing the EXDR, AFM and EDXD results it can be safely asserted that doping of the BHJ PV blends with Ag

NPs gives rise to enhanced bulk stability. Contrary to the reference undoped cells, the only aging effect detected was a minimal augmentation of the roughness upon illumination. The overall picture is completed by DSC analysis of the blends' thermal properties presented in the following.

6.3.3 The Effect of Nanoparticle Incorporation on the Bulk Blend Thermal Properties

In polymer–fullerene blends the morphological properties are strongly influenced by temperature, due to thermodynamic and kinetic effects involving reorganization, aggregation, and crystallization of each component. This property is usually exploited to control a priori the nanodomains morphology by means of thermal annealing treatments. At the same time T_g of the blend, is a critical parameter to consider when assessing the long-term durability of the morphological properties of such films, since it determines the maximum temperature at which the PV cell may operate. The bulk modifications of the P3HT:PCBM reference film morphology described above are well consistent with the consideration that, during illumination, the sample temperature may rise up to temperatures close to T_g , due to thermal heating. On the contrary, such effect is not observed when the active layer is doped with plasmonic NPs. Therefore, comparative DSC studies of the plasmonic and the reference BHJ blends have been performed to obtain a deeper understanding of such different behaviour. The DSC measurements for P3HT:PCBM and P3HT:PCBM_AgNPs are compared in Figure 6.14, where the data for the reference blend are in good agreement with the literature.¹²³ More detailed analyses of the region between $-20\text{ }^\circ\text{C}$ and $120\text{ }^\circ\text{C}$, allowed to detect the glass transition at about $50\text{ }^\circ\text{C}$. In particular, the derivative of the sigmoid fit of the DSC data (see the inset of Figure 6.14) provided an accurate estimation of T_g in both cases; T_g (P3HT:PCBM) = $41\text{ }^\circ\text{C}$ and T_g (P3HT:PCBM_AgNPs) = $53\text{ }^\circ\text{C}$. The observed increase in T_g when NPs are embedded in the blend is consistent with the above results and further support the improved structural stability of the plasmonic BHJ blends.

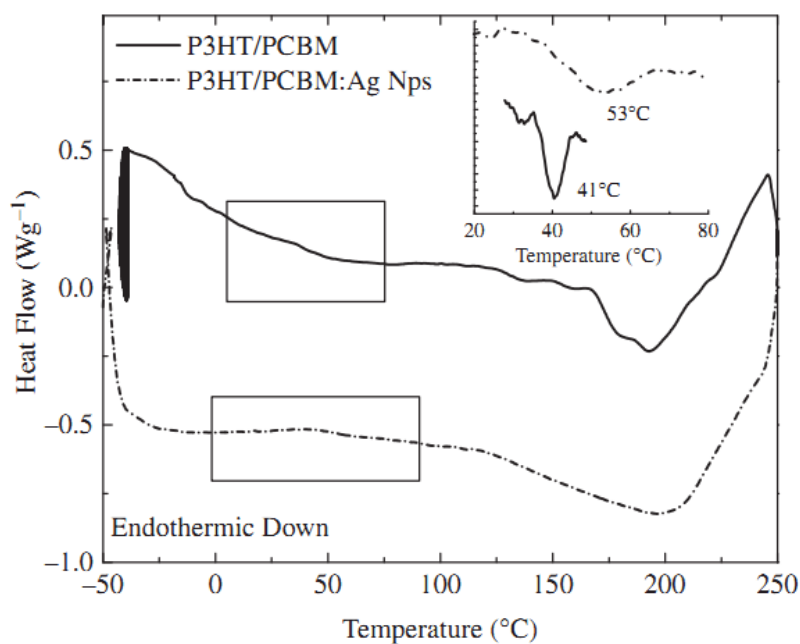


Figure 6. 14 Results of the DSC measurements for P3HT:PCBM and P3HT:PCBM_AgNPs. The derivative of the sigmoid fit of the DSC data, evidencing T_g, is shown in the inset.

6.3.4 The Effect of Nanoparticle Incorporation on the Performance Aging of Photovoltaic Cells

The superior structural/morphological characteristics of the plasmonic organic layer were correlated to the durability of the PV properties of the corresponding PV cells after continuous operation under simulated solar illumination. In order to monitor the stability in conditions similar to outdoor, the experiments were performed with the devices being unencapsulated and exposed to ambient air during operation. The PV characteristics, as a function of exposure time, normalized to their initial values (shown in Table 1) are reported in Figure 10 . In the curves the normalized J_{sc} , the FF , the open-circuit voltage (V_{oc}) and the PCE of the reference and the Ag NP-based solar cells are compared (see the Experimental Section). Current–voltage data were collected at 30 min intervals under simulated AM1.5

solar irradiation (100 mW cm^{-2}). In each point a complete I–V curve is obtained. Between successive measurements, devices were continuously irradiated in the open circuit mode. For the first 20 h, which was the time scale of the morphological aging process of the reference active layer, described in the previous section, an abrupt aging of the reference cell was detected, caused essentially by a single-step exponential decay of J_{sc} , while V_{oc} is relatively stable over this time. On the contrary, in the same time scale,

the degradation rate of the NP-based device is slower, preserving more than 30% of its initial PCE. In particular, the device decay under operational conditions exhibits three stages. In the first stage we observe a fast decay of FF to $\approx 80\%$ of the initial value and of J_{sc} and V_{oc} to $\approx 60\%$ of the initial value on the time scale of ≈ 20 h. This is followed by a second stage ($\approx 20\text{--}35$ h) where V_{oc} and J_{sc} decrease linearly, while the FF remains constant. Accordingly, the dynamics of the second stage of the aging process match well with the time scale of the interface roughening observed by the EDXR/AFM techniques (Figure 6.9). In the last stage ($\approx 35\text{--}45$ h) V_{oc} and J_{sc} degrade slowly, while the FF rapidly decays determining the life-time of the device. This type of delayed, fast degradation is also referred to as secondary failure, attributed to the degradation of the organic-electrode interfaces triggered by solar radiation, and neither by inherent instability of the materials nor by heat.¹²⁴ In conclusion, the structural and morphological modifications during illumination, described above, were likely a source of degradation of the PV characteristics of the devices. Most importantly, the comparison of time-resolved structural investigations and PV performance data show that the incorporation of NPs stabilizes the photoactive layer, allowing the preservation of the OPV cell performance, leading to an enhanced stability over time. The effects are very similar to what is observed by the incorporation of carbon nanotubes to organic light-emitting and PV devices suggesting the possible generality of the effect well beyond metallic NPs.^{125,126,127}

6.6 The role of nanoparticles surfactant

The role of the NPs surface termination is investigated by monitoring the performance of PV devices doped with various types of coated NPs. NPs with different kind of ligands were chemically synthesized.

6.5.1 Incorporation of coated with ligands-Au NPs into the active layer

In order to investigate the role of surfactant of NPs through a comparison with surfactant-free NPs, Au NPs were prepared with either P3HT or TOAB as ligands. TEM images of the two production steps and the corresponding diameter distributions of the resulting NPs, produced by chemical synthesis are shown in Figure 6.15. The most probable diameter in accordance with the size distribution histogram appears to be at 8

nm. Fig. 6.16 displays the differences in UV-vis spectra of TOAB stabilized Au NPs and P3HT stabilized Au NPs. The TOAB stabilized Au NPs solutions exhibit distinct peaks corresponding to the theoretically predicted enhanced absorption due to plasmon resonance of Au. On the other hand P3HT stabilized Au NPs solution presents a wider and less distinct peak due to optical density of P3HT.

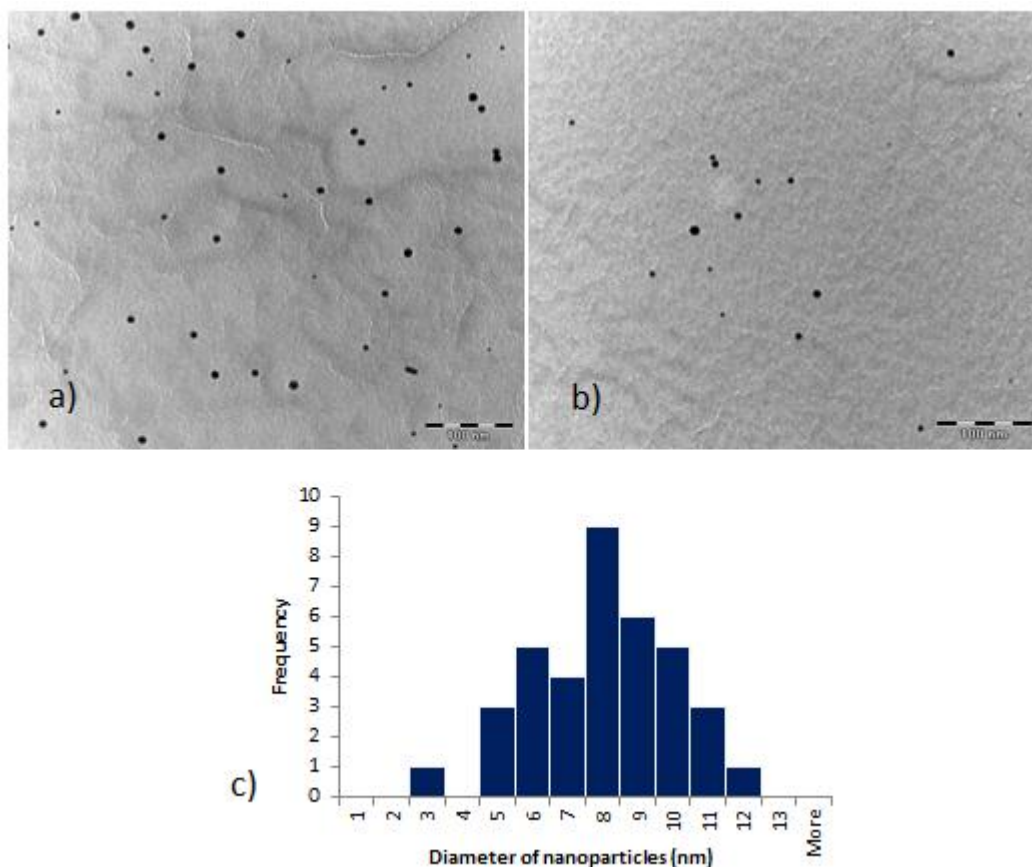


Figure 6. 15 a)TEM image of TOAB stabilized AuNPs. b) TEM image of P3HT stabilized AuNPs.c) Size distribution histogram of the P3HT stabilized AuNPs.

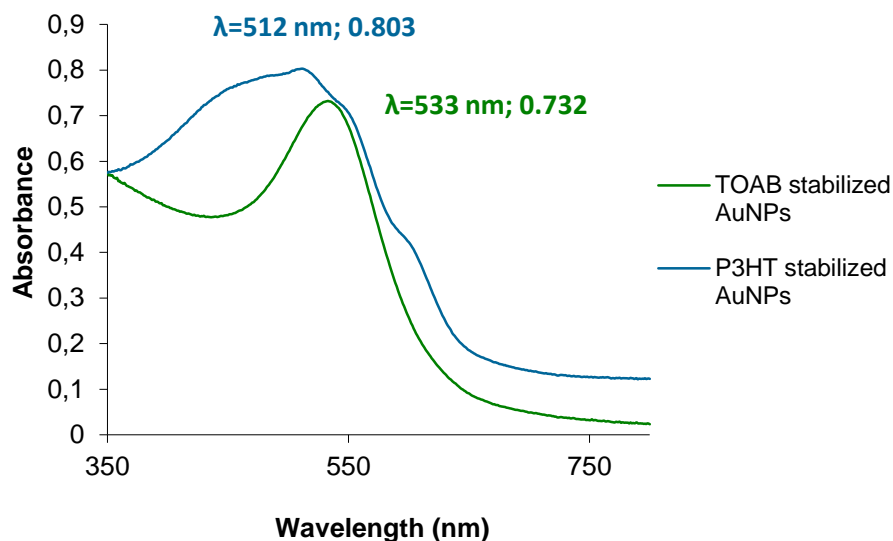


Figure 6. 16 UV-vis spectrum of the TOAB stabilized AuNPs (green line) and P3HT stabilized AuNPs (blue line).

The influence of coated-Au NPs incorporation on the performance of OPVs was studied by preparing and comparing the J-V characteristics and incident-photon conversion efficiency (IPCE). In Figure 6.17 are demonstrated the representative J-V curves and the corresponding IPCE curves and Table 6.3 summarizes characteristic values of the devices. The reference cells reached open circuit voltages (V_{OC} , voltage at zero current) of ~ 0.6 V and short circuit current densities (J_{SC} , current density at zero voltage) of ~ 8.3 mA/cm² with a fill factor ~ 0.54 and power conversion efficiency in the order of 2.65% as it was also shown in chapter 6.3. In the first approach we incorporate P3HT covered AuNPs result to devices with optimized J_{sc} in comparison with the reference. However it was V_{oc} and FF that decreased the power conversion efficiency in the case of coated Au NPs embedment. The J_{sc} improvement compared to reference can be attributed to LSPR and scattering as it was shown to bare NPs incorporation, but in comparison with surfactant-free plasmonic OPVs the J_{sc} for the critical concentration was still lower. This was ascribed to the recombination pathways that are formed by the P3HT chains to the conductive NPs and they enable efficient quenching of excited states in the polymer phase (exciton traps). Segregation of P3HT coated Au nanoparticles at the interface between the active layer and the Al contact might contribute to the decreased efficiency as well.

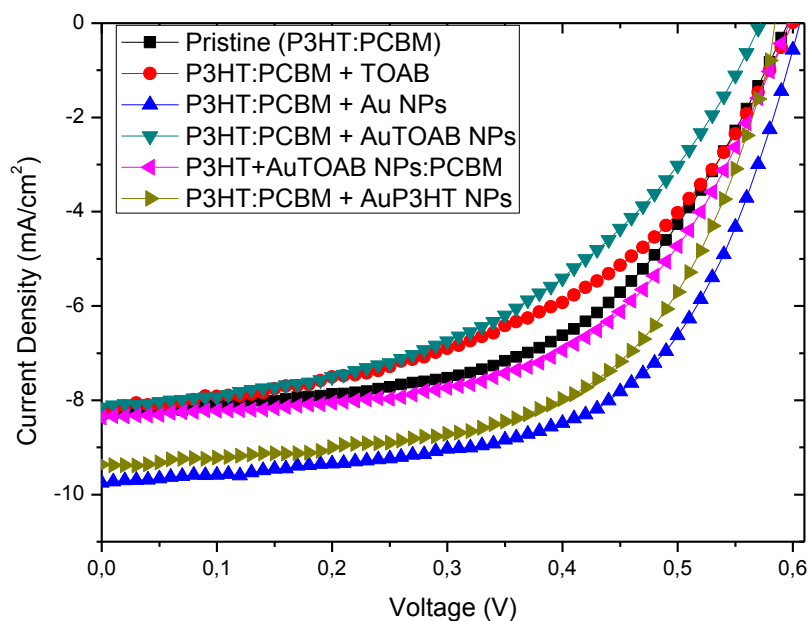


Figure 6. 17 J-V characteristics of the OPV devices with different types of Au NPs embedded in the active layer.

	J_{sc} (mA/cm ²)	V_{oc} (V)	FF (%)	η (%)
Pristine (P3HT:PCBM)	8,29	0,60	0,54	2,66
P3HT:PCBM + TOAB	8,27	0,60	0,53	2,65
P3HT:PCBM + Au NPs	9,75	0,61	0,60	3,52
P3HT:PCBM + Au TOAB NPS	8,15	0,57	0,47	2,18
P3HT+ Au TOAB NPS :PCBM	8,36	0,60	0,56	2,80
P3HT:PCBM + AuP3HT NPs	9,36	0,59	0,59	3,25

Table 6. 3 Photovoltaic characteristics of OPVs with various types of Au NPs solutions into the photoactive P3HT:PCBM layer.

In a second approach Au NPs were synthesized only with TOAB ligand as is referred above. In order to investigate the effect of TOAB addition in the NPs we developed NP-free devices with TOAB and we compared them with reference and TOAB coated Au NPs devices. The addition of critical concentration of TOAB coated Au NPs led to decreased J_{sc} ($\sim 8.15 \text{ mA/cm}^2$), V_{oc} ($\sim 0.57 \text{ V}$) and FF (0.47), thus we had an attenuation of power conversion efficiency in the order of 22%. Moreover the pre-addition of TOAB coated Au NPs result to a better device but still reduced compare with the pure plasmonic devices. In spite of the incorporation of LSPR and scattering agents into the active layer we faced a reduction on device characteristics. These results suggest that not only the morphology of the blend changed (FF and V_{oc} reduced) but also the exciton traps increased and generate a negative balance between recombination and LSPR-scattering enhancement every time that there is a polymer coater around NPs. Finally, the addition of the same quantity of TOAB in the active layer result to a device with power conversion efficiency similar to reference's.

6.7 Conclusions and Future Directions

In summary, our group made an important contribution to the understanding of the underlying operation mechanism and to optimization of plasmonic OPVs by demonstrating experimental results of incorporation of NPs into different areas of a plasmonic device and supporting them with the corresponding theory. Additionally, life time of plasmonic OPVs was investigated for the first time showing the changes in device's morphology. Finally, the role of the NPs surface termination was investigated by monitoring the performance of PV devices doped with various types of coated NPs.

Future work in order to clarify some factors and further improvement of the field must be done. Below, some proposals about the directions that should be researched are demonstrated:

- Determination of critical NPs shape and size is crucial for more controlled experiments.
- Discrimination of LSPR from scattering must be done, by incorporation of efficient, non-plasmonic scatterers, in order to unveil the exact operating mechanism.
- Completion of a modeling that describes the theoretical background behind the incorporation of NPs into the active layer matrix.
- Large scale production of plasmonic Organic Photovoltaic Cells in order to make the field applicable.

- ⁸⁵ C. J. Brabec, S. Gowrisanker, J.J.M. Halls, D. Laird, S. Jia, S.P Williams, *Adv. Mater.* **22**, 3839 (2010).
- ⁸⁶ S. H. Park, A. Roy, S. Beaupr, S. Cho, N. Coates, J. S. Moon, D. Moses, M. Leclerc, K.Lee, A. J. Heeger, *Nat. Photonics*, **3**, 297 (2009).
- ⁸⁷ B. P. Rand, P. Peumans, S. R. Forrest *J.Ap.Physicsa*, 2004, 96, 7519-7526
- ⁸⁸ K. Kim, D. L. Carroll, *Appl. Phys. Lett.* 2005, 87, 203113.
- ⁸⁹ W.J. Yoona, K.Y.Jung, J. Liu, T. Duraisamy, R. Revur, F.L. Teixeira, S. Sengupta, P. R. Berger, 2010, 94, 128-132
- ⁹⁰ K. Topp, H. Borchert, F. Johnen, A. V. Tunc, M. Knipper, E. von Hauff, J. Parisi, K. Al-Shamery, *J.Phys.Chem.A* ,2010,114,3981–3989
- ⁹¹ S.J. Tsai, M. Ballarotto, D. B. Romero, W. N. Herman, H.C. Kan, R. J. Phaneuf, *Opt. Expr.* 2010, 18
- ⁹² C.-H.Kim, S. H.Cha, S.C. Kim, M.Song, J. Lee, W.S.Shin, S.-J. Moon, J. H. Bahng, N. A. Kotov, S.-H.Jin, *ACS Nano*, 2011, 5, 3319-3325
- ⁹³ D. H. Wang, K. H. Park, J. H. Seo, J. Seiffter, J. H. Jeon, J. K. Kim, J. H. Park, O. O. Park, A. J. Heeger, *Adv. Funct. Mater* (2011)
- ⁹⁴ F.-C. Chen, J.-L. Wu, C.-L. Lee, Y. Hong, C.-H. Kuo, M. H. Huang, *Apl. Ph. Let.* 2009
- ⁹⁵ Marina Stavitska-Barba, Anne Myers Kelley, *J.Phys.Chem.* 2010, 114, 6822-6830
- ⁹⁶ Dixon D.S. Fung, Linfang Qiao, Wallace C.H. Choy, Chuandao Wang, Wei E.I. Sha, Fengxian Xie, Sailing He, *J.Mat.Chem.*, 2011,
- ⁹⁷ Richard S. Kim, Jinfeng Zhu, Jeung Hun Park, Lu Li, Zhibin Yu, Huajun Shen, Mei Xue, Kang L. Wang, Gyecheon Park, Timothy J. Anderson, Qibing Pei, *Opt.Exp.* 2012, 20, 12649
- ⁹⁸ Seok-Soon Kim, Seok-In Na, Jang Jo, Dong-Yu Kim, Yoon-Chae Nah, *Appl. Phys. Lett.* 2008, 93, 073307
- ⁹⁹ Ji Hwang Lee, Jong Hwan Park, Jong Soo Kim, Dong Yun Lee, Kilwon Cho, *Org.Electr.* 2009, 10, 416-420
- ¹⁰⁰ Wenzhen Ren, Guanghui Zhang, Yukun Wu, Huaiyi Ding, Qinghe Shen, Kun Zhang, Junwen Li, Nan Jan, Xiaoping Wang, *Opt. Exp.*, 2011, 19, 26536
- ¹⁰¹ Inho Kim, Doo Seok Jeong, Taek Seong Lee, Wook Seong Lee, Kyeong-Seok Lee, *Opt. Expr.* 2012, 20,
- ¹⁰² Y. Kim, S. Cook, S.M. Tuladhar, S.A. Choulis, J. Nelson, J.R. Durrant, D.D.C. Bradley, M. Giles, I.McCulloch, C.-S. Ha, M.Ree, *Nat. Mater.* 5 (2006) 197–203..
- ¹⁰³ C. Hagglund, B. Kasemo, *Opt. Express* 17 (2009) 11944–11957.
- ¹⁰⁴ E. Stratakis, M. Barberoglou, C. Fotakis, G. Viau, C. Garcia, and G. A. Shafeev, *Opt. Express* 17, 12650 (2009).
- ¹⁰⁵ E. Stratakis, V. Zorba, M. Barberoglou, C. Fotakis, and G. A. Shafeev, *Nanotechnology* 20, 105303 (2009).
- ¹⁰⁶ E. Kymakis, E. Stratakis, E. Koudoumas, and C. Fotakis, *IEEE Trans. Electron Devices* 58, 860 (2011).
- ¹⁰⁷ R. Catchpole and A. Polman, *Opt. Express* 16, 21793 (2008).
- ¹⁰⁸ W. H. Lee, S. Y. Chuang, H. L. Chena, W. F. Su, and C. H. Lin, *Thin Solid Films* 518, 7450 (2010).
- ¹⁰⁹ G. D. Spyropoulos, M. Stylianakis, E. Stratakis, and E. Kymakis, *Photon. Nanostruct. Fundam. Appl.* 9, 184 (2011).
- ¹¹⁰ H. Wang, D. Y. Kim, K. W. Choi, J. H. Seo, S. H. Im, J. H. Park, O. O.Park, and A. J. Heeger, *Angew. Chem., Int. Ed.* 50, 5519 (2011)
- ¹¹¹ A. Atwater and A. Polman, *Nature Mater.* 9, 205 (2010).
- ¹¹² J. H. Lee, J. H. Park, J. S. Kim, D. Y. Lee, and K. Cho, *Org. Electron.* 10, 416 (2009)
- ¹¹³ B. Paci, G. D. Spyropoulos, A. Generosi, D. Bailo, V. R. Albertini, E. Stratakis, and E. Kymakis, *Adv. Funct. Mater.* 21, 3573 (2011).
- ¹¹⁴ K. Topp, H. Borchert, F. Johnen, A. V. Tunc, M. Knipper, E. von Hauff, J. Parisi, and K. J. Al-Shamery, *J. Phys. Chem. A* 114, 3981 (2010).
- ¹¹⁵ B. Paci, A. Generosi, D. Bailo, V. Rossi Albertini, R. de Bettignes, *Chem. Phys. Lett.* 2010, 494, 69.
- ¹¹⁶ B. Paci, A. Generosi, V. Rossi Albertini, P. Perfetti, R. de Bettignes, C. Sentein *Sol. Energy Mater. Sol. Cells* 2008, 92, 799.
- ¹¹⁷ L. G. Parratt, *Phys. Rev.* 1954, 95, 359.
- ¹¹⁸ B. Paci, A. Generosi, V. R. Albertini, R. Generosi, P. Perfetti, R. De Bettignes, C. Sentein, *J. Phys. Chem. C* 2008, 112, 9931. 15
- ¹¹⁹ K. Kawano, R. Pacios, D. Poplavsky, J. Nelson, D. D. C. Bradley, J. R. Durrant, *Sol. Energy Mater. Sol. Cells* 2006, 90, 3520.
- ¹²⁰ M. P. de Jong, D. P. L. Simons, M. A. Reijme, L. J van IJendoorn, A. W. Denier van derGon, M. J. A. de Voigt, H. H. Brongersma, R. W. Gymer, *Synth. Met.* 2000, 110, 1.
- ¹²¹ A. Generosi, B. Paci, V. Rossi Albertini, R. Generosi, A. M. Paoletti, G. Pennesi, G. Rossi, M. Fosca, R. Caminiti, *Sens. Actuators B* 2008, 134, 396.
- ¹²² B. Paci, A. Generosi, D. Bailo, R. Caminiti, R. de Bettignes, V. Rossi Albertini, *Chem. Phys. Lett.* 2011, 504, 216.

-
- ¹²³ J. Zhao , A. Swinnen , G. Van Assche , J. Manca , D. Vanderzande , B. Van Mele , J. Phys. Chem. 2009 , 113 , 1587 .
- ¹²⁴ E. Voroshazi , B. Verreet , T. Aernouts , P. Heremans , Sol. Energy Mater. Sol. Cells 2011 , 95 , 1303
- ¹²⁵ P. C. P. Watts , P. K. Fearon , W. K. Hsu , N. C. Billingham , H. W. Kroto , D. R. M. Walton , J. Mater. Chem. 2003 , 13 , 491 .
- ¹²⁶ X.-L. Xie , Y.-W. Ma , X.-P. Zhou , Mater. Sci. Eng. 2005 , R 49 , 89 .
- ¹²⁷ G. Griffini , S. Turri , M. Levi , Polym. Bull. 2011 , 66 , 211 .